

WL-TR-95-3043

OPTICALLY SMART SURFACES FOR  
AERODYNAMIC MEASUREMENTS

JAMES E. MILLERD, PH.D.  
JAMES D. TROLINGER, PH.D.



METROLASER  
18006 SKYPARK CIRCLE #108  
IRVINE, CA 92714-6428

January 1995

FINAL REPORT FOR PERIOD 07/27/92 TO 04/28/95

January 30, 1995

APPROVED FOR PUBLIC RELEASE; DISTRIBUTION IS UNLIMITED.

FLIGHT DYNAMICS DIRECTORATE  
WRIGHT LABORATORY  
AIR FORCE MATERIEL COMMAND  
WRIGHT PATTERSON AFB, OH 45433-7562

19960305 093

DTIC QUALITY INSPECTED 1

## NOTICE

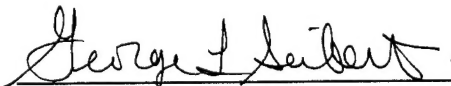
When Government drawings, specifications, or other data are used for any purpose other than in connection with a definitely Government-related procurement, the United States Government incurs no responsibility or any obligation whatsoever. The fact that the government may have formulated or in any way supplied the said drawings, specifications, or other data, is not to be regarded by implication, or otherwise in any manner construed, as licensing the holder, or any other person or corporation; or as conveying any rights or permission to manufacture, use, or sell any patented invention they may in any way be related thereto.

This report is releasable to the National Technical Information Service (NTIS). At NTIS, it will be available to the general public, including foreign nationals.

This technical report has been reviewed and is approved for publication.



LINDA G. SMITH  
Aerospace Engineer  
Experimental Facilities Research Branch



GEORGE L. SEIBERT, Chief  
Experimental Facilities Research Branch  
Aeromechanics Division

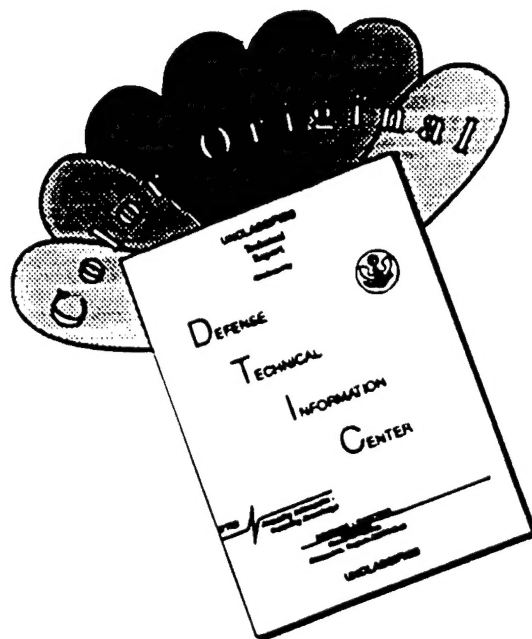


DENNIS SEDLOCK, Chief  
Aeromechanics Division  
Flight Dynamics Directorate

If your address has changed, if you wish to be removed from our mailing, list, or if the addressee is no longer employed by your organization please notify WL/FIMD, WPAFB, OH 45433-7562 to help us maintain a current mailing list.

Copies of this report should not be returned unless return is required by security considerations, contractual obligations, or notice on a specific document.

# DISCLAIMER NOTICE



THIS DOCUMENT IS BEST QUALITY AVAILABLE. THE COPY FURNISHED TO DTIC CONTAINED A SIGNIFICANT NUMBER OF COLOR PAGES WHICH DO NOT REPRODUCE LEGIBLY ON BLACK AND WHITE MICROFICHE.

REPORT DOCUMENTATION PAGE			Form Approved OMB No. 0704-0188	
Public reporting burden for this collection of information is estimated to average 1 hour per response, including the time for reviewing instructions, searching existing data sources, gathering and maintaining the data needed, and completing and reviewing the collection of information. Send comments regarding this burden estimate or any other aspect of this collection of information, including suggestions for reducing this burden, to Washington Headquarters Services, Directorate for Information Operations and Reports, 1215 Jefferson Davis Highway, Suite 1204, Arlington, VA 22202-4302, and to the Office of Management and Budget, Paperwork Reduction Project (0704-0188), Washington, DC 20503.				
1. AGENCY USE ONLY (Leave blank)		2. REPORT DATE JAN 1995		3. REPORT TYPE AND DATES COVERED FINAL 07/27/92 -- 04/28/95
4. TITLE AND SUBTITLE OPTICALLY SMART SURFACES FOR AERODYNAMIC MEASUREMENTS			5. FUNDING NUMBERS C F33615-92-C-3007 PE 65501 PR 3005 TA 41 WU 18	
6. AUTHOR(S) JAMES E. MILLERD, PH.D. JAMES D. TROLINGER, PH.D.				
7. PERFORMING ORGANIZATION NAME(S) AND ADDRESS(ES) METROLASER 18006 SKYPARK CIRCLE #108 IRVINE CA 92714-6428			8. PERFORMING ORGANIZATION REPORT NUMBER TWP04JMF.DOC	
9. SPONSORING/MONITORING AGENCY NAME(S) AND ADDRESS(ES) FLIGHT DYNAMICS DIRECTORATE WRIGHT LABORATORY AIR FORCE MATERIEL COMMAND WRIGHT PATTERSON AFB OH 45433-7562			10. SPONSORING/MONITORING AGENCY REPORT NUMBER WL-TR-95-3043	
11. SUPPLEMENTARY NOTES				
12a. DISTRIBUTION/AVAILABILITY STATEMENT APPROVED FOR PUBLIC RELEASE; DISTRIBUTION IS UNLIMITED.			12b. DISTRIBUTION CODE	
13. ABSTRACT (Maximum 200 words) This effort was to develop optically smart surfaces for aerodynamic measurement applications. Phase I established the feasibility of incorporating an optical sensor in a thin holographic coating placed on an arbitrary metallic surface. These holograms store a complex optical instrument which is actuated by impinging an "address" beam. Information is impressed by the sensor upon the address beam before it is returned to a receiver. Phase II moved these sensors from the basic research laboratory to a wind tunnel environment. Holographic sensors to measure velocity and skin friction were designed, constructed and tested in a calibration channel located at the University of California Irvine and a transonic wind tunnel located at Wright Laboratory. Efforts were made to improve sensor ruggedness and reproducibility by development techniques to produce nickel shims and mylar peel-and-stick sensors.				
14. SUBJECT TERMS Smart materials, holographic optical elements, holographic sensors laser velocimetry, and skin friction			15. NUMBER OF PAGES 92	
			16. PRICE CODE	
17. SECURITY CLASSIFICATION OF REPORT UNCLASSIFIED		18. SECURITY CLASSIFICATION OF THIS PAGE UNCLASSIFIED		19. SECURITY CLASSIFICATION OF ABSTRACT UNCLASSIFIED
				20. LIMITATION OF ABSTRACT SAR



**Blank Pages**

## TABLE OF CONTENTS

LIST OF FIGURES .....	v
LIST OF TABLES.....	viii
ACKNOWLEDGEMENTS.....	x
1.0 PROJECT SUMMARY.....	1
1.1 Analytical Proof-of-Concept.....	3
2.0 SMART SURFACES DESIGN.....	11
2.1 PM5 LV SENSOR.....	11
2.2 SURFACE RR50 LV SENSOR.....	12
2.3 MID-RANGE RR50 LV SENSOR .....	12
2.4 FAN SENSOR.....	13
2.5 TRANSMITTER DESIGN .....	16
2.5.1 OPTICAL DESIGN .....	16
2.5.2 TRANSMITTER ALIGNMENT.....	17
2.6 RECEIVER DESIGN .....	20
2.6.1 OPTICAL DESIGN .....	20
2.6.2 FAN FRINGE RECEIVER AND TRANSMITTER.....	21
2.6.3 ELECTRONICS.....	22
2.6.4 RECEIVER ALIGNMENT .....	23
2.7 SOFTWARE DESIGN .....	26
2.7.1 <i>Dburst.exe</i> .....	26
2.7.2 <i>FanBurst.exe</i> .....	28
2.7.3 <i>Control.exe</i> .....	30
3.0 SMART SURFACE FABRICATION.....	31
3.1 HOLOGRAPHIC RECORDINGS .....	31
3.1.1 SUBSTRATES AND PHOTORESIST COATING .....	31
3.1.2 RECORDING PROCEDURES .....	33
3.1.3 PM5 LAYOUT .....	34
3.1.4 RR50 LAYOUT.....	37
3.1.5 FAN FRINGE LAYOUT.....	38
3.2 SMART SURFACE INSTALLATION.....	45
3.2.1 EMBOSSED HOLOGRAMS .....	45

3.2.2	NICKEL SHIMS.....	47
3.2.3	PHOTORESIST ON GLASS .....	49
3.3	CURVED SURFACE DEVELOPMENT AND ETCHING.....	49
4.0	SMART SURFACE TESTING .....	56
4.1	METROLASER LABORATORY TESTING .....	56
4.2	UCI CALIBRATION CHANNEL TESTING .....	58
4.2.1	CONFIGURATION AND SEEDING .....	58
4.2.2	PM5 .....	59
4.2.3	RR50.....	62
4.2.4	FAN FRINGE .....	66
4.3	MEASUREMENT UNCERTAINTY.....	70
4.4	WL SURVIVABILITY TESTING.....	71
4.5	WL TGF TESTING.....	72
4.5.1	TEST DESCRIPTION .....	72
4.5.2	TGF FACILITY DESCRIPTION.....	75
4.5.3	TEST PERIOD .....	81
4.5.4	SPECIAL TEST PROCEDURES.....	81
4.5.5	TEST NOTES.....	81
4.5.6	TEST SUMMARY.....	82
5.0	RECOMMENDATIONS FOR FUTURE DEVELOPMENT .....	88
5.1	MULTIPLEXED VOLUME RECORDINGS .....	88
5.2	FAN FRINGE VOLUME RECORDINGS.....	89
5.3	CURVED SURFACE VOLUME RECORDINGS .....	89
6.0	CONCLUSIONS.....	91
7.0	REFERENCES.....	92

## LIST OF FIGURES

Fig. 1.	Conceptual layout and replay of Optically Smart Surface Laser Velocimeter Sensor .....	1
Fig. 2.	Geometry of Holographic Sensor Equations .....	3
Fig. 3.	Error in an LDV Sample Volume by Misalignment .....	8
Fig. 4.	PM5 sensor Playback arrangement. Nominally, $\theta = 50^\circ$ , $\alpha = 10^\circ$ , $\gamma = 0$ .....	11
Fig. 5.	RR50 sensor shown in the single beam, surface measurement configuration .....	12
Fig. 6.	RR50 sensor shown in the "off-surface" configuration. The probe volume and the address beams can be contained in a single plane or can be out of plane as shown in the 3-D representation .....	13
Fig. 7.	Doppler bursts near the surface for a) conventional linear fringe probe volume and b) fan fringes of velocity gradient sensor .....	14
Fig. 8.	Reconstruction of FAN sensor. Diffraction of incident light off silvered back surface produces real image of two slits on front glass surface. Reference beam is incident in horizontal plane and fan fringes are reconstructed in the vertical plane .....	15
Fig. 9.	Design of OSS transmitter. M - mirror, R - rotation stage, BS - beam splitter, L - cylindrical lens, AOM - acousto-optic modulator .....	16
Fig. 10.	Relationship between sign of frequency shift and direction of diffracted order .....	19
Fig. 11.	Relationship of direction of fringe motion with frequency shift. Case a) positive frequency shift on upstream address beam results in fringe motion in same direction as flow. Case b) positive frequency shift in down stream address beam results in fringe motion opposing flow direction .....	19
Fig. 12.	Receiver design. For situations where adequate space is available the turning mirror may not be necessary and all optics can be mounted along a linear rail .....	21
Fig. 13.	Reconstruction beam addressing fan fringe hologram from $35^\circ$ below normal (side view) .....	21
Fig. 14.	Setup for the Fan Fringe Sensor with transmitter and receiver .....	22
Fig. 15.	Parameters that may be specified using <i>Dburst</i> software .....	27
Fig. 16.	<i>Dburst</i> data acquisition screen. Top window is time scale, horizontal line indicates trigger level. Lower left window is FFT spectrum, vertical lines indicate bandpass filter cut off points. Lower right window is histogram of valid counts. Frequency and SNR represent peak frequency and signal-to-noise ratio of last valid burst .....	27
Fig. 17.	Histogram and statistics displayed at end of acquisition .....	28
Fig. 18.	Time domain burst measurements .....	28
Fig. 19.	Computer algorithm used to determine if Doppler burst is valid .....	29

Fig. 20.	Playback wavelength compensation for PM5 .....	35
Fig. 21.	Recording layout for PM5 sensor .....	36
Fig. 22.	Optical layout for recording RR series holograms and angular corrections for wavelength changes between recording and playback .....	37
Fig. 23.	Percent in Doppler frequency (from constant value) as a function of position above surface for increasing misalignment of slit focal points .....	39
Fig. 24.	Recording of the velocity gradient sensor. Reference beam is incident from behind the plate and forms a 30 degree angle with the nonfocusing axis of the object beam .....	40
Fig. 25.	Mathcad program to calculate correction distance needed during recording of the FAN fringe hologram to compensate for a different playback wavelength .....	41
Fig. 26.	Photograph of fan-fringe sensor played back with 442 nm light. Beams were visualized by sweeping a phosphorescent card (which makes the beams appear green) through the beam path while camera shutter was open .....	43
Fig. 27.	Recording geometry and mask design for self-aligning FAN sensor .....	45
Fig. 28.	Orientation for playback of embossed holograms. RR series holograms can be played in reverse but diffraction efficiency is substantially less. Diffraction efficiencies for each hologram are shown in Table 3 for the PM5 and Table 4 for the RR series .....	46
Fig. 29.	Process for recording a corrected hologram on a curved surface. Step 1 - record hologram H1 of reflected plane wave. Step 2 - Replay H1 in a phase conjugate geometry and combine with object wave at surface to record H2. Replay of surface hologram using original plane wave to reconstruct unaberrated image of object .....	50
Fig. 30.	Single step process for recording corrected hologram on a curved surface .....	51
Fig. 31.	Reconstruction of holograms recorded on stainless steel cylinders. Far field patterns of diffracted and reflected beams are visualized with a card. Beam paths are drawn in to clarify geometry. The three different holograms are: a) recorded with phase conjugate compensation, reference beam contained in sagittal plane, b) recorded with phase conjugate compensation, reference beam contained in radial plane and c) recorded <i>without</i> phase conjugate compensation, reference beam contained in radial plane .....	53
Fig. 32.	Two types of etching styles exhibited; a) no etching due to noncontact and b) contact during developing but heavy lateral diffusion and undermining .....	54
Fig. 33.	Reconstruction of PM5 sensor. A card is used to visualize the beams as they diffract off the hologram. The hologram is recorded on uncoated photoresist. Upper right hand image shows all address and diffracted beams. Series of images starting with upper left show intersection of diffracted beams with a card parallel to the surface and displaced normal to the surface at several distances. Image at 1.3 cm shows probe volume where two beams cross .....	57

Fig. 34.	Calibration channel optical setup and seeding arrangement for compressed air driver .....	58
Fig. 35.	Center channel velocity measured by PM5, pitot tube and calculated using Eq. 8 as a function of measured pressure differential. The distance between pressure taps $L = 148$ cm and 61 for data below and above 10 mm Hg respectively. Pressure readings taken with $L = 61$ cm were linearly scaled to represent the pressure reading at $L = 148$ cm .....	60
Fig. 36.	Comparison of PM5 sensor data measurements using conventional hot wires in calibration channel at UCI .....	60
Fig. 37.	Mean velocity measurements as a function of position in calibration channel. a) Line is fit using one-seventh power law (Eq. 8), error bars represent RMS deviation. b) Fit using exponent, $x$ , as fitting parameter and smoothed over 1 mm aperture. ( $V_o = U_d$ ) .....	61
Fig. 38.	Comparison of PM5 and RR50 data taken with and without the Acousto-optic modulator and on different days .....	62
Fig. 39.	RR50 sensor data plotted in normalized coordinates and shown with law-of-the-wall fit. Two different methods were used to obtain skin friction .....	64
Fig. 40.	(a) Two beam RR50 sensor having both long and short period gratings. (b) Single beam RR50 where probe volume is defined by overlap of receiver and address beam. Size of probe volume is reduced with receiver at 20 degree angle .....	65
Fig. 41.	Optical arrangement for testing of FAN sensor in the UCI calibration channel .....	66
Fig. 42.	Probability density function for normalized skin friction measurement in 3/4" channel with $u_{cl} = 10$ m/s .....	66
Fig. 43.	Comparison of FAN sensor data with RR50 boundary layer survey data. 3/4" channel with $u_{cl} = 10$ m/s .....	67
Fig. 44.	Measured burst frequency from the FAN sensor as a function of receiver alignment. Circles are data taken using 100-micron fiber and triangles represent 50 micron fiber data. Diagram on top helps to illustrate three regions: Low region - fan is not completely formed, Mid region - valid sensor region, High region - outside laminar sublayer .....	68
Fig. 45.	Shear stress measured using FAN sensor as a function of differential pressure measured between taps separated by 24" in 1/4" channel. Increasing pressure corresponds to higher flow rates. Line indicates theoretical mean shear stress calculated from Eq. 44 .....	69
Fig. 46.	RMS values for measured by FAN sensor as a function of shear stress. RMS values correspond to data shown in Fig. 36 .....	69
Fig. 47.	Flat Plate Model .....	74
Fig. 48.	TGF Wind Tunnel Diagram .....	76

Fig. 49.	TGF Optically Smart Surface Transmitter, receiver and model - Installation Photo .....	83
Fig. 50.	PM5 Freestream Velocity Measurements. M - 0.3 - 0.85 .....	84
Fig. 51.	PM5 Boundary Layer Profile Measurement at M - 0.4 .....	85
Fig. 52.	Fan Fringe Sensor Velocity Gradient Measurement ( $du/dy$ ) for M - 0.3 - 0.8 .....	87
Fig. 53.	Multiple probe volume reconstruction using volume holographic media. Angular change between reconstruction beams is not necessary if different colors are used .....	88
Fig. 54.	Holographic implementation of Fan fringe sensor. Drawing illustrates multiplexed recording to produce rotating fan. Stationary fan can be made with a single reference/reconstruction beam .....	89

## LIST OF TABLES

Table 1.	Focal characteristics of transmitter .....	17
Table 2.	Relationship between spin speed and attenuation of anti-reflection material.....	33
Table 3.	Recording schedule for 8"X10" Holographic plate and diffraction efficiency for embossed Mylar holograms - PM5 sensor. Recorded 28 Mar 93.....	36
Table 4.	Recording schedule for 8"x10" Holographic plate and diffraction efficiency for embossed Mylar and nickel shim holograms - RR series. Recorded 25 Mar 93.....	38
Table 5.	Experimental uncertainties arising from optical alignment and their contribution to frequency measurement and probe volume position. These are systematic errors. ....	71
Table 6.	Survivability test conditions .....	72



## ACKNOWLEDGEMENTS

The work reviewed in this report was due to the combined efforts of many individuals. Optically smart surface technology has and will continue to evolve due to the contributions of these people.

The authors wish to acknowledge the following: Mr. John Swienton for his dedication and hard work on all aspects of the Phase II effort, Mr. Fred Unterseher for his contributions in resist coating techniques, holographic recording and embossing, Dr. John LaRue and Mr. Kurt Novac of the University of California, Irvine, for their involvement in the conceptual design, data interpretation and support during the UCI testing effort, Mr. David Rosenthal for his contributions during Phase I, Dr. Cecil Hess for his contributions in the conceptual design of the LV and FAN sensors, Mr. Joseph Hsu for his help in theoretical fluid mechanics, Mr. Kurt Olsen of CFC Applied Holographics for his assistance in the shimming and embossing process, and Ms. Christina Arnold and Mrs. Marlayne Giron for their expert assistance in contractual administration and document preparation.

The authors would especially like to thank Ms. Linda G. Smith of Wright Laboratory for her contributions in the conceptual designs, interpretation of experimental data, orchestration of the TGF testing, and invaluable assistance in presenting and promoting this work within the Air Force and the aero diagnostics community. The authors also owe thanks to Mr. Glen Williams of Wright Laboratory for his help during the TGF testing and Dr. George Seibert of Wright Laboratory for his encouragement from the very beginning of the idea.

## 1.0 PROJECT SUMMARY

An Optically Smart Surface (OSS) is a holographic optical element (HOE) that is located on the surface of an object for the purpose of making an optical measurement. Upon reconstruction with a reference laser beam, the hologram forms a real image that can be used to detect surface or near surface physical parameters.<sup>1</sup> In this program, Optically Smart Surfaces were examined for use on aerodynamic wind tunnel models and aircraft. Several types of sensors were considered during the Phase I work including laser velocimeters (LV), surface strain gauges, and boundary layer transition sensors.<sup>2</sup> Initially, all these designs were considered during Phase II; however, after initial meetings with Wright Laboratory aerodynamic engineers, it was decided to focus the Phase II work on the LV sensors.

A laser velocimeter can be made by holographically recording the image of two intersecting laser beams, forming a probe volume where they cross.<sup>3</sup> When played back, the diffracted light from the hologram forms the real image of two laser beams crossing, and thereby constructs a laser velocimeter probe volume. Fig. 1 illustrates the conceptual implementation of the smart surface LV sensor. In its general form, the sensor resides on a curved surface and is replayed using a simple collimated beam.

The smart surface LV sensor has several advantages over conventional LV techniques:

1. It relies on forward scattered light intensity instead of the weaker, backscattered light which may be several orders of magnitude smaller,
2. It requires optical access from only the side of the model where measurement nodes are located,
3. The probe volume may be placed extremely close to the surface (limited only by beam waist size), and
4. The probe volume height is independent of the model position so motion of the model due to vibration or drift does not affect the position of the sample volume relative to the surface of the model.

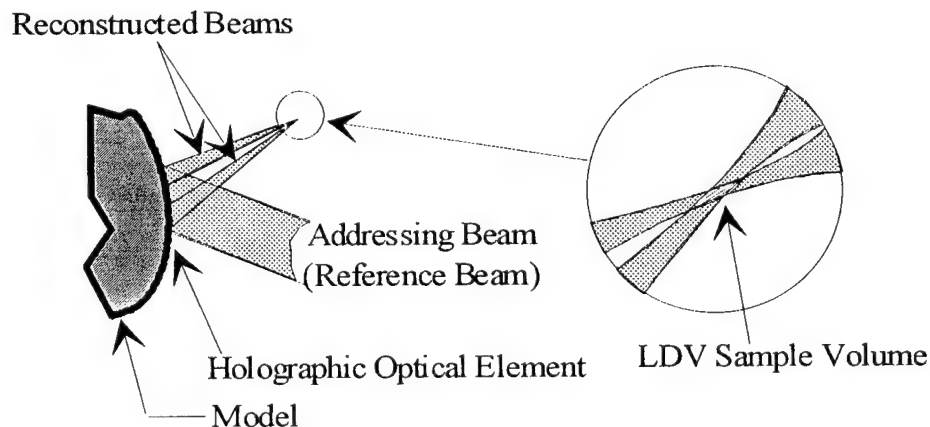


Fig. 1. Conceptual layout and replay of Optically Smart Surface Laser Velocimeter Sensor.

The aerodynamics measurement community is particularly interested in measuring velocity as a function of distance with respect to the surface normal to characterize the boundary layer region of the flow. This interest fueled the requirements for sensor design during Phase II. Two holographic designs were chosen that permitted measurements from 50 microns to 10 centimeters above the surface: the PM5 and the RR50. These sensors were recorded at MetroLaser on photoresist coated glass substrates. These substrates were then coated with aluminum to enhance reflectivity. Fifteen sensors were recorded on a single, large substrate (8" x 10") that was then used to grow a nickel shim. From this grandparent shim other shims were grown. Second generation shims were then used to stamp replicas into aluminum coated Mylar to produce rolls of smart surfaces. The Mylar, nickel and glass sensors were then tested at MetroLaser and at the University of California, Irvine (UCI). The best performance was obtained from the nickel shims because of their flatness and durability.

The PM5 sensor was tested in a calibration channel at UCI and its measurement accuracy validated against conventional sensors (hot wire and pitot) pressure. The useful range of the sensor was verified to be from 3 mm to 100 mm from the surface. Separate tests performed at the Wright Laboratory (WL) demonstrated that the sensors could survive sustained operation at MACH 3.

The PM5 was also tested at WL in the Trisonic Gasdynamics Facility (TGF). In the TGF, freestream velocity measurements were made from Mach 0.3 to 0.85. A boundary-layer survey was also made at Mach 0.4 on a flat plate model.

The RR50 sensor was tested in the UCI calibration channel. Measurements made at a distance greater than 5 mm from the wall were verified against conventional sensors. The sensor was used to make measurements in the boundary-layer laminar sublayer at centerline velocity of 10 m/s at heights down to 0.05 mm.

A third sensor, known as the fan fringe sensor, was also developed. This sensor measures the velocity gradient within the laminar sublayer by forming a fan of interference fringes that intersect at the surface of the sensor. Measurement of Doppler bursts occurring anywhere in the sublayer permit calculation of velocity gradient and hence skin friction (for Newtonian fluids). Because of its unique requirement that the fringes intersect at the surface, it is not possible to use a HOE located on the surface. Instead, the HOE must be located beneath the surface, on the backside of a transparent substrate. The fan-fringe sensor was successfully tested in the UCI calibration channel and measurements were validated for shear stress readings up to  $2 \text{ N/m}^2$ .

Smart surface technology is currently pending US patents which were filed during the Phase II program. In addition to the flat surface sensors that were developed, it was also demonstrated that HOEs could be recorded on curved surfaces using phase conjugate compensation during the recording process. Preliminary designs were made for additional "behind-the-surface" sensors that, if implemented, could dramatically increase the capabilities of this technology.

## 1.1 Analytical Proof-of-Concept

### 1.1.1. General Equations

In this section the basic design equations for holographic sensors are developed. We show analytically that a hologram can be designed, constructed and placed on an arbitrary surface of a model such that when it is addressed by a beam of light, a second wavefront of any desired form will emerge through the process of diffraction. Moreover, the equations demonstrate that useful information about the model or the environment can be impressed upon the emerging beam of light, making the hologram act as a sensor of the information. The general analysis is amenable to the addition of real effects which characterize a real and practical case, and such effects are examined.

The equations predict the amplitude, phase, and direction of a beam of light returned from the holographic surface after having been addressed by an input beam. Fig. 2 provides the geometry and definition of terms and components involved.

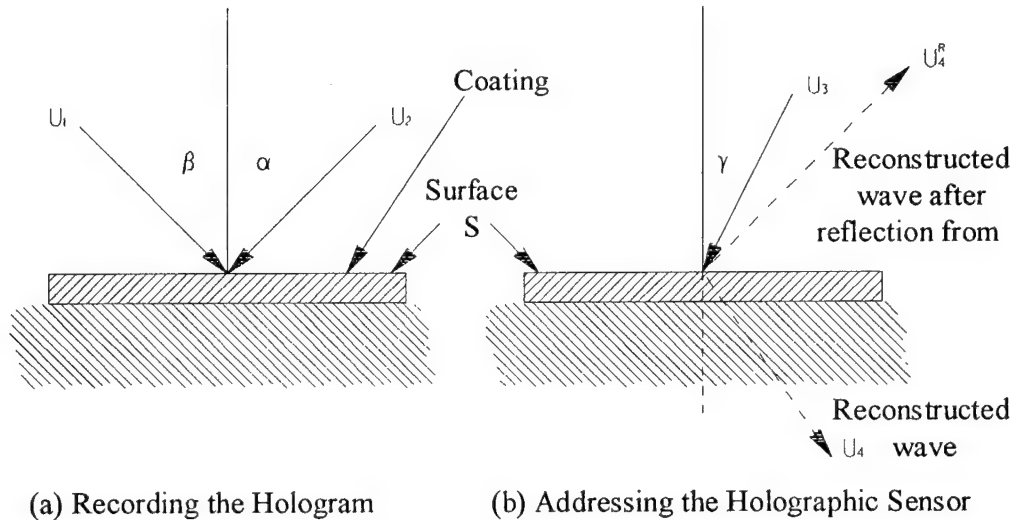


Fig. 2. Geometry of Holographic Sensor Equations.

A light wave from a laser passes from a transmitter through a volume of interest to a general surface of arbitrary shape. This shape could, for example, represent a sensor located on any place on a model surface in a wind tunnel. The amplitude of the wavefront at the surface can be written as the sum of two coherent light waves having  $u_1$  and  $u_2$  (amplitudes).

$$u(x) = u_1 + u_2 \quad (1)$$

Where  $u_1$  and  $u_2$  can be thought of as an object wave and reference wave respectively, and  $x$  is the distance in one axis of the hologram. For simplicity, the analysis is limited to one dimension in the hologram.

The resulting waveform has an intensity given by:

$$I(x) = uu^* \quad (2)$$

$$= |u_1|^2 + |u_2|^2 + u_1u_2^* + u_1^*u_2$$

where  $*$  denotes the complex conjugate, and  $||$  denotes the absolute value.

After processing, we assume that the transmissivity of the hologram is proportional to the original exposure, so that

$$u_4 = H I(x)u_3 \quad (3)$$

where  $u_3$  is the address beam, and  $H$  is a constant.

$$u_4 = Du_3 + Hu_1u_2^*u_3 + Hu_1^*u_2u_3 \quad (4)$$

$$\text{Where } D = H(|u_1|^2 + |u_2|^2)$$

Notice that the second term in Equation (4) is proportional to the original object wave,  $u_1$ , used to form the hologram. The wave represented by the third term is its conjugate. Either of the two waves contains all of the information of the original object wave. Therefore, whatever the original wave is, whether it be a simple plane wave or a combination of many waves, it can be synthesized by addressing the hologram. Also note that the behavior of the reconstructed wave is independent of the shape of the surface, since the only variable,  $x$  is assumed to lie in the surface, and no assumption has yet been made about the shape of the surface. This proves the first step required for holographic sensors for the ideal case.

Equation 4 is a completely general expression which states that the reconstructed beam  $u_4$  produced by the addressing beam  $u_3$  has three components, one which is proportional to  $u_3$  (the first term), a second which is proportional to  $u_2^*$  (the second term), and one which is proportional to  $u_2$  (the last term). Indeed, if the address beam  $u_3$  is the same as  $u_1$ , then:

$$u_4 = Du_3 + H|u_1|^2u_2^* + H|u_1|^2u_2 \quad (5)$$

An important fact to note is that  $u_2$  and  $u_2^*$  exist in the plane of the hologram and are traveling toward the surface. Then, with most of our sensors, the surface is reflective and reflects the wave according to the law of reflection (angle of incidence equals angle of reflection). Consequently, the wavefront will be modulated by the curvature of the surface. If the transmitted wave is used and reflection does not take place, then the surface curvature is of no concern.  $u_2$  can be any arbitrary wavefront or collection of wavefronts. For example, it may comprise one or more pair of focusing, crossing, laser velocimeter beams that produce one or more sample volumes anywhere in space. Or it may comprise one or more beams for use in flow visualization or interferometry.

### Holographic Sensor Equations

Now we proceed to specialize the above equations and develop the equations and logic for specific holographic sensors. We first write the equation for the hologram which has been applied

to the model surface. This predicts the amplitude, phase, and direction of a beam of light returned from the surface after having been addressed by an input beam.

We now assume that all of the beams used here are collimated beams so they can be written as:

$$\begin{aligned} u_1 &= A \exp(ikx \sin \beta) \\ u_2 &= B \exp(ikx \sin \alpha) \\ u_3 &= C \exp(ikx \sin \gamma) \end{aligned} \quad (6)$$

using Equations 4 and 5, we find that

$$\begin{aligned} u_4 &= Du_3 + E \exp(ikx(\sin \beta - \sin \alpha + \sin \gamma)) \\ &\quad + E \exp(ikx(-\sin \beta + \sin \alpha + \sin \gamma)), \end{aligned} \quad (7)$$

where  $k=2\pi/\lambda$ . Where  $E = ABCH$ .

### Incorporating Physical Properties

Now we desire to incorporate the physical properties of the recorded hologram. Rewriting Equation 7

$$\begin{aligned} u_4 &= Du_3 + E \exp((i2\pi x(\sin \beta - \sin \alpha)/\lambda) + (i2\pi x(\sin \gamma)/\lambda)) \\ &\quad + E \exp((i2\pi x(-\sin \beta + \sin \alpha)/\lambda) + (i2\pi x(\sin \gamma)/\lambda)) \\ u_4 &= Du_3 + E \exp(i2\pi x(f_{OS} + (\sin \gamma)/\lambda)) \\ &\quad + E \exp(i2\pi x(-f_{OS} + (\sin \gamma)/\lambda)), \end{aligned} \quad (8)$$

where

$$f_{OS} = (\sin \beta - \sin \alpha) / \lambda, \quad (9)$$

represents the spatial frequency of the holographic grating in the surface at a time  $t_0$ .

When the surface expands for any reason (thermal or stressing), the grating frequency changes from  $f_{OS}$  to some value  $f_{IS}$ . We can represent the change for thermal expansion as

$$f_{IS} = f_{OS} / (1 + K\Delta T) = (\sin \beta - \sin \alpha) / \lambda (1 + K\Delta T) \quad (10)$$

where  $K$  is the thermal expansion coefficient. So

$$\begin{aligned} u_4 &= Du_3 + E \exp(i2\pi x((\sin \beta - \sin \alpha)/\lambda(1+K\Delta T) + (\sin \gamma)/\lambda)) \\ &\quad + E \exp(i2\pi x(-(\sin \beta - \sin \alpha)/\lambda(1+K\Delta T) + (\sin \gamma)/\lambda)) \end{aligned} \quad (11)$$

If we address the sensor with two different beams, then four wavefronts described by Equation 11 emerge, two coming from each addressing beam  $u_3$  and  $u_3'$ . Let us make a holographic sensor in which the geometry is simplified in the following way: One of the two forming waves is normal to the hologram. During reconstruction we use two waves which are symmetrical about the normal and at the same angle as the second wave used to form the hologram. Finally, let us observe only the reconstructed waves which emerge normal to the hologram. Mathematically these assumptions can be stated as follows:

$$\begin{aligned}
u_3 &\sim \text{let } \alpha = 0, \gamma = \beta \\
u_3' &\sim \text{let } \alpha = 0, \gamma = \beta \\
u_4 &= Du_3 + E\exp(i2\pi x((\sin\beta)/(\lambda(1+K\Delta T)) + (\sin\beta)/\lambda)) \\
&\quad + E\exp(i2\pi x(-(\sin\beta)/(\lambda(1+K\Delta T)) + (\sin\beta)/\lambda)) \\
u_4' &= Du_3' + E\exp(i2\pi x((\sin\beta)/(\lambda(1+K\Delta T)) + (\sin\beta)/\lambda)) \\
&\quad + E\exp(i2\pi x(-(\sin\beta)/(\lambda(1+K\Delta T)) + (\sin\beta)/\lambda))
\end{aligned} \tag{12}$$

Two of the components emerge from the hologram exactly at normal when the temperature change is zero and nearly normal at increasing temperature. The appropriate components can be easily identified in equation 12 by setting  $\Delta T = 0$ . From Equation 12, they are

$$\begin{aligned}
u_{4C} + u_{4B} &= E(\exp(i2\pi x(\sin\beta/(1+K\Delta T)-\sin\beta)/\lambda) \\
&\quad + \exp(-i2\pi x(\sin\beta/(1+K\Delta T)-\sin\beta)/\lambda)) \\
u_{4C} + u_{4B} &= 2E\cos(2\pi x(\sin\beta/(1+K\Delta T)-\sin\beta)/\lambda)
\end{aligned} \tag{13}$$

Where the notation C and B refer to the specific near normal wavefronts that have been chosen from all possible wavefronts in Equation 12.

The intensity, I is

$$I = 4E^2 \cos^2((2\pi x/\lambda)(\sin\beta)(K\Delta T)/(1+K\Delta T)) \tag{14}$$

The sensitivity of the measurement of  $\Delta T$  can be expressed in the number of fringes present in the reconstructed beam pair. The intensity at the edge of the sensor is:

$$I = E^2 \cos^2((2\pi r/\lambda)(\sin\beta)(K\Delta T)/(1+K\Delta T)) \tag{15}$$

where  $r$  is the sensor radius. The intensity changes from maximum at  $r = 0$  to zero when

$$(r/\lambda)(\sin\beta)(K\Delta T)/(1+K\Delta T) = 1/4$$

or

$$\begin{aligned}
\Delta T &= \lambda(1+K\Delta T)/4rK(\sin\beta) \\
&\approx \lambda/4rK(\sin\beta), \text{ since } K\Delta T \ll 1
\end{aligned} \tag{16.}$$

for small angles

$$\Delta T \sim \lambda / 4rK\beta \quad (17)$$

Equation 15 expresses the intensity in terms of the expansion coefficient,  $K$ , and the parameter change,  $\Delta T$ .

Consider the case

$$\begin{aligned} K &= 0.0001/^{\circ}\text{C}^{-1} \\ \lambda &= 0.5 \times 10^{-4} \text{ cm (green light)} \\ r &= 1 \text{ cm} \end{aligned}$$

Then the detector can easily detect changes in  $\Delta T$  of

$$\Delta T = 0.125/\beta \text{ }^{\circ}\text{C}$$

For example, for  $\beta = 0.1$  radian, the detector can see

$$\Delta T = 1.25 \text{ }^{\circ}\text{C}$$

#### Temperature Sensor Equation

$$\begin{aligned} I &= 4E^2 \cos^2((2\pi r/\lambda)(\sin\beta)(K\Delta T)/(1+K\Delta T)) \\ \Delta T)_{I=0, x=r} &= \lambda/4rK\beta \end{aligned} \quad (18)$$

The equation can be generalized for strain measurement.

#### Strain Sensor Equation

$$\begin{aligned} I &= 4E^2 \cos^2((2\pi r/\lambda)(\sin\beta)(YS)/(1+YS)) \\ S)_{I=0, x=r} &= \lambda/4rY\beta \end{aligned} \quad (19)$$

where  $S$  is the stress and  $Y$  is the stress/strain coefficient of the sensor material.

The sensitivity of the measurements can be increased (decreased) by,

- (1) Choose a material for the sensor having large (small) coefficients  $K$  or  $Y$ .
- (2) Making  $\beta$  larger (smaller).

#### Practical Effects

To see how the sensor responds to a small tilt in angle as might be caused by vibration, we return to Equation 12 and generalize this equation to consider that a small tilt  $\epsilon$  of the sensor sets the following terms in the equation, see Fig. 3.



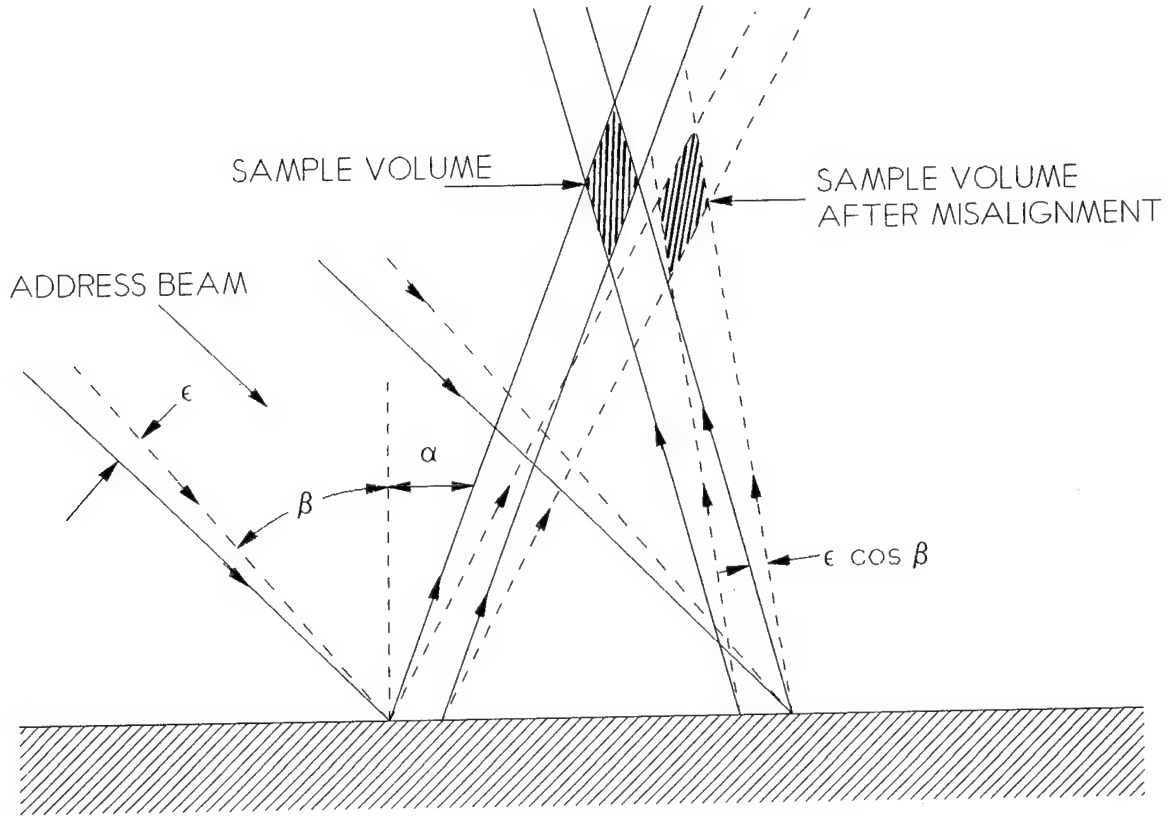


Fig. 3. Error in an LDV Sample Volume by Misalignment.

$$u_3 \sim \text{let } \alpha = 0, \gamma = \beta + \epsilon$$

$$u_3' \sim \text{let } \alpha = 0, \gamma = \beta + \epsilon, \text{ and } \gamma = -(\beta - \epsilon)$$

Assuming  $\epsilon$  is small, Equation 13 becomes

$$\begin{aligned} u_{4C} + u_{4B} = & E(\exp(i2\pi x(\sin\beta/(1+K\Delta T) - \sin(\beta+\epsilon))/\lambda)) \\ & + \exp(-i2\pi x(\sin\beta/(1+K\Delta T) - \sin(\beta-\epsilon))/\lambda)) \end{aligned} \quad (20)$$

Where once again the C and B notations refer to the waves which emerge nearly normal to the sensor. We disregard all of the other waves in the reconstruction.

$$\begin{aligned} u + u^1 = & E(\exp(i2\pi x(\sin\beta/(1+K\Delta T) - \sin\beta\cos\epsilon - \cos\beta\sin\epsilon)/\lambda)) \\ & + \exp(-i2\pi x(\sin\beta/(1+K\Delta T) - \sin\beta\cos\epsilon + \cos\beta\sin\epsilon)/\lambda)) \end{aligned} \quad (21)$$

$$\begin{aligned} u + u^1 = & E(\exp(i2\pi x(\sin\beta/(1+K\Delta T) - \sin\beta - \epsilon\cos\beta)/\lambda)) \\ & + \exp(i2\pi x(\sin\beta/(1+K\Delta T) - \sin\beta + \epsilon\cos\beta)/\lambda)) \end{aligned} \quad (22)$$

The intensity I

$$I = u^2 + u^{12} + uu^{1*} + u^*u^1, \quad (23)$$

The first two terms do not vary with x if uniform intensity waves have been used to record the holograms. The modulation caused by expansion of the surface is manifested in the last two terms. Namely,

$$I = 2E \cos((2\pi x/\lambda)(\sin\beta/(1+K\Delta T) - \sin\beta - \epsilon \cos\beta + \sin\beta/(1+K\Delta T) - \sin\beta + \epsilon \cos\beta)) \quad (24)$$

$$I = 2H \cos((4\pi x/\lambda)(\sin\beta/(1+K\Delta T) - \sin\beta)) \quad (25)$$

which is the same form as Equation 14. Note that the expression has no dependence on  $\epsilon$ . Therefore the sensor is not affected by vibration! Note that the condition

$$\gamma \sim \pm\beta$$

is an important prerequisite to this condition. The reason for the lack of dependence on alignment is that each of the reconstructed beams is shifted by the same amount by a small tilt in the sensor, so no effect is exhibited in the fringes.

#### Laser Velocimeter Sensor

We now consider reconstructed beams which cross over each other to form a sample volume with fringes. Returning to Equation 6, we desire to reconstruct two beams that will cross each other. So  $u_4$  and  $u_4'$  for two adjacent holograms could have phase terms equal and opposite to satisfy this requirement, let

$$\gamma = \beta + \epsilon$$

and

$$\gamma' = \beta + \epsilon$$

i.e., the address beam is almost the same as one of the recording beams. Now let

$$\begin{aligned} \alpha &= -\alpha' \\ \beta &= \beta' \end{aligned}$$

This will produce two beams that cross in space.

$$\begin{aligned} u_4 &= Du_3 + E \exp(ikx(\sin\beta - \sin\alpha + \sin(\beta + \epsilon))) \\ &\quad + E \exp(ikx(-\sin\beta + \sin\alpha + \sin(\beta + \epsilon))) \\ u_4' &= Du_3 + E \exp(ikx(\sin\beta + \sin\alpha + \sin(\beta + \epsilon))) \\ &\quad + E \exp(ikx(-\sin\beta - \sin\alpha + \sin(\beta + \epsilon))) \end{aligned} \quad (26)$$

Note that if  $\epsilon = 0$ , then the second terms of  $u_4$  and  $u_4'$  become two waves traveling at  $\pm \alpha$  with respect to the surface normal. These are the two crossing waves we want to examine further.

$$\begin{aligned}
u_s &= u_{42} + u_{42}' = E \exp(ikx(-\sin\beta + \sin\alpha + \sin(\beta + \epsilon))) \\
&+ E \exp(ikx(-\sin\beta - \sin\alpha + \sin(\beta + \epsilon))) \\
&= E \exp(ikx(-\sin\beta + \sin\alpha + \sin\beta \cos\epsilon + \sin\epsilon \cos\beta)) \\
&+ E \exp(ikx(-\sin\beta - \sin\alpha - \sin\beta \cos\epsilon + \sin\epsilon \cos\beta))
\end{aligned} \tag{27}$$

Where the sub 4 and 2 designation refers to the reconstructed beams that cross in space.

For small  $\epsilon$

$$\begin{aligned}
u_s &= E \exp(ikx(\sin\alpha + \epsilon \cos\beta)) \\
&+ E \exp(ikx(-\sin\alpha + \epsilon \cos\beta))
\end{aligned} \tag{28}$$

The intensity is

$$\begin{aligned}
|u_s|^2 &= 2E^2 + 2E \cos(kx(\sin\alpha + \epsilon\beta + \sin\alpha - \epsilon\beta)) \\
&= 2E^2 + 2E \cos(2kx \sin\alpha)
\end{aligned} \tag{29}$$

Note that in this approximation, the sample volume is not affected by misalignment of the address beam. This is a result of an  $\epsilon$  misalignment causing

$$\epsilon \cos \beta$$

angular change in both beams.

## 2.0 SMART SURFACES DESIGN

### 2.1 PM5 LV SENSOR

The optically smart surface laser velocimetry sensor designated PM5 produces a plus/minus 5 degree crossing angle from two beams incident at 50 degrees. Fig. 4 shows the arrangement for addressing the sensor. The sensor has the advantage of having a small crossing angle which results in a large scattered signal level and wide fringe spacing, producing a low Doppler frequency and high fringe contrast (good for high velocity measurements). Its disadvantages are an inherently low diffraction efficiency (approximately 30%), a need for careful alignment of the address beams, and multiple sample volumes that arise near the surface due to zero order and second order diffraction beams.

The alignment requirement for the address beams is that each should hit on its respective patch on opposite sides of the center line. The beams do not need to fall symmetrically about the center line, making alignment fairly simple for wide beam separations (large probe height); however, at small beam separations (low probe height), this requirement becomes more difficult. At low probe volume heights, the address beam separation is small and in addition to aligning the beams to either side of the center line, the quality of the hologram at the interface between the two patches also becomes an issue. Distortions due to edge diffraction effects present during the holographic recording, extend 300 to 500 microns across the interface, making this region unusable. The multiple sample volumes that arise from interference of the first, second, and zero order beams also occur near the surface. Because of these problems arising when using probe volumes near the surface, this sensor is restricted in its minimum usable height; however, its maximum height is restricted only by the physical sensor size. The current production design of the PM5 smart surface has a usable probe volume height range of 3 mm to 100 mm. Its dual address beam design also allows the flexibility of using frequency shifted beams for high speed or bi-directional (separated) flow.

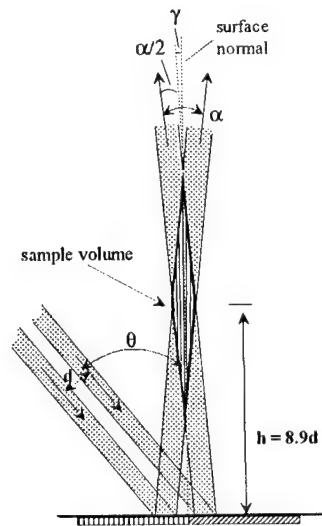


Fig. 4. PM5 sensor Playback arrangement. Nominally,  $\theta = 50^\circ$ ,  $\alpha = 10^\circ$ ,  $\gamma = 0$ .

## 2.2 SURFACE RR50 LV SENSOR

The principle of the RR50 is to retro-reflect 50% of the incident beam back onto itself while the other half of the beam propagates forward. The sample volume is formed between the zero order and first order beams as shown in Fig. 5. For incident angles greater than about 19 degrees (at 488nm) there is one and only one diffracted order. This results in only one sample volume on the surface. In addition, almost 100% of the reflected light is directed into the probe volume (some light does get absorbed or scattered by imperfections on the surface). The major drawback of this design is the requirement of nearly a 40-deg. crossing angle, producing a small fringe spacing which leads to a high Doppler frequency. Fortunately, the flow velocity near the surface, i.e., in the boundary layer, is approaching zero so the Doppler frequency should be within the limits of the electronics.

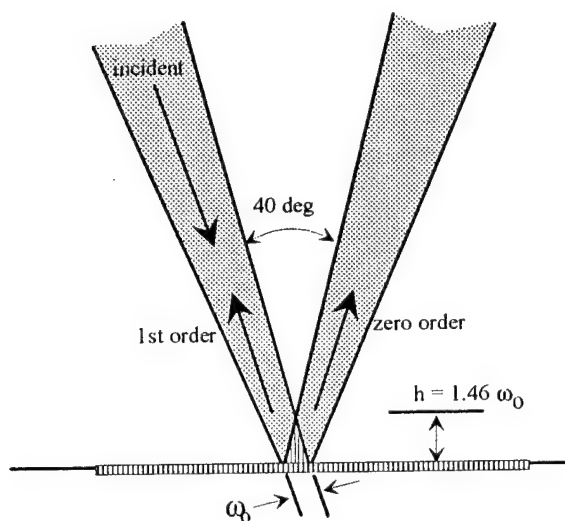


Fig. 5. RR50 sensor shown in the single beam, surface measurement configuration.

The sensor is addressed by a single beam that can fall anywhere on the hologram, making alignment extremely simple. The most stringent alignment requirement is that the beam must be focused on the surface within the Rayleigh length. The probe volume height is roughly equal to the waist of the focused spot, so the minimum height is governed by the focal spot size and alignment tolerance. Below 100 microns the alignment tolerance falls below 1 cm which, although possible, presents significant difficulties since factors such as the refractive index of the windows come into play. Since probe heights are increased by increasing the sample volume size, the upper height limit is a function of the maximum allowable volume. Also, the single address beam means that frequency shifting is not possible in this design so that it cannot monitor flow reversals and is limited in its velocity range by electronics.

## 2.3 MID-RANGE RR50 LV SENSOR

The RR50 is also capable of operating in an off-surface mode similar to the PM5. Two parallel address beams are incident on the surface and the probe volume is formed by the interference of the first order retro-reflection of the first beam with the zero order reflection of the second beam. If this is done out-of-plane see Fig. 6, the resulting sample volume will form in a region free from

other beams. Key features of this design are that (1) the parallel beams can be incident anywhere on the hologram, making alignment simple, (2) frequency shifting is possible, allowing measurement of flow reversal and compensation for high velocity flow and (3) the steep address angle allows the probe volume to be placed very close to the surface. The drawbacks to this design are that a maximum of 50% of the light reaches the probe volume (which is better than the PM5), and the wide crossing angle results in small fringe spacing as discussed previously. In theory, the probe volume can be placed right on the surface; however, there will be a large amount of scattered light from the other 50% of the light in the extra beams. At the surface, each beam will form a sample volume identical to the surface LV (i.e. stationary fringes the size of the beam waist). Because frequency shifting can be used, the scattered signals from the stationary fringes or single beams may be filtered electronically. However, the dc optical signals cannot be filtered from the photomultiplier tube (PMT), and care must be taken to ensure that these signals do not saturate the detector or swamp out the desired signal. The minimum achievable beam separation of two focusing parallel beams and the unwanted scattering signals will ultimately govern how close to the surface the probe volume can be placed.

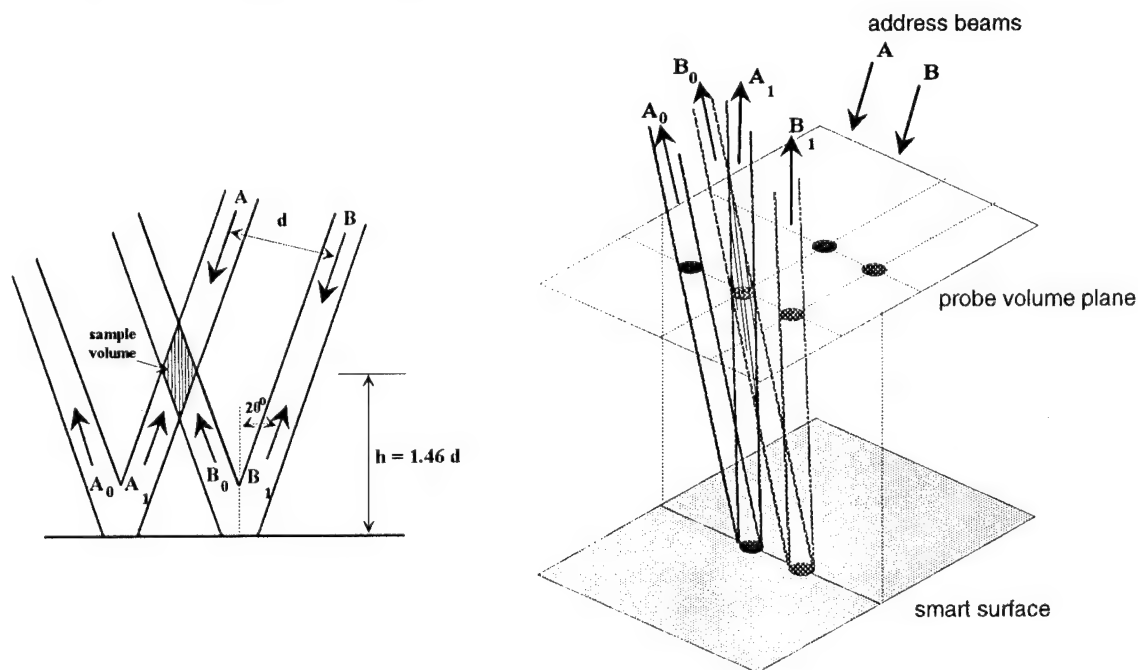
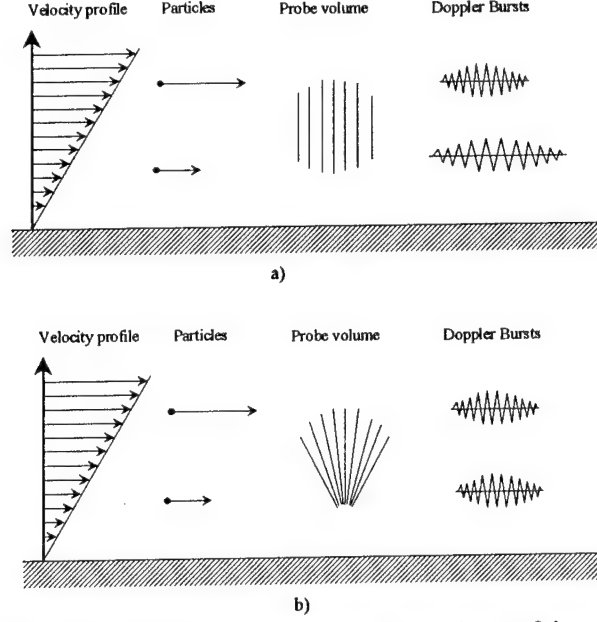


Fig. 6. RR50 sensor shown in the "off-surface" configuration. The probe volume and the address beams can be contained in a single plane or can be out of plane as shown in the 3-D representation.

## 2.4 FAN SENSOR

One possibility for measuring aerodynamic shear stress on the model surface is to measure the velocity gradient near the surface. A unique way to directly measure this velocity gradient was proposed and demonstrated by Naqwi and Reynolds.<sup>4</sup> The method uses a set of fringes that form a fan rather than a linear array. Fig. 7 illustrates the conventional and fan type of fringe measurements.



**Fig. 7. Doppler bursts near the surface for a) conventional linear fringe probe volume and b) fan fringes of velocity gradient sensor.**

We have designed a FAN sensor based on the fan-fringe concept for measuring velocity gradients in the laminar sublayer. The FAN sensor is given this name because the fringes produced are not parallel but come out radially from a point on the surface of the hologram. This sensor measures velocity gradients which can be used to calculate aerodynamic shear stress on the model surface. This OSS sensor reproduces the fan fringes when played back via a single address beam.

Assuming a linear velocity gradient approaching the wall, the Doppler signal produced from the fan fringes is identical for all positions above the surface. The velocity gradient can be found from<sup>4</sup>

$$\frac{\partial u}{\partial y} = f_D \frac{d\Lambda}{dy}, \quad (30)$$

where  $f_D$  is the Doppler frequency,  $\partial u / \partial y$  is the velocity gradient normal to the surface, and  $d\Lambda / dy$  is the change in fringe spacing as a function of height. For the case of two cylindrical sources located on the surface, the slope of the fringe spacing is given by

$$\frac{d\Lambda}{dy} = \frac{\lambda}{S}, \quad (31)$$

where  $\lambda$  is the wavelength of light and  $S$  is the distance between sources. Substituting Eq. 31 into Eq. 30 we arrive at

$$\frac{\partial u}{\partial y} = f_D \left[ \frac{\lambda}{S} \right]. \quad (32)$$

Because the wavelength and the slit spacing are fixed parameters of the holographic recording, the Doppler burst frequency provides a direct measurement of the velocity gradient. The value of this sensor is realized in the fact that for Newtonian viscous flows, the shear stress is linearly proportional to the velocity gradient at the surface, i.e.,

$$\tau_w = \mu \left( \frac{\partial u}{\partial y} \right)_w \quad (33)$$

The constant of proportionality,  $\mu$ , is the viscosity of the fluid.

Recreating the image of two line sources is straightforward to do holographically; however, it is necessary to have the images appear exactly at the surface so that the fringe spacing approaches zero at the wall. The hologram must be located underneath the surface so that the reconstructed images form at the surface. Ensuring that the image forms exactly at the surface makes this a technically challenging hologram to record. However, once recorded properly, reconstruction can be accomplished by simply illuminating with a raw or slightly focusing laser beam, eliminating almost all the optics. Using the holographic sensor also overcomes the current necessity of having optical access from behind the model. Fig. 8 shows how the hologram is replayed and the fan fringes are formed.

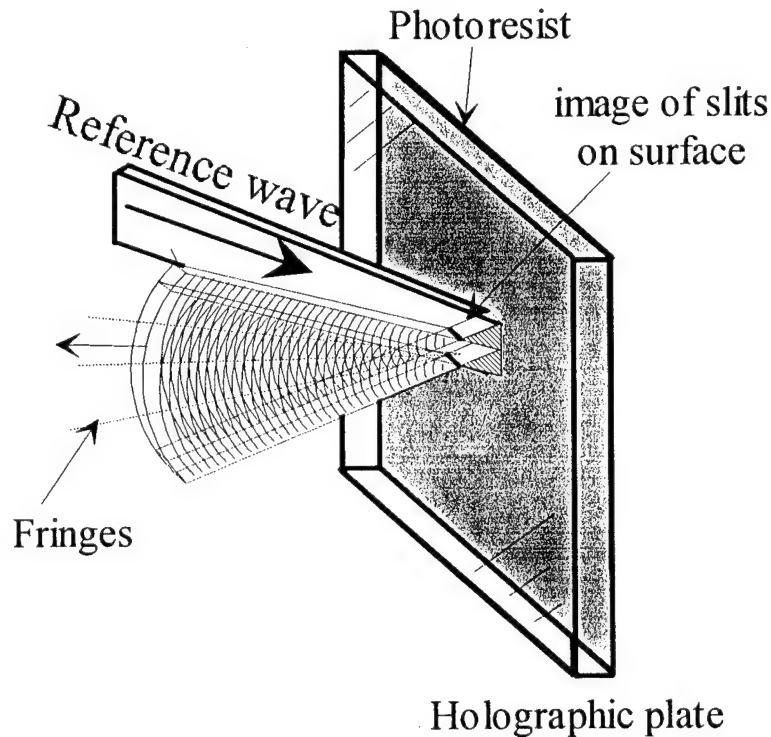


**Fig. 8. Reconstruction of FAN sensor.** Diffraction of incident light off silvered back surface produces real image of two slits on front glass surface. Reference beam is incident in horizontal plane and fan fringes are reconstructed in the vertical plane.



## 2.5 TRANSMITTER DESIGN

### 2.5.1 OPTICAL DESIGN

The optical reference system is separated into two parts: the transmitter and the collection optics; both of which are mounted on separate mounting plates. Once the transmitter and receiver are internally aligned, both enjoy freedom of movement with alignment only necessary between the transmitter or receiver and the smart surface. The transmitter and receiver both have translation stages which are motor driven and computer controlled. The primary collection lens of the receiver is moved in concert with the beam combiner of the transmitter so that the receiver focal point tracks the movement of the probe volume produced by the separation of the address beams.

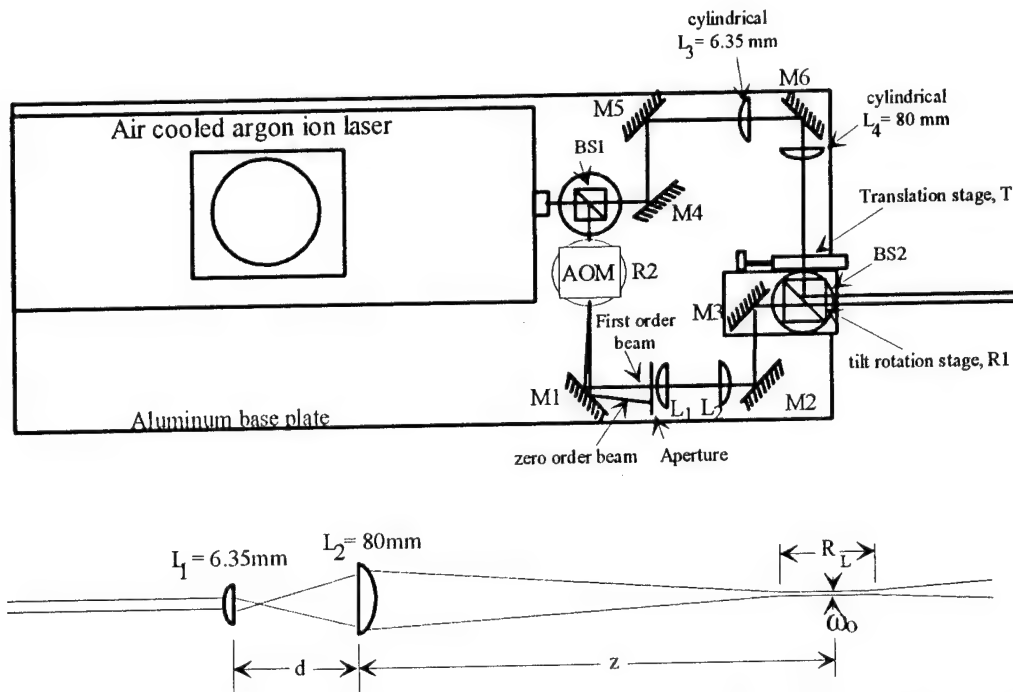


Fig. 9. Design of OSS transmitter. M - mirror, R - rotation stage, BS - beam splitter, L - cylindrical lens, AOM - acousto-optic modulator.

The basic function of the transmitter is to produce two parallel beams with identical beam waists ( $\omega_0$ ) at the hologram. Waist sizes of  $50\ \mu\text{m}$  produce probe volumes of  $450\ \mu\text{m}$  and  $75\ \mu\text{m}$  in length on the PM5 and RR50 holograms, respectively. The transmitter is all located on one mounting plate and includes laser, beamsplitter, Bragg cell, and beam combiner as schematically illustrated in Fig. 9. The laser source used was an air-cooled argon ion laser with  $P=100\ \text{mW}$  and  $\lambda=488\ \text{nm}$  from Omnicrome. Other design parameters of the transmitter are as follows: (1) the optical path lengths of each arm, from BS1 to BS2, are equal including allowance for index-of-refraction inside the acousto-optic modulator (AOM), (2) the physical path length from AOM to L1 is greater than  $10\ \text{cm}$  so that zero order light can be blocked, (3) the physical distance from L1 and the distance between L3 and L4 is adjustable between  $85\ \text{mm}$  and  $100\ \text{mm}$  to allow the distance between transmitter and test model to extend approximately from  $0.46\text{-m}$  to past  $1.5\ \text{m}$ ,

(5) lenses are adjustable perpendicular to the beam direction and can be rotated in angle. In addition, because of the optical path matching condition, the AOM must be left in place even when not in use to frequency shift the beam. The AOM is mounted upon a rotating stage to allow for precision tuning of the Bragg matching angle. The optical components were purchased from Thorlabs, Newport Corp., Melles Griot and Isomet.

Table 1 lists the focal characteristics of the new transmitter where the measurement parameters are shown in Fig. 7. The Rayleigh length represents the tolerance in the alignment of the transmitter distance from the surface to ensure that the focus is at the probe volume.

**Table 1.**  
**Focal characteristics of transmitter**

z, focal length	2 ft	3.1 ft	3.5 ft
$\omega_0$ , beam waist	47 $\mu\text{m}$	77 $\mu\text{m}$	86 $\mu\text{m}$
$R_L$ , Rayleigh length	3.6 mm	9 mm	12 mm

## 2.5.2 TRANSMITTER ALIGNMENT

### Transmitter Optics

The following procedure is recommended for alignment of the transmitter optics. Refer to Fig. 7 for the location of components being adjusted.

- 1) Remove the cylindrical lenses; there are four (L1, L2, L3, L4).
- 2) Remove the beam combiner cube (B52).
- 3) Center the combiner traverse (T), used to move B52 and M3 and thus change beam spacing.
- 4) Align path B51-AOM-M1-M2-M3 (left path).
  - a) Align two irises with the combiner traverse (T) so that they define a line parallel to the direction of travel of the traverse and at the height of the laser beam.
  - b) Block one beam path at M5. Adjust M1 so that the beam is centered on the first iris. Adjust M2 so that the beam is centered on or gets closer to the second iris. Repeat these steps until the beam is simultaneously centered on both irises. Now remove these irises.
- 5) Align path B51-M4-M5-M6-B52 (right path).
  - a) Put one iris near the combiner traverse (T) so as not to interfere with installing the combiner cube, B52, and align the iris with the beam.
  - b) Mark a point several feet from the iris that the beam intersects.
  - c) Square up the cube with its base and mount it on the traverse (T). Adjust the cube so that the beam still goes through the iris and intersects the point marked in step 5b above.

- d) Block the beam at M1, and unblock the beam at M5. Adjust M5 such that the beam goes through the iris. Adjust M6 until the beam intersects the point marked in step 5b above. Repeat these steps until the beam simultaneously passes through the iris and intersects the point marked.
  - e) Remove the iris.
- 6) Lens alignment in the left path.
  - a) Block the right path at M5.
  - b) Install lens L2 and center it with the beam. Rotate L2 until the beam exiting B52 is horizontal.
  - c) Install lens L1 and align it so it is centered on the beam. Rotate L1 until the beam exiting B52 is horizontal.
  - d) Move lens L1 so that the beam is focused at a point equal to the model distance.
- 7) Lens alignment in the right path.
  - a) Block the left path at M1 and unblock the right path at M5.
  - b) Install lens L4 and center it with the beam. Rotate L4 until the beam exiting B52 is horizontal.
  - c) Install lens L3 and align it so it is centered on the beam. Rotate L3 until the beam exiting B52 is horizontal.
  - d) Move lens L3 so that the beam is focused at a point equal to the model distance.
- 8) The focal points of the two beams should now be very close to being convergent. Use the adjustments on the combiner cube B52 to make fine adjustments on the convergence. When correctly aligned, the image should have a slight flicker to it when AOM is not used.

Other things to consider when setting up an OSS LV test are as follows. The optical path length of the acousto-optic modulator (AOM) is about 3 cm, one and one-half times the physical enclosure length. This length, rather than the physical length must be used when determining the path matching requirements. The coherence length of the laser (Omnichrome, argon, 100 mW) is 6 cm. This requires that the pathlength difference in the transmitter be much less than this.

Care must be taken in selecting the correct diffracted order coming out of the AOM. The correct beam to select for a positive frequency shift is the diffracted order located opposite the electrode from the zero order beam. For the geometry shown in Fig. 10, the correct beam is to the right of the zero order. Likewise, it is very important which of the two parallel beams striking the OSS sensor is the shifted beam, since this determines the direction the fringes are moving. Fig. 11 illustrates the two possible orientations for the shifted and unshifted beams with respect to flow direction.

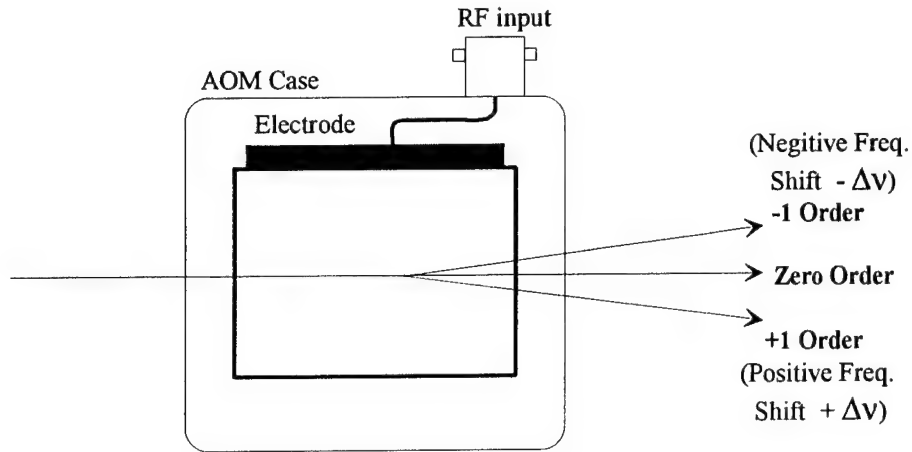


Fig. 10. Relationship between sign of frequency shift and direction of diffracted order.

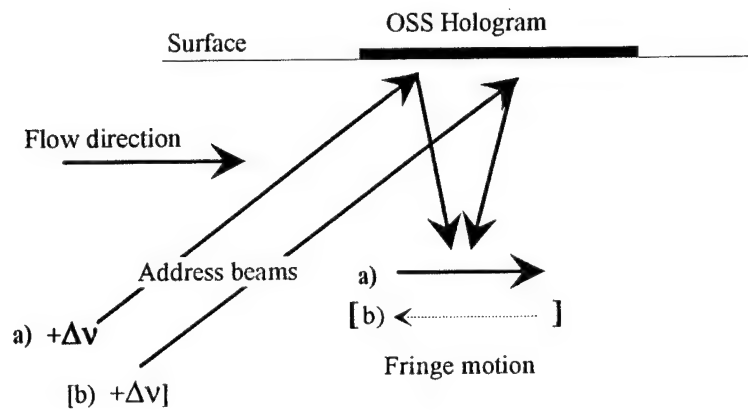


Fig. 11. Relationship of direction of fringe motion with frequency shift. Case a) positive frequency shift on upstream address beam results in fringe motion in same direction as flow. Case b) positive frequency shift in down stream address beam results in fringe motion opposing flow direction.

#### Transmitter and OSS alignment.

Once the transmitter optics have been aligned, the entire transmitter can be positioned with respect to the OSS. The following steps should be done before the receiver final alignment. (The receiver internal optical alignment can be done prior to this.)

- 1) Position transmitter at nominal angle for each sensor (RR50 = 20 deg. PM5 = 55 deg).
- 2) Alignment of Model and OSS:
  - a) Adjust angle of OSS plug and/or model to ensure that the *reflected* beam is contained in the plane of incidence of the address beams.
  - b) Adjust rotational angle of OSS plug to ensure that the *diffracted* beam is contained in the plane of incidence of the address beams.

- 3) Ensure that beams are fully overlapping ( $d = \text{zero}$ ). If Bragg shifting is desired, AOM should be on and set at the desired frequency.
- 4) Position beams at center of hologram. For RR50 this is done by approximation, for PM5 this is done by watching for equal power in both diffracted beams.
- 5) For RR50, adjust transmitter angle so diffracted beam is retro-reflected back to the transmitter.
- 6) For the PM5, the exact angles of the incident and diffracted beams must be measured to calibrate the system. See Fig. 4 for definition of the angles.
  - a) Measure the far field angle between the diffracted beams  $= \alpha$ .
  - b) If the diffracted beams are not symmetric about the surface normal, measure or estimate this angle  $= \gamma$  (only significant when a 50-degree angle cannot be attained).
  - c) Measure the transmitter incident angle  $= \theta$ .
  - d) Calculate the effective fringe spacing,  $\Lambda$ , and the  $h/d$  ratio using

$$\frac{h}{d} = \frac{\cos \gamma}{2 \cos \theta \tan(\alpha / 2)}, \quad \Lambda = \frac{\lambda \cos \gamma}{2 \sin(\alpha / 2)} \quad (34)$$

Nominal values for the PM5 are  $h/d = 8.9$ ,  $\Lambda = 2.8$  microns, RR50  $h/d = 1.46$ ,  $\Lambda = 0.7134$  microns. PM5 values can vary as much as 10% because of limitations in optical access and should therefore be measured for optimum accuracy.

- 7) Input these values into the software program.

## 2.6 RECEIVER DESIGN

### 2.6.1 OPTICAL DESIGN

The receiving optics consist of a collection lens, focusing lens, and a fiber holder with fiber, as shown in Fig. 12. The collection lens collects and collimates the forward scattered light from particles passing through the probe volume. To collimate the scattered light, the lens is located one focal length away from the probe volume. Imaging the probe volume to check fringe contrast and uniformity (which simplified alignment but is only possible when using unscattered beams of the PM5), requires large diameter lenses: ( $f/D < 6$ ). The collection lens is mounted on a translation stage with motorized drivers to track the movement of the probe volume due to changes in beam separation. The collimated light is then passed through a secondary lens which focuses the light onto the fiber in the fiber holder at a distance equal to the focal length of the secondary lens. Because the secondary lens receives collimated light, it need not be mounted on the translation stage. To increase the performance of the system, achromatic lenses (which have small spherical aberrations), were selected. The light focused into the fiber is then guided through the fiber to a photomultiplier tube (PMT) which converts the light signal to an electronic signal for processing.

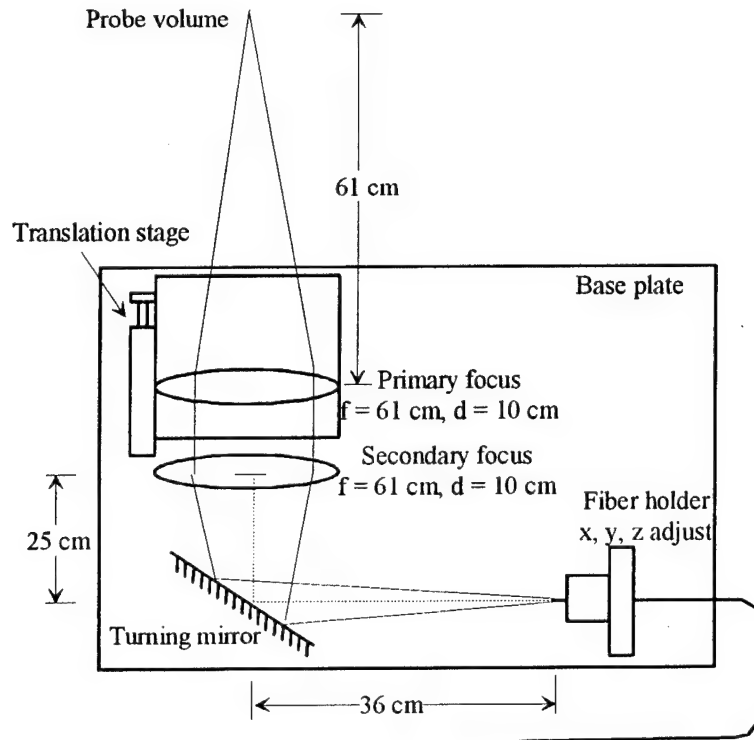


**Fig. 12. Receiver design.** For situations where adequate space is available the turning mirror may not be necessary and all optics can be mounted along a linear rail.

## 2.6.2 FAN FRINGE RECEIVER AND TRANSMITTER

Due to the nature of the fan fringe design, the need for two beams is no longer necessary, ending the need for the beamsplitters and recombiners used for the previous sensors. The reconstruction beam is incident upon the surface of the hologram at  $35^\circ$  from below the horizontal plane, as represented in Fig. 13. This resulted in the fringe pattern projected into the horizontal plane which allowed for an easier alignment of the receiving optics which imaged the probe volume.

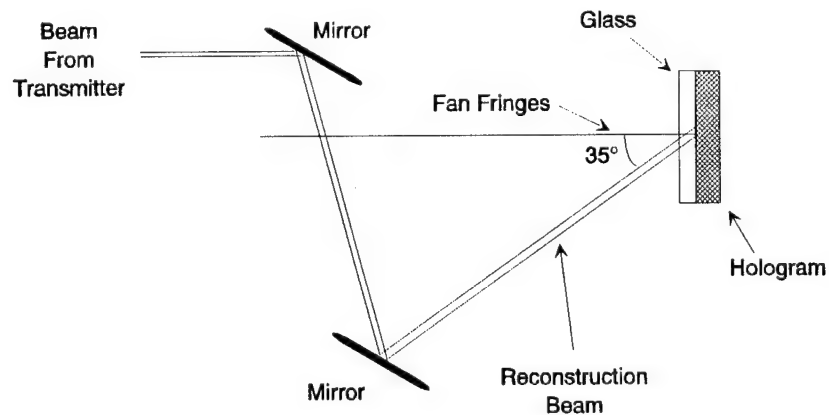


**Fig. 13. Reconstruction beam addressing fan fringe hologram from  $35^\circ$  below normal (side view).**

The transmitter consists of an air cooled, Argon ion laser, two cylindrical lenses to focus the beam, and two mirrors which allow the steering of the beam necessary to obtain the  $35^\circ$  reconstruction angle. The cylindrical lenses focus the reconstruction in the vertical dimension to approximately 100 microns. This is done to increase the intensity of the beams near the surface but has no effect on the focusing of the light in the streamwise or fan direction which is controlled entirely by the hologram. The cylindrical lenses are spaced so that the focus is on the surface of the glass, rather than on the surface of the photoresist, and can be adjusted to compensate for a change in distance from the mirror to the sensor. The use of the mirrors allows extra freedom for the positioning of the transmitter. The transmitter, which is illustrated in Fig. 14, is positioned to be perpendicular to the sensor in the horizontal plane, but not in the vertical plane. To simplify alignment of the receiver, the fan fringe array is kept level in the horizontal plane.

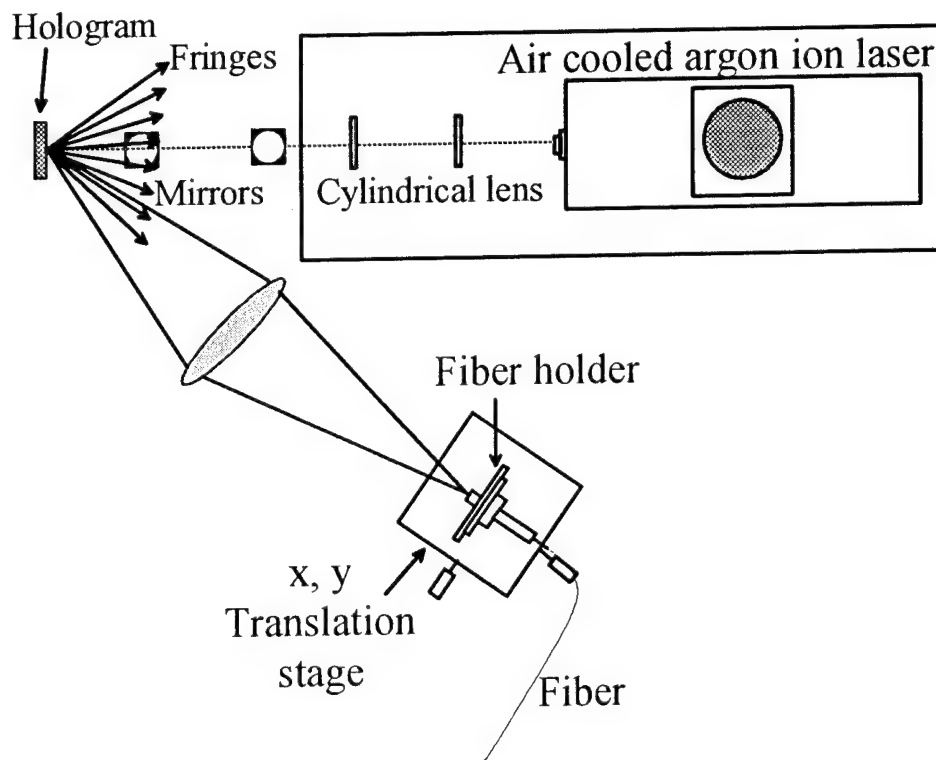


Fig. 14. Setup for the Fan Fringe Sensor with transmitter and receiver.

The actual probe volume is defined by the overlap of the fan fringes and the receiver solid angle. The receiver consists of a single achromatic focusing lens, which focuses the scattered light onto a fiber optic cable. The fiber optic cable is then fixed to an X, Y, Z stage to allow for the overlap region to be adjusted. The receiver is adjusted to minimize the overlap while still detecting a reasonable number of bursts so that the probe volume is kept as close to the surface as possible.

### 2.6.3 ELECTRONICS

The signal processing of the Doppler bursts requires high sensitivity and wide bandwidth ( $>50\text{MHz}$ ). To meet these requirements, a photomultiplier tube and amplifier, (originally designed

for MetroLaser's particle sizing instrument, the PCS-100), was modified and housed in a custom-built box. The PMT features a 10 stage tube (Hamamatsu 1P21) with a sensitivity of  $1.8 \times 10^5$  A/W and a dark current of 2 nA. The transimpedance amplifier has a gain of 750 V/A and a bandwidth of 50 MHz. Active low pass filtering is provided onboard with cutoff frequency selectable through a resistor selection. Total system sensitivity is fixed at 135 V/ $\mu$ W. A  $\pm 15$  V power supply, programmable high voltage supply, ten turn potentiometer and a digital voltmeter were housed with the PMT and amplifier in an aluminum, rack mountable box. Optical access is provided to the PMT via an SMA fiber connector and output is in the form of a coaxial BNC connector. The electrical burst signals are digitized using a DASP100 high speed A to D board from Signatec. Maximum digitizing rate is 0.01  $\mu$ s/point. The DASP100 has an onboard DSP chip that can perform a 256 point FFT in 3.7 ms. The host computer is a 25 MHz 386/SX personal computer. The digitizing rate of the DASP100 limits the PM5 sensor to a maximum flow velocity of 140 m/s. With the use of an 80 MHz AOM, this range can be extended to 364 m/s. The range can be significantly increased by changing to a 500 MHz A to D card; however, FFT processing must be done by the host computer since no DSP chip is available with this card. Maximum measurement range for the PM5 can be extended to 924 m/s and 700 m/s with and without the AOM, respectively.

#### 2.6.4 RECEIVER ALIGNMENT

There is one general procedure for aligning the receiver optics with relationship to each other. The entire receiver assembly can then be aligned to the particular sensor being used.

##### Receiver Optical Alignment:

- 1) Mounting of alignment laser:
  - a) Choose a laser to serve as an alignment tool, typically a HeNe, but it can also be Argon.
  - b) Mount the laser a distance of 10 inches above the optical table.
  - c) Ensure the laser is parallel with the table by measuring the height of the beam at different distances. Adjust the mounting until the beam is parallel to the table.
- 2) Positioning of receiver:
  - a) Position the receiver platform (aluminum plate or optical rail) so that the optical mounting holes are parallel with the beam direction and that the beam travels from the fiber-optic mounting end towards the focusing lenses.
  - b) If using the aluminum plate with a turning mirror, install the mirror and ensure that the mirror alignment is such that the beam is turned at 45 degrees and travels level and parallel to optical mounting holes.
- 3) Installation of primary lens translation stage:
  - a) Install the primary lens translation stage. Ensure that the stage is centered below the beam.



- b) Install a post with a test target in the stage post holder (a white card with crosshairs works well).
  - c) Translate the stage manually (by removing actuator or driving actuator to its minimum position) and check that the beam strikes the target in the same position at all points of travel. Adjust mounting of the stage until proper alignment is achieved.
- 4) Installation of collection lenses:
  - a) Install the primary lens in the mount and ensure that the height is correct by measuring the height of the back reflected beam. The beam should be at the same height as the laser.
  - b) Pivot the lens so the back-reflection falls very nearly back into the laser.
  - c) Repeat procedures a) and b) for the secondary lens.
- 5) Installation of fiber and aperture:
  - a) Install the fiber-optic receiver (without fiber) and the x-y translation stage so that the beam travels through the center of the mount. The distance from the fiber to the lens should be as specified in the drawing (or focal length of lens).
  - b) Install the front aperture and check that it is centered by closing it down to the size of the beam (1 mm) and position it so the beam is transmitted.
  - c) Install the fiber-optic cable.
- 6) Final check-out:
  - a) Launch light into the PMT end of fiber by placing end of fiber in beam. (HeNe or Argon).
  - b) Adjust the angle of fiber optic receiver so that the emerging cone of light is centered on the secondary lens.
  - c) Verify the position of the focus at one focal length in front of the primary lens.
  - d) Translate the stage and verify that the focus changes only in the "on axis" dimension. If the focus moves in the vertical or horizontal dimensions, return to step 3 and repeat with greater precision.
  - e) If the focus is translated only on axis, the receiver is ready for placement.

For the RR50 and Fan fringe sensors, the backlit fiber arrangement should be used for final alignment of the receiver. For the PM5, the direct imaging method should be used as a final alignment procedure.

#### Final Alignment

- 1) Backlit arrangement (PM5, RR50, FAN):
  - a) Swing the receiver into the correct angular position for the sensor being used.
  - b) Drive the receiver stage to fully extended position using software control.

- c) Slide the receiver towards the OSS until the focus is close to the surface.
  - d) For the RR50 and PM5, adjust the angle of the receiver until the surface reflection back reflects to the receiver (receiver is normal to surface). Also make sure the spot overlaps the position of the address beams on the sensor.
  - e) For the FAN sensor, position focus close to the position of the slit images.
  - f) Clamp the receiver to the table.
  - g) Make any fine adjustments to the focus to ensure the focal point is on the surface.
  - h) Define the zero position for "h stage" in software.
- 2) Direct view alignment (PM5 only):
- a) Fully open the receiver aperture.
  - b) Turn on the address beams and position them at  $d = \text{zero}$  (hitting center of sensor).
  - c) Examine the PMT end of the fiber by direct viewing (if coupling is poor) or by placing it in front of a white card.
  - d) Use the fine adjustments on the fiber receiver x,y,z translations to maximize the light transmission through the fiber.
  - e) Lock the stages together using software.
  - f) Drive the stages to the maximum travel in 5mm steps, monitoring the transmission through the fiber. If the transmission drops off completely between both ends of the stage travel, the receiver should be adjusted by small angular displacements so that the light is focused on the fiber along the entire length of travel.
- 3) Final alignment (PM5, RR50):
- a) Connect the fiber to the PMT.
  - b) Connect a scope to output of the PMT (or use for burst with histogram disabled).
  - c) Adjust the x, y stage on the receiver to maximize the scattered or zero order signal.
  - d) Initiate flow and seeding.
  - e) Position probe volume at desired location. Block zero order beams.
  - f) Reduce aperture size and adjust fiber alignment for optimum signal.
- 4) Final alignment for FAN:
- a) Connect the fiber to the PMT.
  - b) Run FANBURST software with histogram disabled.
  - c) Adjust fiber x, y, z positioner for maximum signal.
  - d) Initiate flow and seeding.
  - e) Translate fiber in x direction until burst signals are detected (1-2 mm).
  - f) Translate fiber additional 100 - 200 microns in x direction.

- g) Adjust z axis of fiber to maximize signal.

## 2.7 SOFTWARE DESIGN

In an effort to streamline the data acquisition process and remedy problems with the existing computer programs, custom processing software was written. Two programs were written for processing data: *Dburst* was used for the PM5 and RR50 sensors and *FanBurst* was used for the FAN sensor. A third program, *Control*, was written to control the motion of the two motorized stages.

### 2.7.1 *Dburst.exe*

The software is written in Microsoft Quick C for Windows. It displays the incoming Doppler bursts in both the time and frequency domain at a rate of about 300 milliseconds per burst. While this rate is rather modest, it is more than adequate to be used for alignment of the optical system. The acquisition process is controlled through a parameter screen on the PC. The user sets voltage range, offset level, trigger level, trigger coupling, slope, and sampling rate. These parameters are saved and used for subsequent runs unless they are changed by the user. Offset, trigger level and cutoff frequencies may be changed by the user during acquisition. Fig. 15 is a copy of the parameter screen that the user may modify.

A histogram of the valid bursts can also be displayed on the display screen if desired. To speed processing, the user may select to disable the real-time signal and FFT displays (see Fig. 16 for a sample of the display screen). Because the software no longer has to update the screen as frequently, the data processing time decreases to 100 milliseconds per burst. This data rate is consistent with typical rates measured from the calibration channel. The software can perform an FFT on a user-selectable number of samples occurring after a valid trigger. The user may also select the cutoff frequencies for a bandpass filter. This allows low frequency noise due to large pedestals and high frequency noise due to second harmonic signals to be eliminated. Determination of signal-to-noise ratio is made by comparing the highest FFT value with the average of all the values inside the pass band. Frequency is scanned from low to high so that, in the event of identical values at more than one frequency, the lowest frequency is chosen (this method is somewhat arbitrary). The user defines a signal to noise threshold, below which signals are considered invalid.

The system collects data until a stop value is reached or the user terminates acquisition. Data are stored in a user specified file and indexed by a run number of up to 999. The histogram is displayed graphically on the screen along with a mean and RMS calculation for the distribution (shown in Fig. 17). After each data collection, the run number is automatically incremented. If the user attempts to collect data using a previously saved file name and run number, the program prompts to see if the old data should be overwritten. Otherwise, the old data are redisplayed on the screen.

Date : 10/20/93		PARAMETER SCREEN	
a) Amplifier type : Linear		m) File name : pc5	
b) Voltage range : 20		n) Run number : 1	
c) Offset level : 100		o) Fringe Spacing : 2.8 um	
d) Trigger mode : Continuous		p) Frequency Bias : 0 MHz	
e) Trigger level : 10		q) Signal to Noise : 3 : 1	
f) Trigger source : External		r) Stop mode : Valid Samples	
g) Trigger coupling AC		s) Stop Value : 100	
h) Trigger slope : Positive		t) Histogram : Enabled	
i) Time out value : 1		u) Signal display : Enabled	
j) Sample rate : 6.25 MSPS			
k) Memory size : 16 Kbytes			
l) Run Start Block : 0 K			
y) HighPass Filter : 41 = 0.600 MHz			
z) LowPass Filter : 154 = 1.88 MHz			

Enter parameter number to change, <SPACE> to exit and begin acquisition.....

Fig. 15. Parameters that may be specified using *Dburst* software.

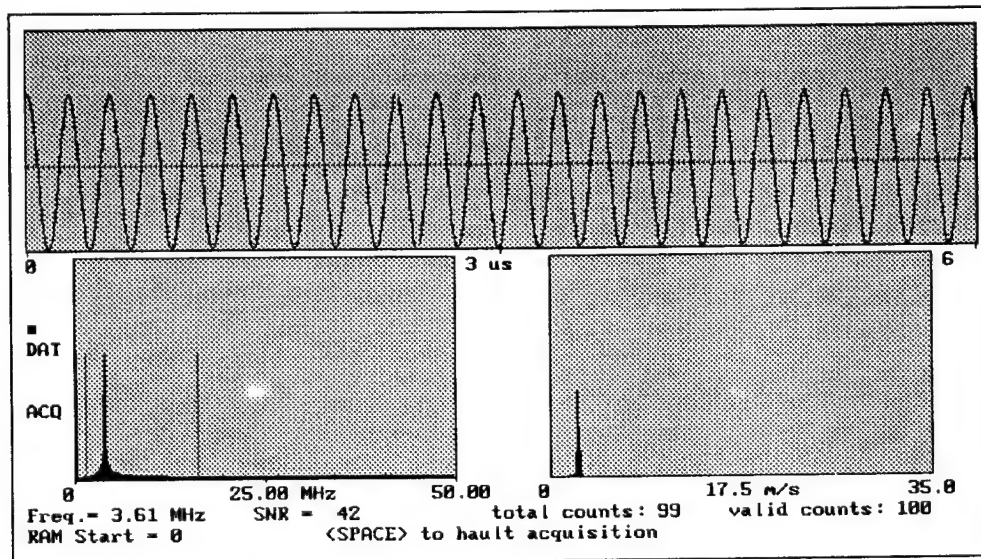


Fig. 16. Dburst data acquisition screen. Top window is time scale, horizontal line indicates trigger level. Lower left window is FFT spectrum, vertical lines indicate bandpass filter cut off points. Lower right window is histogram of valid counts. Frequency and SNR represent peak frequency and signal-to-noise ratio of last valid burst.

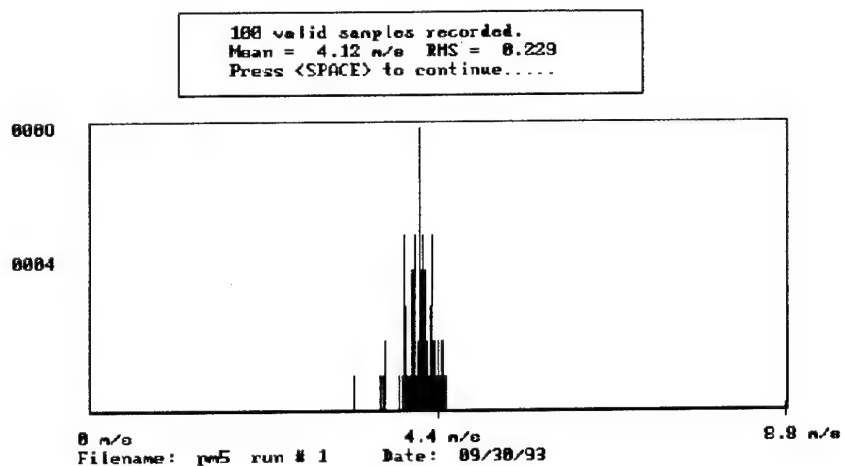


Fig. 17. Histogram and statistics displayed at end of acquisition.

### 2.7.2 FanBurst.exe

Initial measurements of the FAN sensor in the UCI calibration channel using *Dburst* produced frequency distributions that were strongly dependent on the high-pass filter point. Burst discrimination based solely on Fourier transform data was unable to distinguish between pedestal or low frequency noise and valid signals. To remedy this situation, the burst processing software was modified to apply more demanding selection criteria. Because the FAN sensor produces a fixed number of fringes (in this case seven) it is possible to make determinations of burst validity based on the overall burst width and the Fourier spectrum. The time domain burst measurements are shown graphically in Fig. 18 and the algorithm employed to process the bursts is illustrated in Fig. 19.

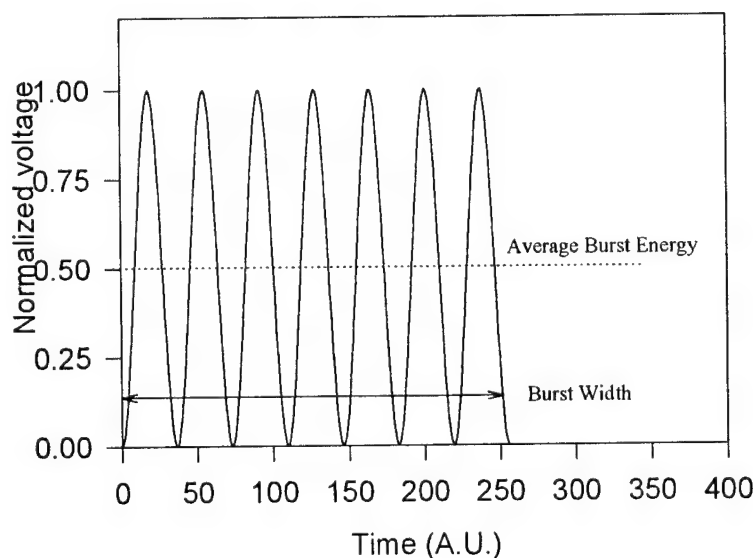


Fig. 18. Time domain burst measurements.

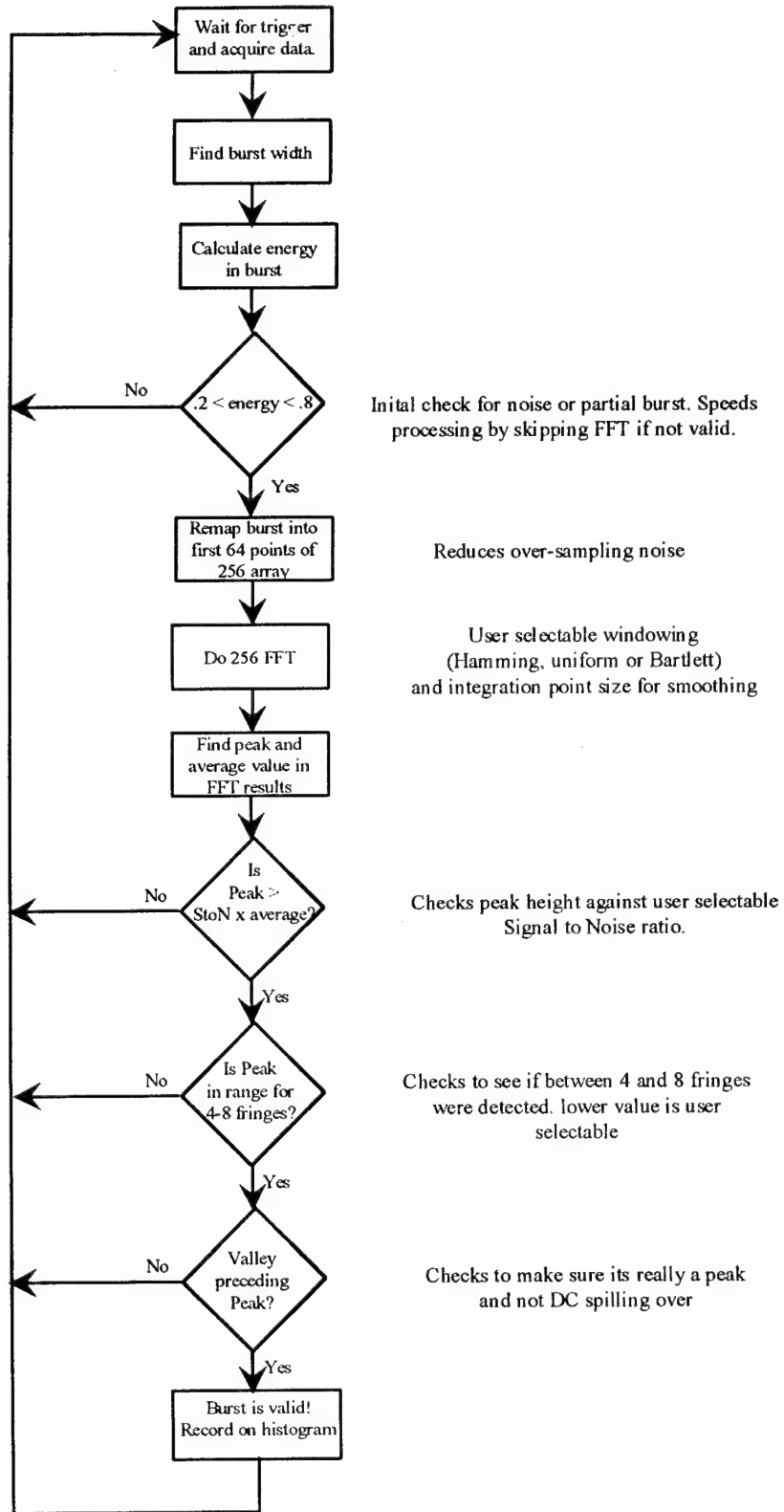


Fig. 19. Computer algorithm used to determine if Doppler burst is valid.

The burst is first analyzed to determine the average burst energy (normalized by the peak value). A perfect sinusoidal burst will give a normalized burst energy of 0.5. A reasonable selection criteria was determined to be greater than 0.2 and less than 0.8. These values are only changeable at the source code level. It was found that a large number of bursts could be discarded using these criteria alone, saving the computation time of doing the FFT. If the energy is within the preset limits, the data are then mapped into 64 data points using an interpolation routine and were placed into a 256 point array. The additional points are zero filled. Because there should be no more than 7 fringes in a valid burst, burst widths wider than 64 data points represent data that was significantly over-sampled. Desampling to 64 points eliminates high frequency noise and makes windowing and subsequent filtering easier. A 64 point window is applied to the data. The user can select between Hamming, Welch and uniform windows. The FFT is performed and the results are smoothed by a user-selectable window (1 - 31 points). The FFT frequency must indicate that there were between 8 and a user-selectable, minimum number of fringes in order to count the signal as a valid burst. Four fringes is the default minimum value. The FFT spectrum is further analyzed to check that a valley occurred before the peak (defined as less than or equal to  $(\text{peakvalue}/(\text{StoN}/3+1))$ ). This was done to guard against leakage from the DC signal.

Because of the dynamic remapping into the 64 point array, each burst is processed identically, regardless of its frequency. High pass and low pass frequency filter points automatically readjust depending on the measured burst width. This permits measurements of frequency over the entire spectrum (from as high as  $(\text{sampling frequency})/2$  to  $(\text{sampling frequency})/256$ ) without clipping. The new algorithm has substantially improved the data processing power of the system.

### 2.7.3 *Control.exe*

To increase the speed of data acquisition and therefore ease of testing, the address beam separation and receiver focusing were automated using computer control. Small electric motors, fitted with position feedback sensors, were purchased from Oriel and used to drive the stages responsible for address beam separation (probe volume height) and primary receiver focusing. These motors are driven with a motion control board purchased from Galil, and housed in a PC. A program was written at MetroLaser in QuickBasic for precise and remote actuation of the stages. The program allows the user to move the position of the stages independently using keyboard keys to toggle the motion. The stages can also be locked together through software control so that the receiver tracks the motion of the transmitter. By specifying a desired position for the probe volume, (as measured from the surface or its current location), both stages are automatically driven to the correct position. They can then be incremented in a preset direction by the press of one key. This software records the stage position to a DOS file so that *DBurst* has access to the information at all times. *Control* runs as a self-contained package but is called as a shelled program during the execution of *DBurst*.

### **3.0 SMART SURFACE FABRICATION**

#### **3.1 HOLOGRAPHIC RECORDINGS**

Holographic recordings were made in positive photoresist coated onto metal and glass substrates. Coatings were done both in-house and by commercial vendors. Holograms were recorded using a 442nm HeCd laser, P= 100 mW (LiCONiX). The developed holograms could be used without any further processing; however, the reflectivity was limited to less than 4%. Aluminizing the plates raised the reflectivity to as high as 90%. The aluminized plates could further be used to grow nickel shims which were high quality replicas of the original holograms. The shims were aluminized and used as sensors. A master shim was used to emboss aluminum coated Mylar to effectively mass produce the Smart Surfaces. The Mylar holograms were then adhered to glass or metal and tested as sensors. This section describes the coating process, the recording/development procedure, the optical recording layouts for each type of sensor and the mounting procedures. It also includes a discussion of investigations into chemical etching of the sensors and preliminary experiments made to record on curved surfaces.

##### **3.1.1 SUBSTRATES AND PHOTORESIST COATING**

The sensors used for testing at UCI and WL were originally recorded on flat glass plates that were coated with photoresist. The coating of curved metal substrates is discussed in Section 3.3. Plates were both purchased from outside vendors and coated in-house. In the development of the PM5 and RR50 sensors, coated plates were purchased from Townlabs Inc. and Shipley 1400 series positive photoresist was used. The resist thickness was nominally 1.5  $\mu\text{m}$  and typically four exposures could be made on each 2.5" x 2.5" plate. Two different types of Townlabs plates were used. The first type of plate had an Iron oxide sublayer which enhanced adhesion of the photoresist to the glass and reduced back reflections. We found, however, that the coating did not entirely eliminate Fresnel reflections from the plate. Because of this, we felt that the iron oxide layer was not worth the extra cost, (about \$2 additional for each \$5 plate) and chose to purchase regular, unbacked plates. The back side of the plate was then coated with ordinary flat black spray paint to reduce back reflections. In addition, the iron oxide coating could not be used for recording of blazed gratings, which is required for the FAN sensor.

We also developed the technology to coat photoresist onto substrates at MetroLaser. Initial attempts at coating surfaces used a spray method. A commercial air gun was purchased and used with compressed nitrogen to spray photoresist onto glass plates. We were eventually able to obtain reasonable quality flat plates with this method; however, even the best plates suffered from aberrations due to the paint drying with a slight amount of surface roughness or "orange peel." The best results were obtained using a two pass method where an initial thin layer was deposited followed by a thicker layer. With continuing development, this method could prove to be satisfactory but it was abandoned in favor of other techniques.

In an effort to obtain high quality, flat glass plates, a pouring or drip coat method was investigated. A large pool of resist is deposited on the substrate using a syringe and the puddle is rolled around until the entire surface is coated. The plate is then turned sideways so the excess



resist can run off. While this method tends to leave nonuniform coating in the top to bottom direction, the surface smoothness was vastly improved over the spray method. Many 4x5" plates were coated using this method with an approximate yield of about 50%. With the exception of particulate matter settling onto the plate and build-up near the edge, the plates coated using this method were of equal quality to those produced by Town Labs.

The final evolution in coating flat plates was to build a spin coating machine using a 3000 RPM motor. The high speed was needed to achieve ultra thin coatings. The motor is mounted in a large 12" dia. x 18" bowl and covered with a Plexiglas cover. Actual rotation speed is controlled using a variable voltage supply. The current procedure for coating the plates is as follows:

The procedure is performed inside a clean box (class 100 or better).

1. Clean plates with bleach and acetone wipe.
2. Use anti-static brush on plates.
3. Place plate on spinner and cover.
4. Measure 2 cc of resist ( or Brewer ARC) onto center of plate through a small hole in the cover.
5. Let resist flow over entire plate.
6. Spin for:
  - ARC - 3 min @ 100 RPM.
  - Photoresist - 1 min @ 1000 RPM.
7. Bake ARC coatings @ 200 °F for 30 seconds.
8. Remove and allow to air dry in dark or safe light environment for at least 10 additional minutes.

This procedure has resulted in high quality coatings; however, some dust does appear to settle onto the plates after the spinning which is due to suboptimal conditions inside our clean box.

Recording holograms on reflective (metal) surfaces poses an additional problem due to the large reflection occurring at the surface. We tested anti-reflection (ARC) material supplied by Brewer Scientific to see if it could eliminate unwanted back-reflections. The ARC liquid may be spun on plates in a similar way as the photoresist and when dry is highly absorptive at the 442 nm wavelength. It also provides a relatively good index match with the photoresist so there are negligible reflections at the boundary. Any light not absorbed by the resist is greatly attenuated by the ARC material, and any transmitted light that is reflected is even further attenuated. The material has the advantage that it may be processed, etched and removed along with the resist, unlike oxide layers. Table 2 summarizes the results of measurements made on various thickness coatings of the ARC material. The slow spin of the XL20 material provided the best performance for us.

**Table 2.**  
Relationship between spin speed and attenuation of anti-reflection material.

ARC type	RPM	TRANSMITTED
XLT	1000	38.7%
XLT	100	12.5%
XL20	2000	61%
XL20	100 ramp 1000	12.5%
XL20	100	0.6%

### 3.1.2 RECORDING PROCEDURES

Initial holographic recording experiments were conducted using a fiber-optic delivery system. Upon construction of a Michelson interferometer to monitor fringe stability, it was discovered that random thermal fluctuations occurred in the fibers, causing phase drift and instability in the fringe pattern. This thermal noise caused significant fluctuations (greater than  $\pi$  phase change), in time scales of roughly several hundred milliseconds. To mitigate this problem, an enclosure was built around the entire optical setup, excluding the laser, out of foam core material (poster board). The enclosure was effective in damping air currents and reduced the phase drift in the fibers to less than 10% of a fringe during a 5 -10 second time period. Although good holograms could be recorded with this setup, the reproducibility was very poor and ultimately this system was abandoned in favor of a freespace delivery system. The foam-core enclosure was used in the free space system to minimize thermal drift due to air currents.

A shutter system was assembled at MetroLaser using a GreyLabs dark room timer and a 12-volt relay. The timer was modified internally to drive the relay and the relay armature fitted with a long lever arm and brass flag to block the beam. The system, costing a mere \$120, has an accuracy of 0.1 second and provides an economical alternative to the \$900 Newport shutter. The shutter actuator, consisting of the relay and flag, was mounted on a tripod external to the table to provide isolation from vibrations occurring during its opening. Additionally, the shutter controller was moved outside the room to allow personnel to leave the room and control exposures remotely, resulting in added stability.

High quality holographic recordings required high quality, beam intensity uniformity. Using short focal length lenses for collimation (5-10 cm) results in a collimated beam; however, the intensity profile is Gaussian, resulting in a nonuniform exposure. A characteristic of such an exposure is a bowl-shaped resist profile superimposed on the fringes. This typically results in a reconstructed beam having a ring or central dot of high intensity while the rest of the reconstruction is dim. To alleviate this problem, longer focal length lenses must be used, resulting in an overfilling of the lens aperture ( $D = 1''$ ) and a more uniform intensity distribution.

The procedure used to expose and develop the plates is:

1. Beams and optics are aligned, and then the laser output is blocked with the shutter.
2. Room lights off, and the yellow 10W safe light on.
3. Plate positioned in holder, and the enclosure shut.
4. Settling time of 1-3 minutes allowed. (Personnel leave room).
5. Shutter opened for the correct time - Exposure range between 5 - 25 mJ/cm<sup>2</sup>.
6. Plate repositioned for the next shot. Typically four shots per plate.
7. Additional settling time of 1-3 min. between each exposure.
8. Plate removed after all the exposures are done and placed in a light tight box.
9. Solution prepared in darkroom using Shipley 1420 developer.  
4:1 - Distilled water: developer.
10. Vigorous agitation in solution for 4 seconds.
11. Immediate immersion of the plate in flowing water bath for 2 minutes.
12. Dried the plate using compressed nitrogen gas.

This procedure has been used for a variety of exposure energies and beam geometries. Early attempts at exposures using longer development times (10 seconds in solution) resulted in streaked or smeared lines running through the hologram. This was felt to be the result of over development and reduction of the developing time alleviated this problem.

Unwanted "star burst" patterns were also visible on the surface as well as in the reconstructed beam in many of the holograms. This effect was found to be caused from surface reflections from the collimating lenses. Replacement of the optics using high grade, anti-reflection-coated lenses reduced this problem.

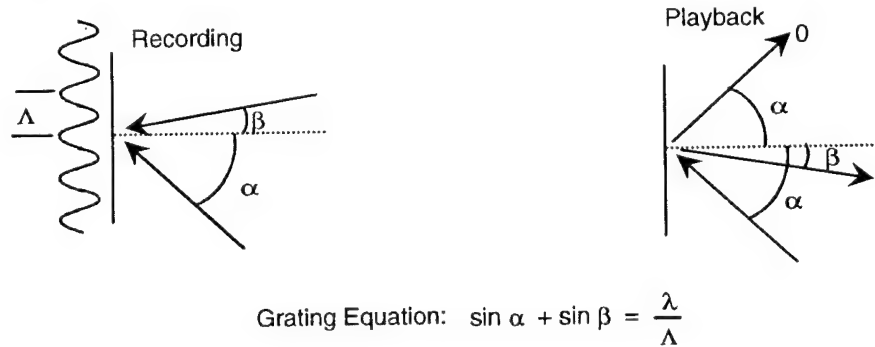
### 3.1.3 PM5 LAYOUT

A decision was made to change the playback wavelength to 488 nm (Argon ion) from the originally proposed wavelength of 442 nm (HeCd). Switching to a different playback laser allowed parallel recording and testing of the smart surfaces. The choice of 488 nm over 442 nm was mainly driven by the availability of low cost, high power, air cooled argon ion lasers in comparison to the higher cost, high noise, HeCd laser. Being a more common laser, the argon ion wavelength also offers more compatibility with existing lasers at WPAFB and other facilities. A 100 mW, single 488nm line, air cooled, argon laser was purchased as the reconstruction laser.

The HeCd laser was necessary for recording because the photoresist was insensitive at 488 nm. Because the recording and playback wavelengths are different, the recording geometry must be arranged so that the reconstructed image has the desired characteristics for each sensor. The recording and playback of a simple hologram can be described by the grating equation,<sup>5</sup>

$$\sin \alpha + \sin \beta = \frac{\lambda}{\Lambda} , \quad (35)$$

where  $\alpha$  and  $\beta$  are the angles of the reference and object beams with respect to the surface normal,  $\lambda$  is the freespace wavelength and  $\Lambda$  is the period of the holographic grating. During recording, the reference and object beams are incident on the holographic medium as shown in Fig. 20. Equation 35 can be used to determine the resulting holographic grating period. During playback, the hologram is illuminated with a single reference beam. Equation 35 can be used to determine the angle of the diffracted object beam as a function of incident angle and wavelength. Fig. 20 shows the design example for the PM5 sensor. Equation 35 is valid for simple holographic diffraction gratings illuminated by collimated beams but is not valid when the hologram contains complex information such as focusing. In general, chromatic corrections cannot be made for complex holograms by simply changing the reference beam angle. First order corrections can be made using Equation 5; however, chromatic aberrations will exist. Because the PM5 and RR50 series holograms were designed specifically to work with collimated beams, Equation 5 is valid for calculating the corrections necessary during recording.



Want Playback @488 nm,  $\alpha = 50$ ,  $\beta = \pm 5$

Need:  $\Lambda = 0.572 \mu\text{m}$ ,  $\Lambda = 0.718 \mu\text{m}$

With  $\beta = \pm 5$  and  $\lambda = 442 \text{ nm}$

$\alpha = 43.3, 44.6$

Choose  $\alpha = 44.0$ ,  $\beta = \pm 5$  for recording  $\longrightarrow \Lambda = 0.565 \mu\text{m}, 0.728 \mu\text{m}$ .

Playback angles:  $\lambda = 488\text{nm}$ ,  $\alpha = 50$ :  $\beta = 5.6, -5.5$

**Fig. 20. Playback wavelength compensation for PM5.**

The optical layout necessary for recording the PM5 sensor is shown in Fig. 21. The HeCd laser is split into two legs, reference and object. Both legs are spatially filtered and collimated. The reference leg is incident at 44 degrees to the surface normal. The object leg is further broken into two components by a second beamsplitter and the resulting two legs are incident at plus and minus 5 degrees. In terms of exposure, two parameters are important in the recording of the PM5 sensor. First, it is desirable to have the overall diffraction efficiency as high as possible. Second, and perhaps more important, the diffraction efficiency of the two beams should be roughly equal

so that the resulting fringe contrast in the probe volume is high. Table 3 shows the recording schedule and the resulting diffraction efficiencies and beam ratios. The 'Ref. to Obj Ratio' refers to the ratio of reference beam intensity to object beam intensity at the plate. To calculate this number correctly, the power in the beam must be divided by the cross-sectional area of the beam intersection with the plate. Notice that the best sensor is not the one with the highest diffraction efficiency but rather the one with the replay beam ratio closest to unity (i.e. recording #4).

**Table 3.**  
**Recording schedule for 8"X10" Holographic plate and diffraction efficiency for embossed Mylar holograms - PM5 sensor. Recorded 28 Mar 93**

Recording number	SERIES	Total Power	Exp. Time	Exp. Energy	Ref to obj. Beam Ratio	Diff. Eff. Mylar	Replay Beam ratio
5	PM5	2.11mW	3.3 sec	9.0 mJ/cm <sup>2</sup>	2.5:1 (5:1)*	28%	.77
4	PM5	2.11mW	3.7 sec	10.0 mJ/cm <sup>2</sup>	2.5:1 (5:1)*	32%	1.0
3	PM5	2.11mW	3.9 sec	10.5 mJ/cm <sup>2</sup>	2.5:1 (5:1)*	33%	1.4
2	PM5	2.11mW	4.1 sec	11.0 mJ/cm <sup>2</sup>	2.5:1 (5:1)*	40%	3.2
1	PM5	2.11mW	4.5 sec	12.0 mJ/cm <sup>2</sup>	2.5:1 (5:1)*	33%	2.8

(\*) Before angular correction factor.

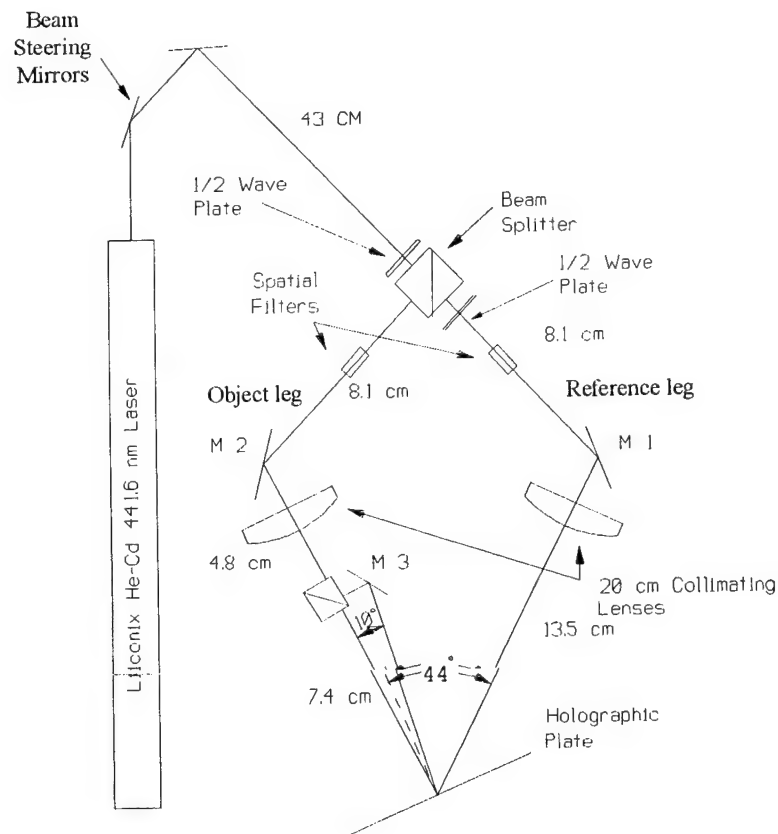


**Fig. 21. Recording layout for PM5 sensor.**

### 3.1.4 RR50 LAYOUT

The optical recording layout for the RR50 sensor is shown in Fig. 22. The angular corrections necessary to compensate for the differences in recording and playback are also shown in Fig. 22 and were calculated using Equation 35. Of particular importance to this sensor is achieving as close to the 50% diffraction efficiency mark as possible. This was accomplished by bracketing the exposure energies until the desired results were achieved. The diffraction efficiency was a function of the exposure fluence, resist type, resist freshness, developer concentration, developer freshness and development time. Because of this, results could vary significantly from day to day. Table 4 includes the exposure log summary and measured diffraction efficiency for RR sensors on the 8" x 10" holographic plate that was recorded for the embossing process. The exposures were bracketed around the expected values for optimum diffraction efficiency to ensure that one or several of the designs would be close to the desired value. In addition, the decrease in diffraction efficiency experienced when transferring the hologram to the Mylar during the embossing process was compensated for by recording holograms having nominal diffraction efficiency much higher than 50% (RR100).

	Record	Playback
Wavelength ( $\mu\text{m}$ )	0.442	0.488
Reference angle (deg)	18	20
Object angle (deg)	18	-----
Grating spacing	0.72 $\mu\text{m}$	0.72 $\mu\text{m}$
1st order angle	-----	19.9

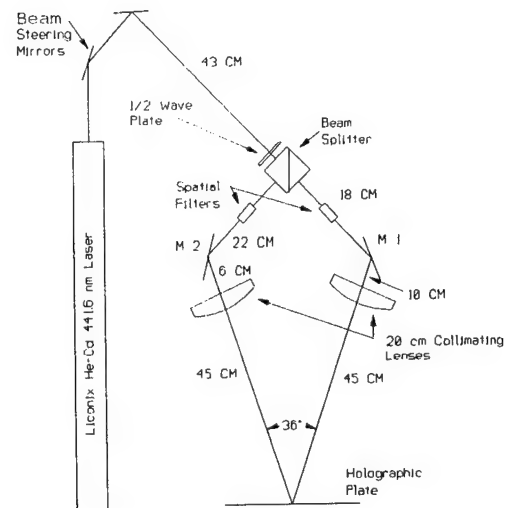


Fig. 22. Optical layout for recording RR series holograms and angular corrections for wavelength changes between recording and playback.

**Table 4.**  
**Recording schedule for 8"x10" Holographic plate and diffraction efficiency for embossed Mylar and nickel shim holograms - RR series. Recorded 25 Mar 93.**

Recording Number	SERIES	POWER TOTAL	EXPOSURE TIME	EXPOSURE ENERGY	BEAM RATIO $P_R:P_O$	Diff. Eff. Mylar	Diff. Eff. Shim*
1	100 RR	3.06mW	1.8 sec	7.0 mJ/cm <sup>2</sup>	2:1	39%	58.5%
2	100 RR	3.06mW	1.9 sec	7.5 mJ/cm <sup>2</sup>	2:1	36%	54%
3	100 RR	3.06mW	2.1 sec	8.0 mJ/cm <sup>2</sup>	2:1	37%	55%
4	100 RR	2.93mW	2.2 sec	8.5 mJ/cm <sup>2</sup>	2:1	50%	75%
5	100 RR	2.93mW	2.3 sec	9.0 mJ/cm <sup>2</sup>	2:1	59%	88.5%
6	50 RR	2.93mW	1.6 sec	6.0 mJ/cm <sup>2</sup>	2:1	49%	73%
7	50 RR	2.93mW	1.5 sec	5.5 mJ/cm <sup>2</sup>	2:1	44%	66%
8	50RR	2.95mW	1.3 sec	5.0 mJ/cm <sup>2</sup>	2:1	35%	52.5%
9	50 RR	2.95mW	1.2 sec	4.5 mJ/cm <sup>2</sup>	2:1	30%	45%
10	50 RR	2.95mW	1.1 sec	4.0 mJ/cm <sup>2</sup>	2:1	24%	36%

\* Shim with aluminum coating for enhanced reflectivity.

### 3.1.5 FAN FRINGE LAYOUT

The basic design theory of the FAN sensor is to record the image of two slits appearing exactly at the surface of the substrate. An analysis considering the effects of slit misalignment was conducted to estimate the tolerances necessary during recording. Essential to the design of the sensor is that the fringe spacing approaches zero at the wall. This ensures that a constant Doppler frequency is produced, regardless of position. Misalignment of the focal point of the slit, either in front or behind the surface, will cause the point where fringes converge to also move in front or behind the surface. This will introduce a position dependent term into the Doppler frequency. By allowing the fringe spacing to have a misalignment offset,  $\delta$ , we can make the following substitution for fringe spacing as a function of distance normal to the surface:

$$\Lambda = \frac{d\Lambda}{dy} y + \delta. \quad (36)$$

Equation 36 can be used to calculate the deviation of Doppler frequency from a constant value as a function of height off the surface and the misalignment offset. Results of this numerical calculation are shown in Fig. 23.

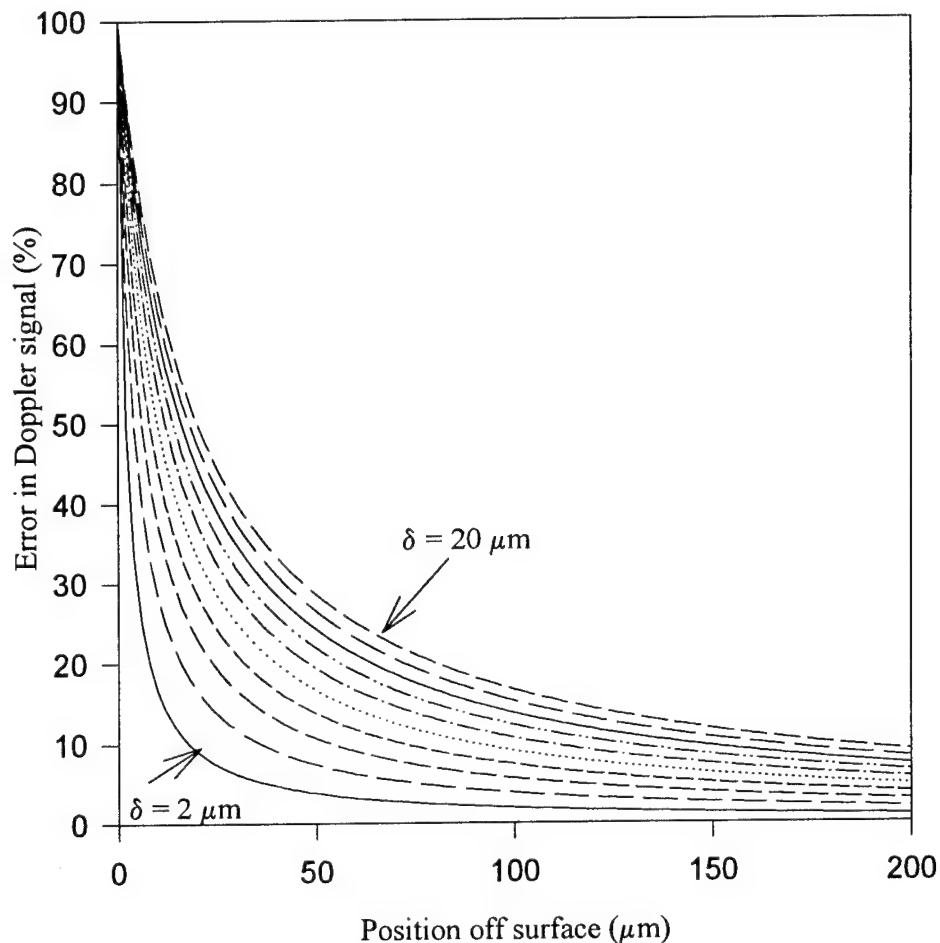


**Fig. 23.** Percent change in Doppler frequency (from constant value) as a function of position above surface for increasing misalignment of slit focal points.

As a result of these calculations, it was determined that it was necessary to align the focal point of the slits to within 5 microns of the surface. Additionally, the effects of playback with a different laser wavelength were investigated. Computer calculations showed that when the recording geometry is such that the reference beam and the fan fringes are in the same plane playback with a different wavelength results in severe chromatic aberrations. With an in-plane geometry (equivalent to an off-axis image) the reconstructed slits would increase in size from 5 to 10 times when recorded with 442 nm and played back at 488 nm. To mitigate the chromatic aberrations of the system, the reference beam angle was moved so that its plane of incidence was perpendicular to the fan direction. This results in an on-axis focusing arrangement during playback which greatly reduces chromatic aberrations and allows near diffraction limited beams to be reproduced. Fig. 24 shows the recording arrangement.



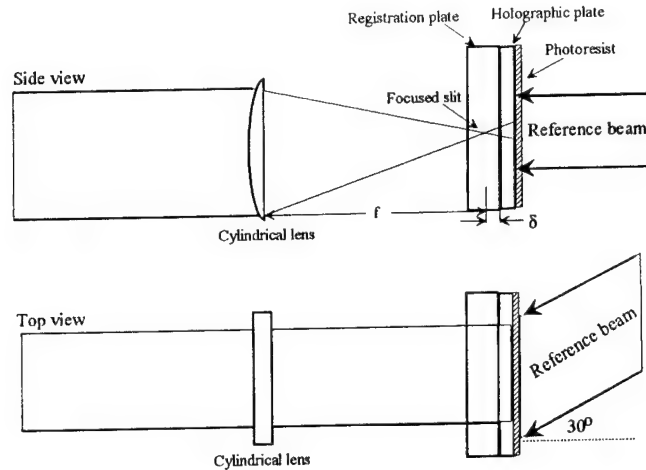


**Fig. 24. Recording of the velocity gradient sensor. Reference beam is incident from behind the plate and forms a 30 degree angle with the nonfocusing axis of the object beam.**

For our experiments, an apertured cylindrical lens was used to form a single slit. By controlling the aperture, the slit size and quality could be controlled. A 4-mm aperture was used, resulting in a 2-micron slit width. Wider apertures resulted in unacceptable beam aberrations. Due to physical limitations caused by the short focal length cylindrical lens, the reference beam was incident from the backside of the plate. This recording geometry results in a blazed grating in the photoresist which can increase diffraction efficiency significantly over conventional sinusoidal gratings.<sup>6</sup> Because the object beam was focusing, it was necessary to bias the energy in the two beams 10:1 in favor of the reference beam so that intensities at the photoresist were roughly equal.

The holographic plate was mounted on a registration plate using an index matching fluid. The registration plate was attached to a precision translation stage so that its position relative to the focal spot could be adjusted. A microscope objective was used to view the focus of the laser beam and white light scattering off imperfections at the surface of the registration plate. By bringing both into focus at the same time, the position of the focus could be located precisely at the face of the registration plate. To record a hologram without chromatic corrections, (i.e. playback and recording wavelengths the same), the object beam is focused at the back surface of the registration plate. To generate the image of two slits from one hologram, two exposures were made with the registration plate displaced vertically between each. The two slits were recorded 20 microns apart with a resolution limited by the stage of approximately 2.5 microns.

Because longer wavelength light will diffract at a larger angle, holograms recorded at 442 nm will focus at a shorter distance when played back at 488 nm. To compensate for this focal length shorting, it is necessary to record the hologram with the slit focused slightly in front of the glass (shown as  $\delta$  in Fig. 24). Calculations of the correction distance depend on the substrate thickness, index of refraction and reference beam angle. A program to calculate the correction distance was written using Mathcad and is shown in Fig. 25. A nominal correction of 220 microns was calculated using this program. This value was used initially and adjusted slightly after testing the playback of actual sensors to achieve registration to within 5 microns.

On axis calculation for chromatic aberration. Assumes recording is focused in front of glass surface by distance delta. Corrected for refraction at front surface 1-6-94.

$$\begin{aligned}
 \lambda_{\text{rec}} &:= 442 && \text{recording wavelength (nm)} && w_0 &:= 2 && \text{waist of recording beam} \\
 \lambda_{\text{play}} &:= 488 && \text{playback wavelength (nm)} && \delta &:= 220 && \text{distance of probe volume off} \\
 &&& && &&& \text{the surface (um).} \\
 L_{\text{glass}} &:= \frac{25.4}{8} && \text{Glass thickness (mm)} && \theta &:= 0 && \text{crossing angle degrees} \\
 &&& && n &:= 1.517 && \text{index of refraction of glass} \\
 &&& && &&& \text{range in mm around glass surface to examine} \\
 L_{\text{range}} \text{ min} &:= .1 && L_{\text{range}} \text{ max} &:= .1 \\
 y_{\text{step}} &:= 30 && \text{number of iterations over HOE radius} && \lambda_{\text{rec}} &:= \frac{\lambda_{\text{rec}}}{n} \\
 L_{\text{step}} &:= 100 && \text{number of steps inside Lrange} && \lambda_{\text{play}} &:= \frac{\lambda_{\text{play}}}{n} \\
 \alpha_{\text{max}} &:= \left( \frac{\lambda_{\text{rec}} \cdot 2}{\pi \cdot w_0 \cdot 1000} \right) && \text{maximum radius of HOE} \\
 L_{\text{max}} &:= L_{\text{glass}} + \frac{\delta \cdot n}{1000} && \text{Distance of focus to film} \\
 i &:= 0..y_{\text{step}} && \text{index for ray number} \\
 j &:= 0..L_{\text{step}} && \text{index for position number} \\
 \alpha_{\text{rec}_i} &:= \left( i - \frac{y_{\text{step}}}{2} \right) \cdot \frac{\alpha_{\text{max}}}{y_{\text{step}}} \cdot 2 && \text{angle of each recording ray} \\
 y_i &:= L_{\text{max}} \cdot \tan \left( \theta \cdot \frac{\pi}{180} + \alpha_{\text{rec}_i} \right) && \text{position on film of each recording ray} \\
 f_i &:= \left( \frac{\sin \left( \theta \cdot \frac{\pi}{180} + \alpha_{\text{rec}_i} \right)}{\lambda_{\text{rec}}} \right) && \text{spatial frequency caused by each ray} \\
 L_j &:= \frac{(L_{\text{range}} \text{ max} + L_{\text{range}} \text{ min}) \cdot j}{L_{\text{step}}} + L_{\text{glass}} - L_{\text{range}} \text{ min} && \text{position along axis} \\
 &&& L_{100} = 3.275 \\
 \alpha_{\text{play}_i} &:= \text{asin} \left( \lambda_{\text{play}} \cdot f_i \right) && \text{angle of each play back ray} \\
 \text{Ray}_{(i,j)} &:= (y_i) - (L_j) \cdot \tan(\alpha_{\text{play}_i}) && \text{height off axis of each ray, i, as a function of distance, j.} \\
 \text{Minray}_{j,1} &:= \left[ \left( \max(\text{Ray}_{<j>}) \right) - \left( \min(\text{Ray}_{<j>}) \right) \right] && \text{find extreme rays at each point} \\
 \text{Minray}_{j,0} &:= j && \text{create linear number array for sorting} \\
 DL_j &:= (L_{\text{glass}} - L_j) \cdot 1 && \text{convert to distance from glass surface} \\
 \text{Minray} &:= \text{csort}(\text{Minray}, 1) && \text{sort according to spot size} \\
 \text{Waist} &:= |\text{Minray}_{0,1}| \cdot 1000 && \text{pick minimum spot size} \\
 \text{loc} &:= |\text{Minray}_{0,0}| && \text{find longitudinal position of that spot} \\
 \text{height} &:= \left| \left| \text{Ray} \left( \frac{y_{\text{step}}}{2} \right), \text{loc} \right| \right| && \text{find height of the spot} \\
 \text{HOE}_{\text{spot}} &:= y_{\text{step}} - y_0 + \frac{w_0}{1000} && \text{calculate size of hologram} \\
 G_{\text{waist}} &:= \frac{L_{\text{loc}}}{\text{HOE}_{\text{spot}}} \cdot \frac{\lambda_{\text{play}}}{1000} \cdot \frac{4}{\pi} && \text{calculate diffraction limited spot size} \\
 z &:= (L_{\text{loc}} - L_{\text{glass}}) \cdot 1000 && \text{conversion for distance to mm} \\
 \text{Ray2}_{i,j} &:= (-\text{Ray}_{i,j}) && \text{second beam is mirror of first} \\
 \text{HOE}_{\text{size}} &:= 2 \cdot \left( L_{\text{max}} \cdot \tan \left( \theta \cdot \frac{\pi}{180} \right) + \frac{\text{HOE}_{\text{spot}}}{2} \right) \\
 z &:= \text{if} \left( z > 0, \frac{z}{n}, z \right)
 \end{aligned}$$

**Fig. 25.** Mathcad program to calculate correction distance needed during recording of the FAN fringe hologram to compensate for a different playback wavelength.

Sensors with and without chromatic corrections have been successfully recorded. The holograms were then coated with aluminum to increase diffraction efficiency by increasing the reflectivity. The coating increased the reflectivity from 4% to about 90%. The overall diffraction efficiency, defined as the fraction of light present in the diffracted fan fringes divided by the light incident on the hologram, was approximately 28%. The physical size of the hologram was approximately 0.5 mm so the use of reconstruction beams larger than this dimension will result in lower overall diffraction efficiencies because of the overfilling. The sensors were also anti-reflection coated on the front surface to minimize unwanted reflections off this surface. Upon receipt of the coated holograms, an additional glass substrate was epoxied to the surface of the exposed photoresist. The glass served to protect the fragile photoresist surface during handling of the sensor. A photograph of the playback of an uncoated sensor is shown in Fig. 26. Visualization of the beams was done by moving a card in the beam path with the shutter open.

The waist of the focused slits was measured to be 1.8 microns and the separation between slits was measured to be 10.7 microns. The sensor is designed to work with 488 nm light, which gives a calibration constant of  $\lambda/S = 0.04530 \pm 0.0017$ . This value is used to convert from Doppler frequency to velocity gradient (see Equation 32).

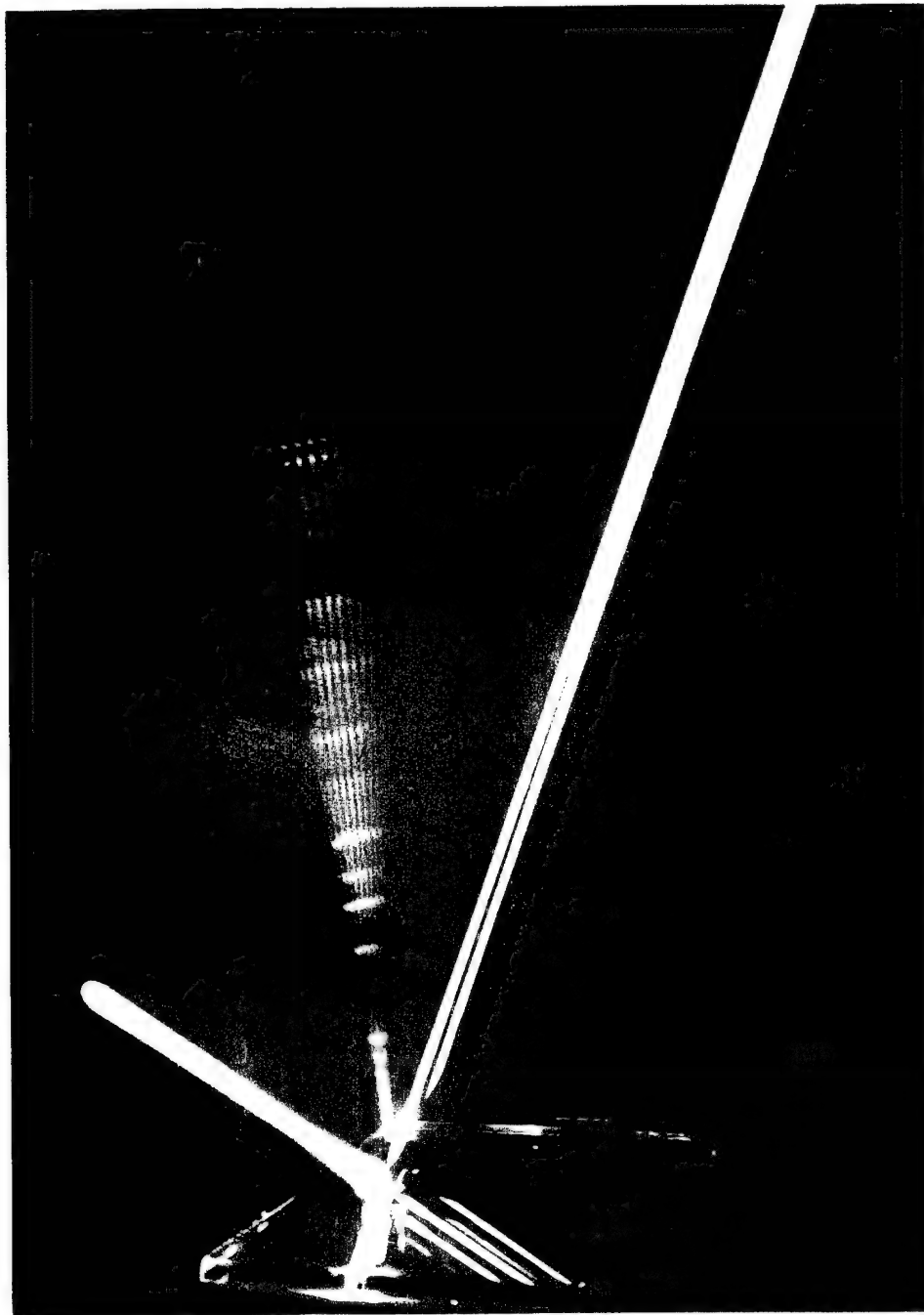


**Fig. 26.** Photograph of fan-fringe sensor played back with 442 nm light. Beams were visualized by sweeping a phosphorescent card (which makes the beams appear green) through the beam path while camera shutter was open.

A second arrangement was proposed for recording the FAN sensor. Chromatic aberrations occurring because of different recording and playback wavelengths resulted in a minimum operational height for the FAN sensor ( $y > 120$  microns). The use of a cylindrical lens to form the slits resulted in beam waist sizes larger than desired and therefore small far field diffraction angles. This increased the size of the nonoverlapping zone near the surface. The only way to overcome these limitations is to record the sensor using a precision mask to form the slits. Additionally, it is necessary to use the same wavelength to record and playback the hologram to avoid any chromatic aberrations.

As an outcome of the channel testing, a new idea was developed for the FAN sensor that would allow easier alignment. It should be possible to record a projection of the receiver's field of view at a spot adjacent to the FAN hologram. By illuminating this region with the address beam, a diffracted order will appear that exactly duplicates the receiver's solid angle. By imaging this light with the receiving lens into the fiber, the receiver will automatically be adjusted to the correct height above the surface. The address beam is then translated over several millimeters to reconstruct the FAN hologram and the alignment is complete. We are incorporating this design into the precision mask so that this concept can be tested in the final version of the FAN sensor. Fig. 27 illustrates the mask design and recording geometry.

We had a precision mask made to the specifications shown in Fig. 27 (Photosciences Inc.). In the final weeks of the Phase II program we attempted to record FAN sensors using this configuration. For these recordings we used a recently developed photoresist that is sensitive in the blue-green area of the spectrum (HSM). This allowed us to record and playback the sensor with the 488-nm argon line. We were successful in recording on the new photoresist; however, several problems prevented us from recording holograms better than the original FAN sensors. The mask was made using a material with an optical density (OD) of 2.0. This turned out to be inadequate because a significant portion of the light was still transmitted relative to the percentage of light transmitted through the 1-micron slits. This caused distortions in the fringe pattern. Also there was a significant amount of light transmitted through the 30-micron slit even though the beam waist was less than 15 microns. This also caused distortions. Finally, the thickness of the glass substrates was thinner than specified, 1/16" instead of 1/8" or 1/4", resulting in a very small spot size on the resist. For future applications it is recommended that the mask be made without the 30 micron slit, and with an OD greater than 4.0.

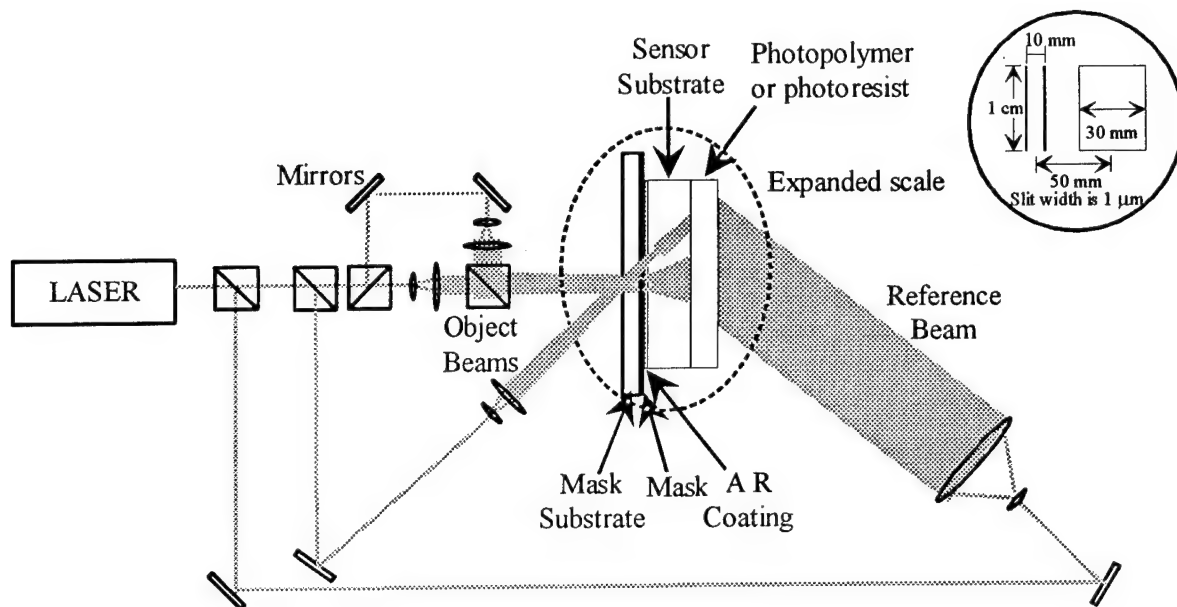


Fig. 27. Recording geometry and mask design for self-aligning FAN sensor.

### 3.2 SMART SURFACE INSTALLATION

For testing at the University of California, Irvine (UCI) and Wright Laboratory (WL), the smart surfaces must be applied on the end of a 1.5-inch-diameter test plug. The plug fits into either the calibration channel or the flat plate inside the wind tunnel. There were three methods used to generate the surface hologram on the plug, each having its relative merits: embossed holograms in Mylar, nickel shims produced from electro-plating and direct application of photoresist coated glass substrates. The Mylar holograms and glass substrates were tested extensively in the UCI calibration channel while the shims and glass substrates were used for the testing at WL Trisonic Gasdynamics Facility (TGF).

#### 3.2.1 EMBOSSED HOLOGRAMS

The most interesting method for applying Smart Surfaces is to fabricate embossed holographic stickers that can be glued to the surface. The stickers are produced by growing metal shims from holograms that are originally recorded on photoresist covered glass plates. The shims are grown by evaporating silver on top of the hologram and then electroplating a thick layer of nickel. The nickel layer is then removed from the glass plate and the resulting shim used to stamp aluminum coated Mylar sheets in a replication process that can produce thousands of copies. An adhesive backing is added to the sheet so that the holograms can then be applied to the test surface in a "peel-and-stick" fashion. These smart surface stickers offer the most exciting alternative to the coating problem since they allow the holograms to be applied to almost any portion of the model surface with a minimum of surface preparation. Additionally, the stickers can be mass produced for very little cost.

We recorded an 8" x 10" holographic plate and sent it to CFC Applied Holographics for shim production and embossing. The 8"x10" holographic plate is the standard size used by CFC. Nonstandard plate sizes can be accommodated by building a special jig; however, it was more cost effective to record onto the larger plate. We received two rolls of embossed Mylar film: one without a backing and the other with an adhesive applied to the back side and covered with a removable liner. Preliminary tests indicated that it was very important to have the aluminized side of the Mylar as the front surface. If the aluminized surface was used on the back, reflections from the front surface would interfere with those from the back and cause interference fringe across the entire image. Having the aluminized side face forward leaves the coating unprotected so care must be taken to avoid scratching the surface.

Fig. 28 shows the correct orientation of the addressing beams with respect to the adhesive backed, Mylar film. Although shown readable in the figure, the MetroLaser logos actually appear as mirror images on the adhesive backed film (reversed from left to right). The RR series are bi-directional, that is, they can be addressed in either direction but the PM series can only be addressed in one direction in order for the diffracted beams to cross. Because the holograms have a blaze to them, the diffraction efficiency depends on the direction of playback. The diffracted power from each side of the PM5 hologram is listed in the form of an average value and as a ratio in Table 3. A ratio of 1 corresponds to equal power in each beam and results in maximum fringe contrast. The best recordings of the PM5 are sensors 3 and 4, which were the ones used for testing in the channel. The diffraction efficiency of the RR series holograms is listed in Table 4. The decrease in efficiency due to the embossing processes can be seen by the fact that the maximum diffraction efficiency of the 100 series is only 60% compared with over 90% for the master. The nickel shims have efficiencies greater than 80%.

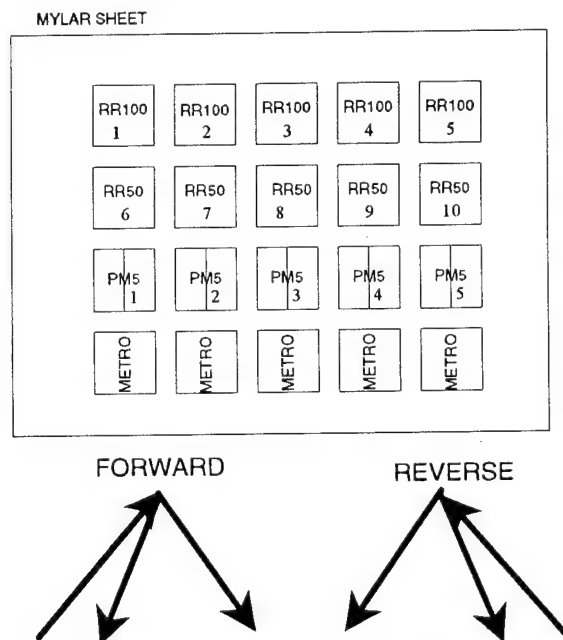


Fig. 28. Orientation for playback of embossed holograms. RR series holograms can be played in reverse but diffraction efficiency is substantially less. Diffraction efficiencies for each hologram are shown in Table 3 for the PM5 and Table 4 for the RR series.

The limiting factor in using embossed holograms is the surface smoothness that can be obtained when applying the hologram to a substrate. The smoothness is effected by 1) the model surface itself, 2) the smoothness/flatness of the Mylar layer and 3) the uniformity of the adhesive.

Applying peel and stick holograms directly to smooth surfaces will result in flatness that is acceptable to the eye but interrogation with a laser beam reveals that surface distortions or irregularities are present. By illuminating the hologram with a collimated beam of several millimeters in diameter and checking the diffracted beam at several distances, one finds that near the surface the beam intensity looks uniform but at distances as short as several centimeters aberrations and nonuniformities in the beam intensity arise. Closer inspection of the holograms reveal that there are small pits and bumps on the surface. We tried several methods to adhere the holograms to the surface to mitigate this problem.

Perhaps the most formidable challenge was to find an adhesive that would bond Mylar to glass or aluminum. Super glues (cyano-acid), epoxies, pressure sensitive adhesives and cements were all ineffective in bonding to Mylar, although they all bond to glass. Super glues and epoxies would hold the Mylar in place but the film could be easily peeled off the substrate, a condition unacceptable for wind tunnel applications. The pressure sensitive adhesive (supplied by Monsanto) was somewhat effective in sticking to the Mylar but it was so viscous that it could not be spread in a thin layer. Furthermore, it did not dry hard and could be easily dented or deformed.

The best solution was found to be a combination of the peel and stick adhesive (supplied on the adhesive backed roll) and 5-minute epoxy. The epoxy forms a thin layer between the adhesive and the substrate, filling in any holes or gaps. In order to produce an optically flat surface, it was necessary to hold the Mylar down on a piece of glass using a vacuum chuck. The chuck was constructed using a 1/2" thick piece of Plexiglas. A square hole was routed out of the Plexiglas, and a slightly smaller piece of optical glass was inserted into the opening. A vacuum line was connected to the groove between the glass and Plexiglas. With the vacuum on, the Mylar film is laid face down on the jig, and once a seal is formed, all air is evacuated between the glass and Mylar holding it optically flat. Care must be taken to ensure that dust does not get trapped between the glass and Mylar. For this reason, the entire process was done inside a clean box and an anti-static brush was used to clean the film before it was laid down. Using this method, reasonably good quality holographic surfaces could be adhered to glass. Tests using a collimated beam show that aberrations are not significant in the first 2 to 3 feet.

For convenience, the Mylar was glued to glass substrates and the glass subsequently was fastened to the aluminum test plug using Flexicon two sided tape. This made it possible to machine only three aluminum plugs since the sensors could be easily fastened and removed from the test plugs. The epoxy should bond equally as well to aluminum, so the holograms could also be bonded directly to the aluminum.

### 3.2.2 NICKEL SHIMS

In order to increase the durability of the Smart Surface sensors, the use of Nickel shims was investigated. The nickel shims are produced using electroplating and are used for the embossing



process. The shims can, in principle, be grown to any thickness but are typically produced in the 30-50 micron range. Although very durable when mounted, the shims are relatively flimsy in free form. This makes them difficult to mount while maintaining flatness and smoothness (much the same as the Mylar holograms). To overcome this problem we had extra thick shims grown. The difficulty in producing the thick shims is that mechanical strain tends to build into the thicker foil, resulting in overall warpage. CFC Applied Holographics was able to produce shims in the 200 - 400 micron range that had an acceptable amount of warpage. These shims had sufficient thickness to avoid most of the problems encountered when mounting the thinner shims.

Three additional problems surrounded the mounting of the shims on the test plugs: 1) reflectivity, 2) bonding, and 3) cutting. The raw reflectivity from a polished Nickel surface is only about 60% at blue wavelengths. While this is much better than uncoated photoresist (4%), it is almost half the reflectivity of aluminized Mylar or photoresist. In order to enhance the reflectivity, the shims were vacuum coated with a 50 nm layer of aluminum and then a 10-nm layer of  $\text{SiO}_2$ . This increased the raw reflectivity to almost 95% without compromising the durability of the sensor (because the aluminum to nickel bond is very strong). The coated shims were then adhered to the aluminum test plugs.

Most epoxies could bond Nickel to aluminum; however, the peel strength was very poor (although the tensile strength was very good). The shims could easily be peeled from the substrate by first snagging one of the edges. This proved very frustrating since any handling of the mounted shims usually resulted in the snagging of an edge and started the peel back process. After a good deal of investigation, a two-part adhesive system (Dymax 846 Adhesive) was found to give satisfactory results. The two-part adhesive works by painting on an activator to one of the surfaces and an adhesive to the other. The two parts are joined and held for 10 - 60 seconds at which point the two surfaces are bonded. Full cure is obtained in 24 hours. The system offers very high peel strength. To bond the shims with acceptable flatness, it was necessary to hold the shim flat with a vacuum chuck during the bonding process. To accomplish this, a vacuum chuck capable of holding a 8"x10" shim was machined out of Plexiglass.

Cutting of the shims to the desired size (1.499 inches Dia.) was also a challenge. The relatively delicate nature of the shim prevented the use of any conventional metal cutting machinery. Instead, a  $\text{CO}_2$  laser cutting facility was used. This resulted in very high precision cuts that did not mar the holographic surface. As an initial test, a single 70-micron shim was cut using this method. The resulting circular shims were very high quality; however, there was no easy way to hold the shim flat for mounting. Small vacuum chucks always resulted in the leakage and subsequent warpage around the edges. This problem was overcome by first mounting the aluminized shim to a 1/8" thick stainless steel plate using the Dymax adhesive. The adhesive was allowed to fully cure and then the stainless backed shim was laser cut. This resulted in acceptably durable holographic disks that could then be adhered to the test plug. An unfortunate consequence of gluing before the laser cut was that the adhesive near the cut line was locally heated and expanded. This caused some minor warpage near the edge of the disk. This problem could have been reduced by using thinner or less dense metal for the substrate, originally, stainless steel was thought to be one of the best materials for cutting, but it was later discovered that lighter metals would be better. There may also exist some high peel strength epoxies that may be

more tolerant of the heat produced during the cutting process, but the time schedule of the project did not allow investigation into other techniques.

### 3.2.3 PHOTORESIST ON GLASS

The final method of sensor installation is to directly mount the photoresist coated substrate on the test plug. The hologram is recorded on the photoresist coated glass plate, and the developed hologram is then silvered and coated with a thin layer of  $\text{SiO}_2$  for protection. The plate is precut to the desired size (1.5-inch circle) and fitted to the test plug after development and processing. The test plug must be machined down to compensate for the thickness of the plate. This method provides the best optical quality because there is no replication process; however, the durability of the holographic surface is substantially less than that of the nickel or even the Mylar. In addition, photoresist dissolves with most solvents (except water) so cleaning the surface is difficult.

The best compromise can be obtained by coating the back surface of the glass substrate with photoresist and recording the hologram so that it can be replayed with a reconstruction beam incident on the front side of the glass. The hologram can be developed and silvered and then coated with an epoxy to seal the photoresist. The front surface of the glass can be anti-reflection coated to reduce back reflections and is extremely durable compared with any of the previous methods. This is exactly the method used in the production of the FAN fringe sensor. Although not truly a surface hologram, this method offers the best performance and durability. The drawbacks to this method are that the resulting sensor is a 2-5 mm thick disk which may be more difficult to mount, and it requires individual recording and development of each sensor, which is more costly than either the Mylar or nickel replicas. It has been our experience, however, that this is the preferred method to use because of the gains in optical quality and durability.

### 3.3 CURVED SURFACE DEVELOPMENT AND ETCHING

In the course of the Phase II program, we investigated the possibility of recording sensors on curved surfaces. One of the virtues of holographic recordings is that they have the ability to compensate for distortions caused by reflections from arbitrary surfaces. Thus, the smart surface can be recorded on curved aerodynamic surfaces as well as flat ones. Unfortunately, recording holograms on curved surfaces that will reconstruct without aberrations is more challenging than recording on flat surfaces. Recording of holograms that will correct for surface curvature when reconstructed requires a reference beam that is the phase conjugate of a reflected plane wave from the recording surface. Recording on flat surfaces also requires a phase conjugate reference beam; however, in this case the phase conjugate beam is simply another plane wave or collimated beam. The phase conjugate wave can be generated by replaying a second hologram that was recorded using a plane wave and the reflected wave from the curved surface. This process is shown schematically in Fig. 29. In the first step, a hologram H1 is recorded using a reflected plane wave from the curved surface and a second reference wave. The hologram is developed and placed back in the setup. H1 is now reconstructed using the phase conjugate of reference beam #2. If reference beam #2 is a plane wave, then the reconstruction beam is also a plane wave but one that travels in the opposite direction. This will create the desired phase conjugate of the surface reflection. In step 2 the phase conjugate reflection is combined with an object wave at the curved

surface to record the smart surface hologram. After development, the object wave can be reconstructed by simply illuminating the smart surface hologram with the original reference beam #1 (a plane wave).

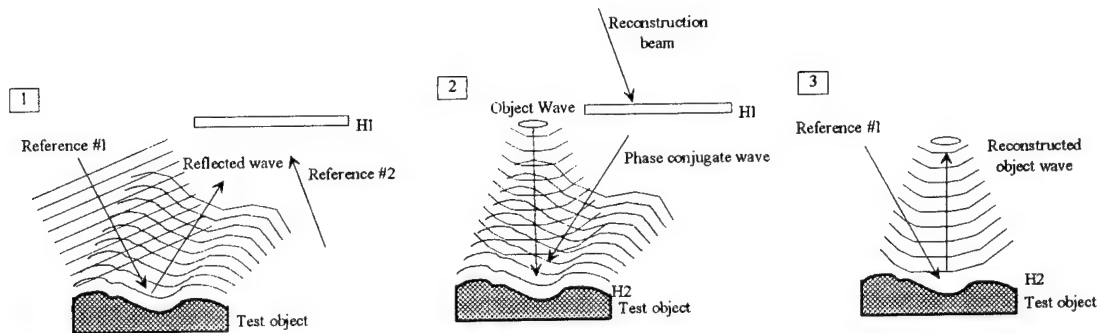


**Fig. 29. Process for recording a corrected hologram on a curved surface. Step 1 - record hologram H1 of reflected plane wave. Step 2 - Replay H1 in a phase conjugate geometry and combine with object wave at surface to record H2. Replay of surface hologram using original plane wave to reconstruct unaberrated image of object.**

Although this process is fairly straightforward conceptually, in practice the procedure is difficult. The difficulty is in avoiding exposure of the smart surface hologram, H2, during recording of the corrector hologram, H1. It is possible to coat the test object after exposure of the corrector hologram; however, the test object must be returned to precisely the same location after coating, and the coating must be very thin and uniform so that the shape of the coated surface is not significantly different from the uncoated one. Likewise, the realignment of hologram H1 back to its original position after development is also critical. These difficulties can be overcome by using a real-time holographic material that requires no chemical development. A real-time material such as Bacteriorhodopsin or Bismuth Silicon dioxide (BSO) can be used to record the phase conjugate corrector hologram *insitu*.<sup>7</sup> The hologram develops without any chemical processing on the order of 100's of milliseconds. In addition, these materials respond in both the blue and the green so that the corrector hologram can be recorded using green light, where the photoresist is not sensitive and replayed with blue light where the photoresist is sensitive. This avoids the problem of over-exposing the resist. This one step recording process is shown in Fig. 30.

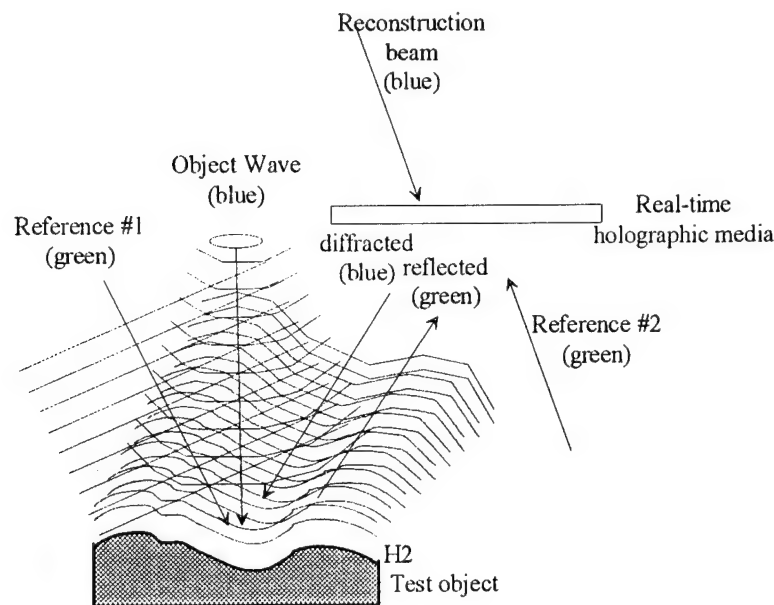


Fig. 30. Single step process for recording corrected hologram on a curved surface.

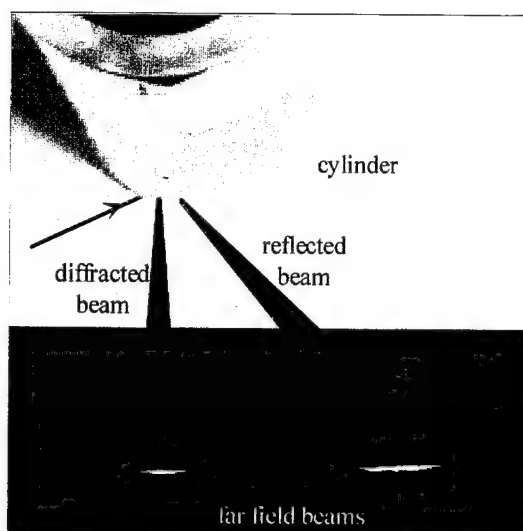
We investigated the two-step method for recording holograms on curved surfaces using conventional holographic films for the corrector plate. The first task in the process, however, was to develop a method to coat curved surfaces with uniform layers of photoresist. The spray coating technique offered an easily extendible technology to coat curved surfaces; however, the surface quality was only marginal even for flat plates. The spin coating system developed previously, was successful in coating flat plates, but lacked the ability to coat curved surfaces. We investigated the possibility of coating on top of thin plastic films backed by glass substrates using the spin coater. The hope was that these high quality, thin films could then be peeled from the glass and affixed to the desired curved surface. We achieved some initial success with this method but found that when peeled from the glass backing, the film developed thin, finely spaced cracks or striations. This was enough to negate any advantages gained by depositing the uniform layer with the spin coating technique. After exploring alternatives, we successfully developed a "pull coating" technique for depositing ultra-thin layers of photoresist and anti-reflection backing material to flat and curved objects.

Pull coating works by immersing the model or object in photoresist (or anti-reflection coating) and slowly drawing the object out of the fluid. Somewhat counter-intuitively, the slower the object is removed from the fluid the *thinner* the coating is. Thus, some degree in uniformity and repeatability can be achieved by drawing the sample at a constant rate. In practice, two factors make this method a bit more difficult. If the object displaces a significant amount of fluid in comparison to the total volume of the container, then the fluid level in the container will rise as the object is lowered into the container. This leads to a nonlinear relationship between object position and fluid level on the object. Constant pulling rates then do not lead to a uniform fluid level decrease. Fortunately, this problem is partially offset by the effects of gravity. Gravity tends to produce coatings that are thinner at the top and thicker at the bottom. The fluid level problem results in higher effective pull rates at the top and slower pull rates at the bottom, leaving a

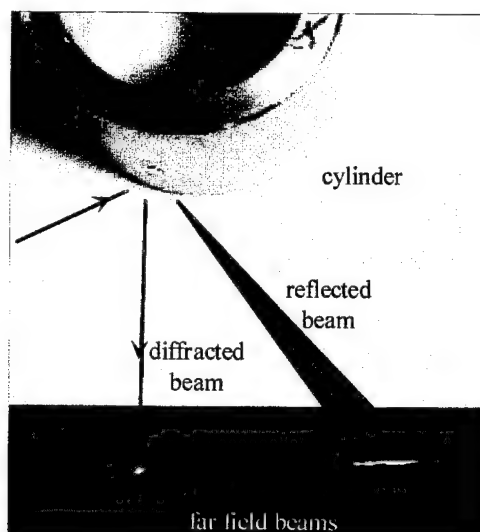
thicker coating on top and thinner one on the bottom, so, the two effects tend to cancel each other. The best coatings are then obtained by varying a combination of the pulling speed, fluid viscosity and the ratio of container volume to object volume.

We have coated flat substrates using a container to object volume ratio of about 4:1 and a pulling speed of about 0.5 mm/second. Though not as good as the spin coating technique, reasonable quality films were obtained. To obtain the thinnest possible coatings we pull the object very slowly. At speeds below 0.5mm/second our pulling device begins to move in a stepwise fashion rather than in a continuous manner. This leads to coatings that have discrete steps in the resist profile. Surface quality was examined by visual inspection of the coating while tilting the plate at approximately 45°.

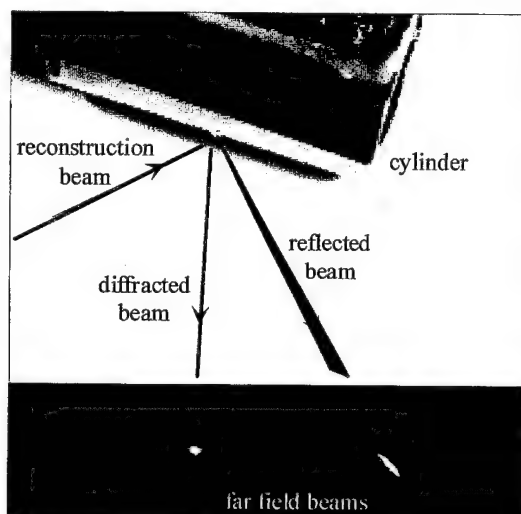
Single layer photoresist and a combination layer of anti-reflection material followed by photoresist have been deposited on glass and polished metal substrates. We have successfully recorded and developed good quality holograms on both types of these test pieces. We have also coated polished metal cylinders anti-reflection and photoresist layers, and successfully recorded holographic gratings on the cylinders using a phase conjugate reference beam for compensation. Fig. 31 shows images obtained by reconstructing four different holograms. Fig. 31a shows the fanning that results in the diffracted beam when phase conjugate compensation (PCC) is not used. Figs. 31b and c show how PCC corrects for surface curvature and produces a collimated diffracted beam. Fig. 31d shows the reconstruction of a PM5 sensor recorded with PCC on a cylinder. These experiments clearly demonstrate the ability to record OSS on curved surfaces.



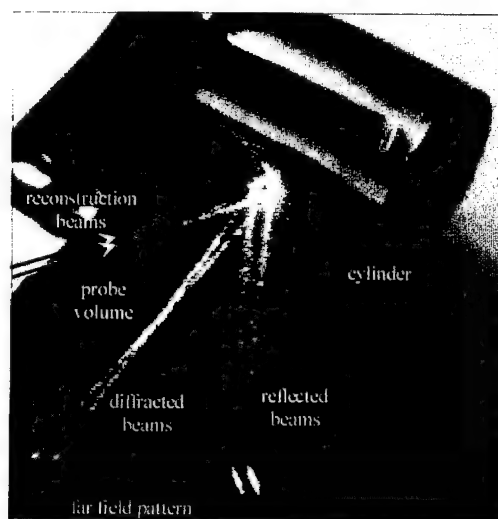
a)



b)



c)



d)

Fig. 31. Reconstruction of holograms recorded on stainless steel cylinders. Far field patterns of diffracted and reflected beams are visualized with a card. Beam paths are drawn in to clarify geometry. The three different holograms are: a) recorded with phase conjugate compensation, reference beam contained in sagittal plane, b) recorded with phase conjugate compensation, reference beam contained in radial plane and c) recorded *without* phase conjugate compensation, reference beam contained in radial plane.

As part of the curved surface development, we explored ways to etch gratings into the metal substrates after the holograms are recorded. The simplest form of etching is chemical etching. In this process the photoresist is developed so that the groove profile comes close to or touches the metal. This can be done through a combination of exposure time, developer strength and development time. An acid is then used to etch into the metal, hopefully retaining the profile of the resist. We attempted etching into stainless steel substrates using an etchant comprised of 10% hydrogen chloride, 30% nitric acid and 60% water. First attempts at etching were done by recording low spatial frequency gratings (0.5mm spacing) using a mask and a single beam. The pattern of the mask was exposed to the laser light for varying times and then developed. Using this method, we could determine the proper combination of exposure and development to have the exposed regions just touch down onto the substrate. Approximately 15 seconds of exposure at  $30 \text{ mW/cm}^2$  and 30 seconds in a developer solution of 6:1 was adequate for touchdown. These times will vary greatly depending on the thickness and freshness of the resist. Resist that has dried for many days usually requires more time to develop.

Acid was then applied to the large period gratings and allowed to etch for 30 seconds. The acid was then washed off and the remaining resist stripped using acetone. The 0.5-mm gratings were clearly visible and well defined. This grating was too large to diffract light, however. Holographic gratings were then recorded (grating periods of 1-2 microns) using an exposure range centered around 15 seconds. They were then developed using the same procedure as in the previous experiments. At this stage, holograms were still visible on all but the most heavily exposed recording. The acid solution was applied to the surface and allowed to etch for 30 seconds. After washing the acid away it was clear that the etching followed one of two processes. Either no etching took place if the solution did not actually come into contact with the metal or the etching would spread horizontally, undermining the fringes in the area neighboring the touchdown spot. Stripping away the resist with acetone also confirmed this behavior. No evidence of holographic gratings were found in the metal. Fig. 32 illustrates the two types of test results.

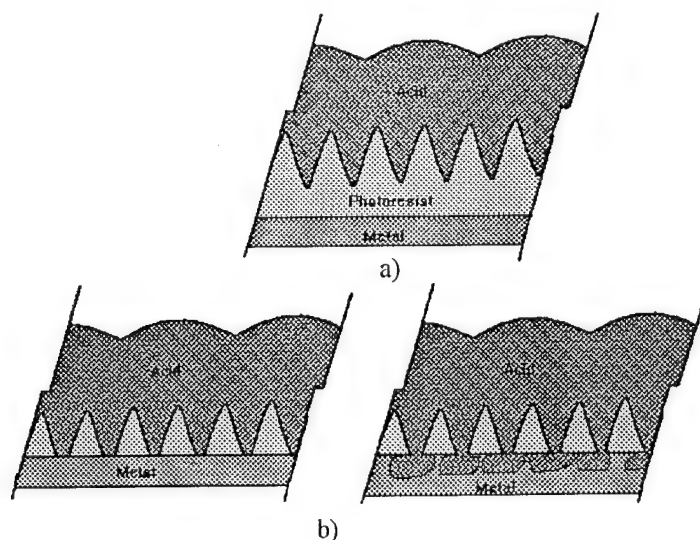


Fig. 32. Two types of etching styles exhibited; a) no etching due to noncontact and b) contact during developing but heavy lateral diffusion and undermining.

We are of the opinion that chemical etching does not have the resolution and/or direction selectivity necessary for holographic etching. Ion milling or plasma etching techniques, currently used for integrated circuit fabrication, do offer the possibility of achieving the resolution necessary, however, they are very costly. In addition, the optimal resist profile for etching is likely not to be the best profile for optimized diffraction efficiency<sup>6</sup> (blazed). In fact, etching will likely introduce significant distortions to the diffracted beams due to differences in the initial and final surface relief patterns. The etching process is extremely sensitive to the coating, exposure and development processes, making the ability to obtain high quality etched gratings very difficult.

The electroplating process used to grow nickel shims on flat plates should, in theory, work just as well for curved surfaces. The difficulty after the shim is produced and removed from the model is that, 1) it has the inverse curvature and grating pattern needed (i.e. inside out) and, 2) it does not remain optically smooth. We believe that this can be overcome by casting a mold that will bond to the nickel layer, possibly out of a hard resin or epoxy. The mold can then be separated from the original model leaving an optically smooth but inverted version of the model. The shimming processes is then repeated, growing the new shim from the first mold. A second casting is performed and this time upon separation of the two parts, we are left with an exact replica of the original model but with a nickel skin. The skin contains a replica of the hologram and is bonded to the casting material underneath which can be machined or joined with other parts. Although it seems somewhat complicated, it is really only an extension of known and proven technologies. The method is completely insensitive to resist thickness and groove depth, requiring only that a good hologram is recorded on the surface (which we can do routinely now). This appears to be the most likely method to produce durable surface relief gratings on curved surfaces.

While we demonstrated the recording of a corrected hologram on the surface of a cylinder coated with photoresist, practical application of this technique would be difficult. First, the coating of large or complex models would be challenging in practice. Second, the durability of the resist coating under test conditions would be poor. Finally, post processing would require placing the model in a vacuum chamber for aluminizing. It is our belief now that Photopolymer materials offer the best alternative for curved surface development. This technology is discussed in Section 5.1.



## **4.0 SMART SURFACE TESTING**

The PM5, RR50 and FAN sensors were tested in a calibration channel at UCI and in a trisonic wind tunnel at WL. Calibration channel testing validated the sensor readings against conventional pressure and velocity sensors. The PM5 sensor was successfully tested at UCI in the calibration channel up to center channel velocities of 85 m/s. The PM5 gave accurate readings at probe volume heights down to 3 mm above the surface, exceeding the design goal of 5 mm. Signal-to-noise ratios as high as 20:1 were achieved using the minimum laser power of about 30 mW. This sensor was also successfully tested using the AOM to frequency-shift one of the beams. The AOM can extend the range of the PM5 sensor to supersonic speeds. Boundary layer profiles were measured with the PM5 and with conventional hot wire sensors. The smart surface data showed excellent agreement with the hot wire sensors.

The RR50 sensor was also successfully tested in the calibration channel. Probe volume heights in the range of 10 mm to 50 microns were achieved, exceeding the design goal of 10 mm - 200 microns. The RR50 and PM5 sensors gave the same readings within the RMS uncertainty and were repeatable between different days. This served as validation of the RR50 sensor. Testing of the RR50 in the calibration channel under the higher flow rates was unsuccessful. The problems have been, in part, attributed to the change of the seed quality (size) between that of the humidifier in the low speed tunnel and the pressure seeder in the higher velocity arrangement. Higher flow rates required the use of Bragg shifting to ensure that the Doppler frequency did not exceed the processing electronics capabilities. With the AOM installed, the signal-to-noise ratio was very poor, particularly at heights below 1 mm. Further analysis of the sensor resulted in the identification of a simpler, alternative way to address and measure velocity with the sensor; however, at present, the sensor is still limited in its velocity capability.

The FAN fringe sensor was successfully produced and was tested in the 3/4" calibration channel at 10 m/s. The velocity profile measured by the sensor was in excellent agreement with the profile previously measured by the RR50 and PM5 sensors. In addition, the sensor was validated against differential pressure measurements in a 1/4" channel. Tests in the TGF of the FAN sensor produced data that did not correlate with theory. This discrepancy was later understood to be due to the fact that the sensor dynamic range had been exceeded. Future generations of FAN sensors could be designed to overcome this limitation.

### **4.1 METROLASER LABORATORY TESTING**

Initial testing at MetroLaser involved measuring the diffraction patterns and diffraction efficiencies of the sensors. Tables 3 and 4 respectively list the diffraction efficiencies of the PM5 and RR50 sensors used for testing at UCI and WL. Fig. 33 shows a visualization of the beams diffracting off the PM5 sensor. The sensor used here was uncoated photoresist so diffraction efficiency is much lower than final production sensors. Initial testing was done by placing a pinhole on a rotating wheel at the probe volume and measuring the scattered light. The received signal showed good uniformity across the probe volume and high contrast fringes. The sensors were then tested by injecting water particles from a humidifier into the probe volume with a fan.

Initial tests showed good signal-to-noise. After these preliminary tests, careful measurements were made in the calibration channel at UCI.

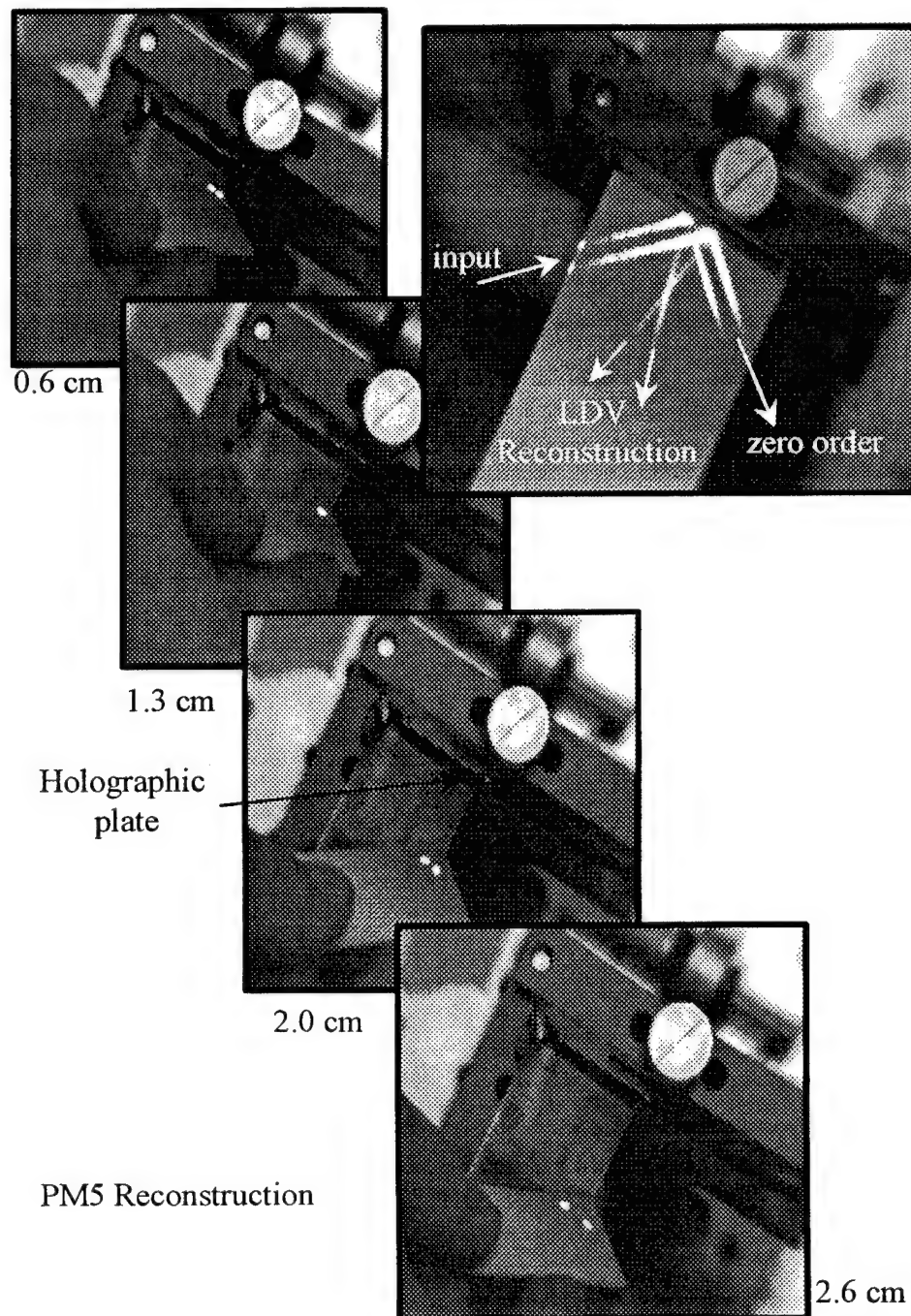


**Fig. 33. Reconstruction of PM5 sensor.** A card is used to visualize the beams as they diffract off the hologram. The hologram is recorded on uncoated photoresist. Upper right hand image shows all address and diffracted beams. Series of images starting with upper left show intersection of diffracted beams with a card parallel to the surface and displaced normal to the surface at several distances. Image at 1.3 cm shows probe volume where two beams cross.

## 4.2 UCI CALIBRATION CHANNEL TESTING

### 4.2.1 CONFIGURATION AND SEEDING

The next phase of testing of the sensors involved a narrow calibration channel fitted with an optical window across from a test plug. The sensors were mounted on aluminum test plugs that could be removed quickly for cleaning and changing of sensors. The calibration channel thickness can be varied between 3.2 mm and 19 mm to allow for laminar or turbulent flow. The small thickness of the channel allows close optical access, simplifying the alignment procedure. The maximum probe volume height is limited by the width of the channel.

Channel flow was accomplished in two different ways. A squirrel-cage fan was coupled to the end of the channel and used to draw air through. For this arrangement, water particles were drawn into the channel flow by placing an ultrasonic humidifier near the mouth of the inlet. The humidifier provided very uniform seeding which was estimated to be between 1 - 10 microns. The squirrel-cage provided a nominal flow rate of around 10 m/s. The fan could be loaded by partially blocking its exit to achieve smaller flow rates.

For higher flow rates, a pressure inlet was used. The calibration channel was fitted with a pressurized intake section that consisted of a 25.4-mm-high pressure air inlet, multi-layer screen baffle for flow quality, convergent nozzle and a seeder. Compressed air was used from an industrial compressor capable of delivering 90 li/sec. For this arrangement a pressure seeder was used. The seeder consisted of two small diameter tubes (~100 microns) one supplying pressurized water and the other high pressure air. The air tap was oriented at 90 degrees with respect to the water tap to produce a shearing stream that produced particles in the 1 - 50 micron range. The calibration channel seeding and optical arrangement are shown in Fig. 34 for the case of the compressed air driver.

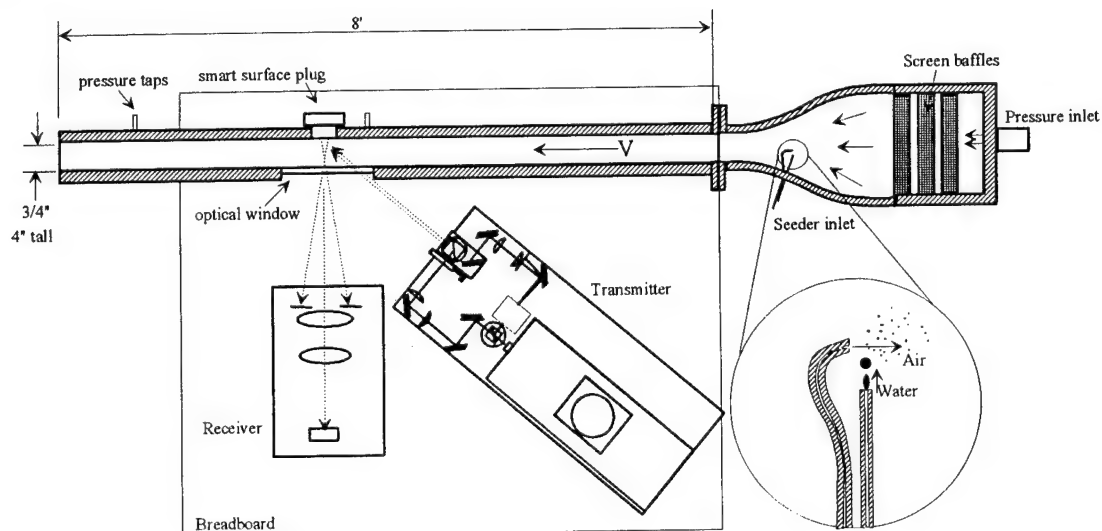


Fig. 34. Calibration channel optical setup and seeding arrangement for compressed air driver.

The centerline channel velocity was also measured using a small pitot tube at the end of the channel and by static pressure taps on the channel wall. These two methods were used to calibrate the channel for flow generated by both the squirrel-cage fan and the compressed air, independently. Thus, an independent source was available for verifying the results of the OSS. In addition, this channel has been extensively tested by UCI over many years and its flow characteristics are well documented.

#### 4.2.2 PM5

Initial measurements were made in the 3/4" channel with the squirrel-cage fan at a centerline flow rate of approximately 10 m/s. The channel Reynolds number for atmospheric temperature and pressure is<sup>8</sup>

$$Re_h = \frac{U_{cl} h \rho}{\mu} = 13,100, \quad (37)$$

where  $U_{cl}$  is the centerline velocity,  $h$  is the channel width,  $\rho$  is the density of air and  $\mu$  is the absolute velocity coefficient. This Reynolds number indicates a turbulent channel flow<sup>9</sup>. A pressure transducer was connected to pressure taps along the centerline of the channel. The pressure taps were initially placed 148 cm apart and were later reduced to 61 cm to permit operation within the range of the pressure transducer at higher flow rates (12 mm Hg). The measured values of center channel velocity were compared with those theoretically predicted for channel flow. The relationship between differential pressure,  $\Delta p_{hg}$ , and center channel velocity,  $U_{CL}$ , is given by,<sup>8</sup>

$$U_{CL} = \sqrt{\frac{2\Delta p_{hg} g \rho_{hg} D_h}{f \rho_{air} L}}, \quad (38)$$

where  $\Delta p_{hg}$  is in mm Hg,  $g$  is the gravitational acceleration constant (9.8m/s<sup>2</sup>),  $\rho_{hg}$  and  $\rho_{air}$  are the density of mercury, and air, respectively,  $L$  is the separation between pressure taps,  $D_h$  is the corrected hydraulic diameter given by  $2hw/(h+w)$ , where  $h$  and  $w$  are the height and width of the channel, respectively and  $f$  is the friction factor and can be found using the Moody chart for fully turbulent flow in a duct. For this case,  $f$  was estimated to be 0.0185.

Fig. 35 shows the data measured by the PM5 at center channel plotted with the calculated velocity as a function of differential pressure. Center channel velocity was also measured by inserting a pitot tube into the channel near the exit. The smart surface readings agree well with the values measured by both conventional sensors.

This test demonstrated the ability of the PM5 sensor to measure velocities of up to 85 m/s. The PM5 worked well with the compressed air drive and seeding arrangement. It produced data at moderate rates even with the seeding level turned down so low that no seed was visibly present in the beams to the naked eye.

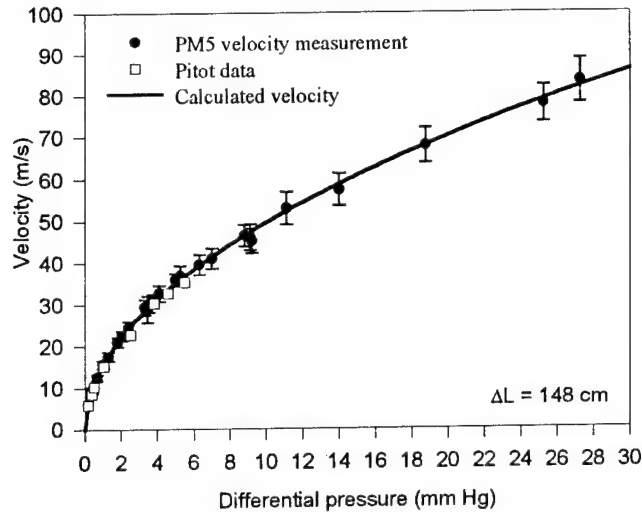


Fig. 35. Center channel velocity measured by PM5, pitot tube and calculated using [Eqn. 8] as a function of measured pressure differential. The distance between pressure taps  $L = 148$  cm and 61 for data below and above 10 mm Hg respectively. Pressure readings taken with  $L = 61$  cm were linearly scaled to represent the pressure readings at  $L=148$  cm.

A velocity profile was measured with the PM5 sensor at a center channel velocity of 30 m/s. Conventional hot wire sensors were used near the exit of the channel to measure the velocity profile. The hot wire sensor was mechanically translated across the channel. The data from the two methods are compared in Fig. 36 and show excellent agreement. The nonzero reading of the hot wire sensor at the boundary was an artifact of the sensor being placed at the exit and not fully inside the tunnel. These experiments served to calibrate the PM5 sensor.

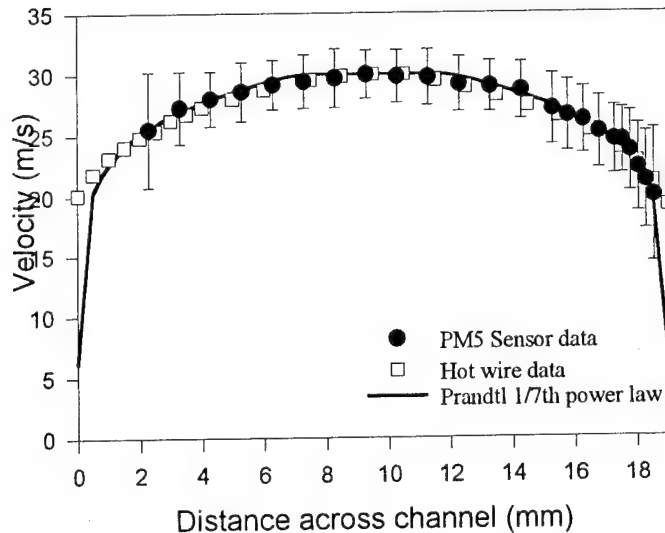


Fig. 36. Comparison of PM5 sensor data measurements using conventional hot wires in calibration channel at UCL.

Although limited in its minimum height, the PM5 sensor had no problems measuring close to the outer window of the channel. The probe volume size was 100 microns in width (along the flow direction), 900 microns tall (perpendicular to the surface) and 500 microns long. The automated positioning system allowed a greater number of positions to be measured, resulting in higher resolution. Fig. 37 plots the mean velocity as a function of position with the RMS deviation shown as error bars. The channel width,  $d$ , was measured to be 19.0 mm. Note that  $y = 0$  is at the hologram surface, and data close to 19.0 mm correspond to positions adjacent the optical window. The data were fit using Prandtl's empirical one-seventh power law for fully turbulent flow,<sup>8</sup>

$$\left( \frac{u}{U_{cl}} \right) = \left( \frac{y}{\delta} \right)^x, \quad (39)$$

where  $u$  is velocity at position  $y$ ,  $U_{cl}$  is the velocity in the center of the channel,  $\delta$  is the boundary layer thickness and  $x = 1/7$ .

Using this formula,  $U_{cl}$  and  $\delta$  were found to be 8.6 m/s and 6.7 mm respectively (see Fig. 37a). The data were also fit with Equation 9 using the exponent  $x$  as a variable. A least squares fit method, provided by Sigma Plot (Jandel Scientific), was employed. The calculation was also averaged over a 1-mm window to more accurately represent the experimental conditions. The result of the fitting is shown in Fig. 37b.

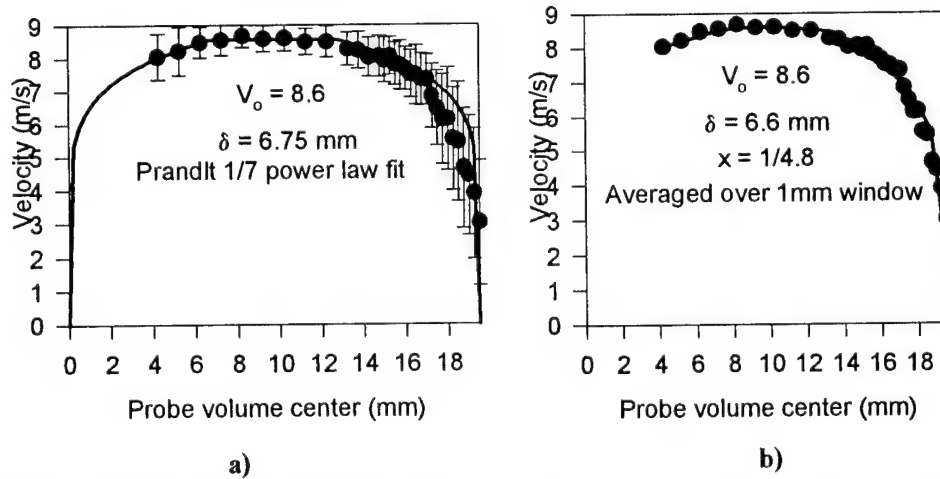


Fig. 37. Mean velocity measurements as a function of position in calibration channel. a) Line is fit using one-seventh power law (Eqn. 8), error bars represent RMS deviation. b) Fit using exponent,  $x$ , as fitting parameter and smoothed over 1 mm aperture. ( $V_o = U_{cl}$ )

During the testing, it was discovered that minerals contained in the seeding particles generated by the humidifier were depositing on the optical window and the sensor surface. This caused excessive scattering and attenuation of the optical beams. The coating layer was difficult to detect under ambient lighting conditions but was readily detectable upon illumination at certain angles with a bright, white light source. The use of de-ionized water in the humidifier, which was done

from the beginning, was thought to be sufficient to avoid this problem. It was finally remedied by switching to a humidifier that employs a special mineral filtering system in addition to using de-ionized water and by cleaning the windows periodically with a vinegar and water solution. The holographic sensors may also be cleaned lightly with the vinegar solution but, because no scrubbing can be done on the fragile surface, they must be replaced periodically.

#### 4.2.3 RR50

The RR50 sensor was tested in a similar way as the PM5 using the identical setup shown in Fig. 34. The RR50 sensor obtained velocity measurements at heights as low as 50 microns above the surface. Because the measurement ranges of the PM5 and RR50 overlap, the measurements of the PM5 can be used to validate measurements of the RR50. The data between the PM5 and RR50 showed good agreement. Data were taken on several different days and overlapping points were in good agreement between days and between sensors. Fig. 38 shows the data from five different days, including tests using an acousto-optic modulator (AOM) to Bragg shift one of the reconstruction beams and provide a frequency bias to the measurements. The AOM provides two useful functions. First it extends the range of the sensor by slowing the relative velocity between the fringes and the particles in the flow. An 80-MHz shift, equivalent to a flow velocity of 216 m/s for the PM5 sensor, extends its overall range (limited by electronic processing speed) to 350 m/s. The second benefit of the modulator is that it can be used to provide an offset frequency so that bursts from slow moving particles have Doppler frequencies well above DC, leading to higher signal-to-noise ratio. Performance of the PM5 sensor with the AOM was slightly worse than without it, primarily due to the loss of optical power through the modulator. Increasing the modulation frequency above the value used in the tests (30 MHz) is expected to improve performance since modulator diffraction efficiency increases with drive frequency. Data from the PM5 and RR50 are compared in Fig. 38.

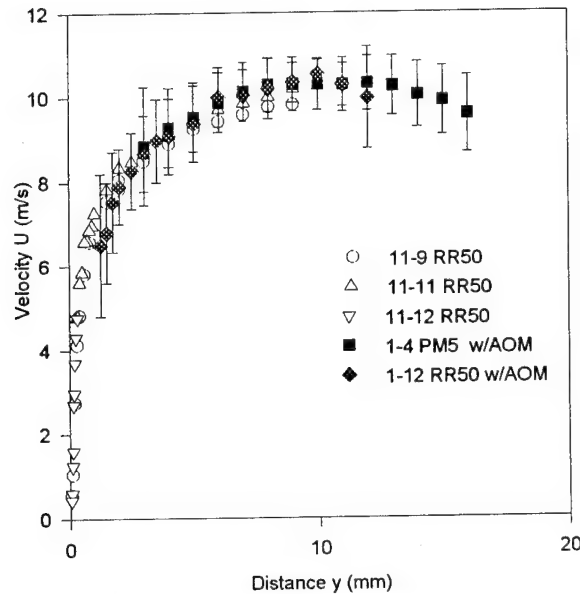


Fig. 38. Comparison of PM5 and RR50 data taken with and without the Acousto-optic modulator and on different days.

The RR50 is capable of measuring down to heights of 0.05 mm and was used to make measurements inside the boundary layer, laminar sublayer of the channel flow. For these measurements, the centerline channel velocity was 9.8 m/s. The data for this boundary-layer survey were normalized by the friction velocity,<sup>9</sup>

$$u^* = \left[ \frac{\tau_w}{\rho} \right]^{\frac{1}{2}}, \quad (40)$$

where the shear stress was calculated by

$$\tau_w = \mu \left[ \frac{\partial u}{\partial y} \right]_{y=0}, \quad (41)$$

and the velocity gradient was obtained from the RR50 sensor data within the sublayer. The data were normalized using

$$u^+ = \frac{u}{u^*}, \quad y^+ = \frac{y u^* \rho}{\mu}, \quad (42)$$

where  $u$  is velocity,  $y$  is distance from the inside channel wall,  $\mu = 1.819 \times 10^{-5}$  kg/m/s @ 20°C,  $\rho = 1.199$  kg/m<sup>3</sup> at 1 atm and 20°C. The normalized data are plotted in Fig. 39 along with two curve fits. The first corresponds to  $u^+ = y^+$  which is the theoretical linear relationship between velocity and distance inside the laminar sublayer. The second curve is a fit of the data to the law-of-the-wall expression<sup>9</sup>

$$u^+ = \frac{1}{\kappa} \ln y^+ + B, \quad (43)$$

where the theoretical values for the law-of-the-wall profile are  $\kappa = 0.40$  and  $B = 5.5$ . Equation 43 is typically valid for  $y^+$  values greater than 100. Using the points inside the laminar sublayer to determine  $\partial u / \partial y$ , we obtain a value for skin friction of 0.0042 and from the fit to data find that  $\kappa = 0.32$  and  $B = 5.3$ . An alternate method of calculating skin friction is to require the velocity data to fit Equation 43 with  $\kappa = 0.40$  and  $B = 5.5$  and then use the Clauser diagram<sup>10</sup> to determine the skin friction. Using this method we find a skin friction value of 0.0053. The fit of the data to these functions is also shown in Fig. 39.



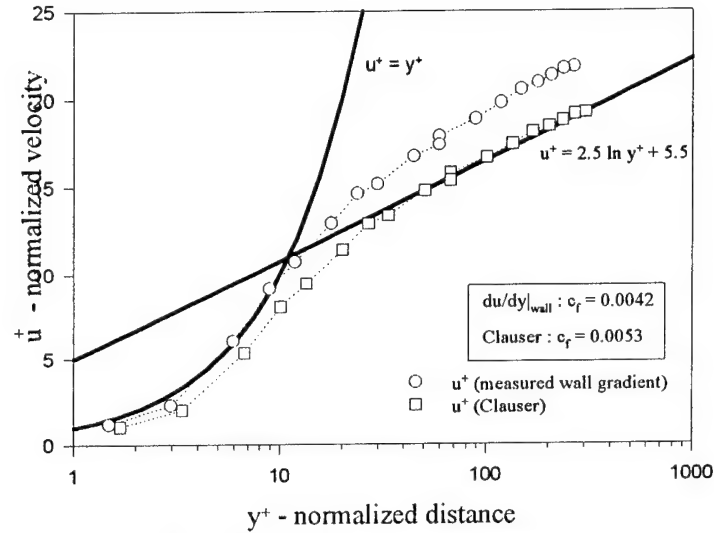


**Fig. 39. RR50 sensor data plotted in normalized coordinates and shown with law-of-the-wall fit. Two different methods were used to obtain skin friction.**

The RR50 did not perform as well as was expected using the AOM. As shown in Fig. 38, data were not measurable below a probe volume height of 1 mm. This was due to a large amount of lower frequency signals generated from scattering near the surface. Closer inspection of the problem revealed that Doppler bursts of high quality were obtained from the fringes formed by each incident and retroreflected beam. Fig. 40 illustrates the fringes formed from the incident and retroreflected beams. These fringes have a very small spacing ( $\lambda/2$ ) and, in addition, scattering off of the incident beam is in the backwards direction. Our initial calculations showed that the fringe contrast from these fringes should be very poor and signals from the forward scattering probe volume should be much larger. Experimentally, we see that the signal from the small fringes formed by the single beam are quite high in contrast and easy to measure. The projection of the small fringe spacing along the particle velocity direction is identical to the fringe spacing caused by the two beam forward scattering probe volume. Because of this, the Doppler frequencies from the two mechanisms are identical and therefore, when not using the AOM, it is impossible to distinguish which signals are generated from each mechanism. When using the AOM it became obvious that signals were generated from the small period grating because signals from the larger grating had a frequency offset. Further confirmation of this process was obtained by blocking one of the beams and measuring the signal in the absence of the large period probe volume.

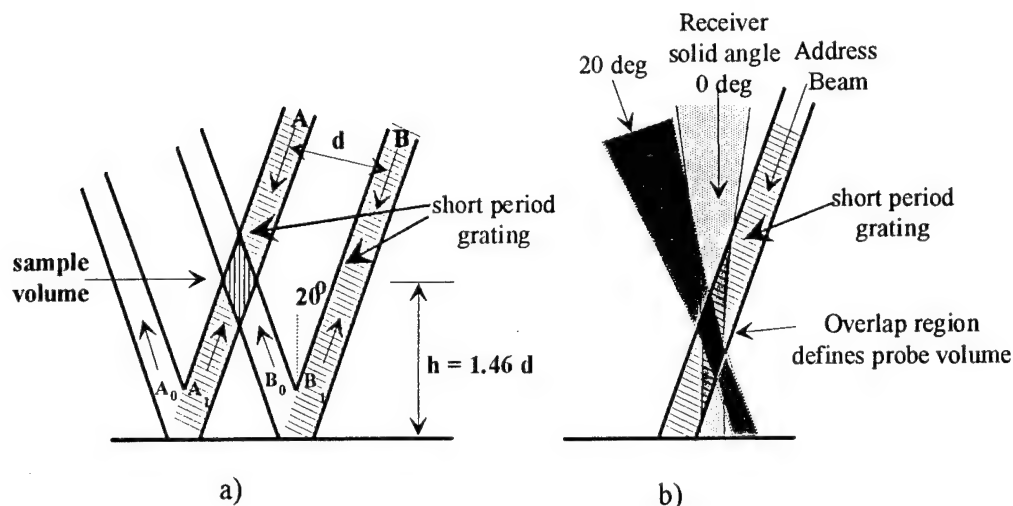


Fig. 40. (a) Two beam RR50 sensor having both long and short period gratings. (b) Single beam RR50 where probe volume is defined by overlap of receiver and address beam. Size of probe volume is reduced with receiver at 20 degree angle.

Discovery of the scattering from the small period grating has great significance on the operation of the RR50 sensor. This second signal manifests itself as a source of noise when using the RR50 in its regular configuration, especially at heights near the surface (see Fig. 39a). Two methods can be used to try to overcome this noise. The first is to construct the probe volume out-of-plane. Unfortunately, this has the disadvantage of moving the probe volume in two dimensions rather than only normal to the surface, and at low heights, the additional beams will still cause scattering. The second method is to use an AOM since the signals from the large period probe volume have a frequency offset. Filtering of the lower frequency bursts is difficult; however, with the proper filtering electronics, this method should work. Perhaps the best solution is to use the out-of-plane configuration with the AOM.

Because the signals from the small period grating are so strong, we have investigated using this signal to measure velocity. This has the decided advantage that only a single beam is needed to address the sensor, making the transmitting optics extremely simple. It does have two drawbacks in that a frequency shift is no longer possible, limiting the maximum measurable velocity and detection of flow direction, and registration of the exact probe volume location difficult. The probe volume location is defined by the overlap of the receiver solid angle and the address beam (see Fig. 40b). Movement of either the address beam or the receiver will move the effective probe volume location. Accuracies in determining the position of this overlap will limit the ability to register the probe volume location. With our present system, alignment is limited to within about 200 microns. To demonstrate the operation of the single address beam, adjustable height sensor, we scanned the 3/4" channel using the identical setup as the RR50 but blocked one of the beams. Data from this scan showed good agreement with data taken from the two beam system. By moving the receiver 20 degrees off axis, the size of the probe volume will be reduced, increasing the resolution of the measurement. We believe that this sensor has applications in low to medium flow rate applications.

#### 4.2.4 FAN FRINGE

The FAN sensor was cemented into the calibration channel and oriented to measure the streamwise velocity component. Fig. 41 shows the optical arrangement.

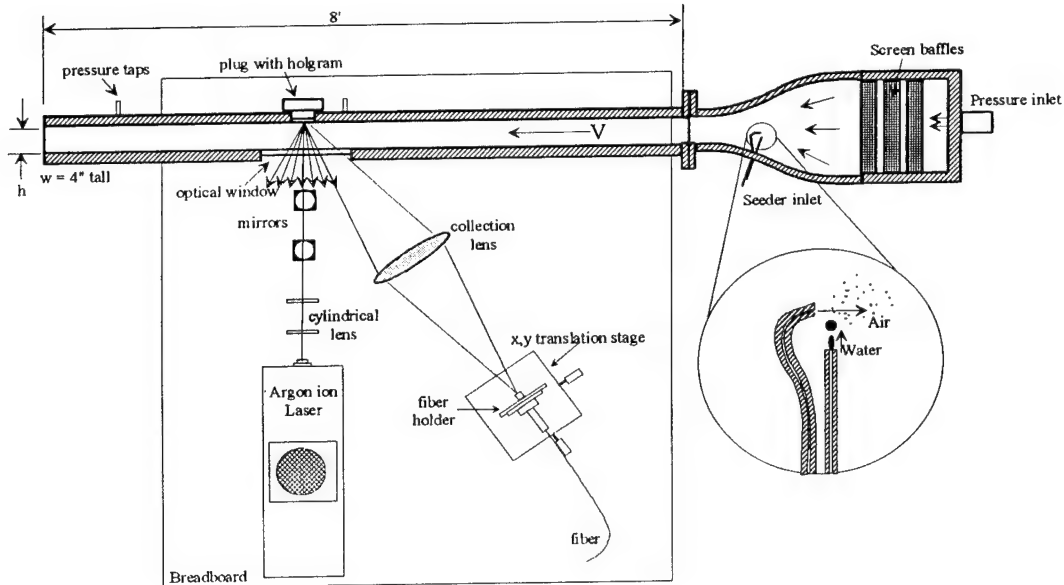


Fig. 41. Optical arrangement for testing of FAN sensor in the UCI calibration channel.

A typical burst distribution measured with the fan fringe sensor in calibration channel at 10 m/s is shown in Fig. 42. The mean value is 16,400/s ( $\tau = 0.295 \text{ N/m}^2$ ) with an RMS deviation of 36.7%. This velocity profile agreed well with the data measured using the RR50 sensor. A comparison of the fan fringe and RR50 data is shown in Fig. 43.

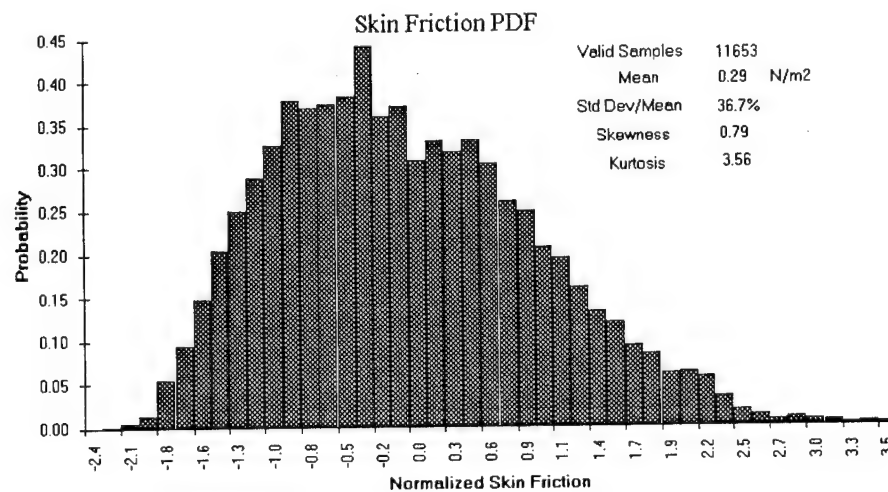
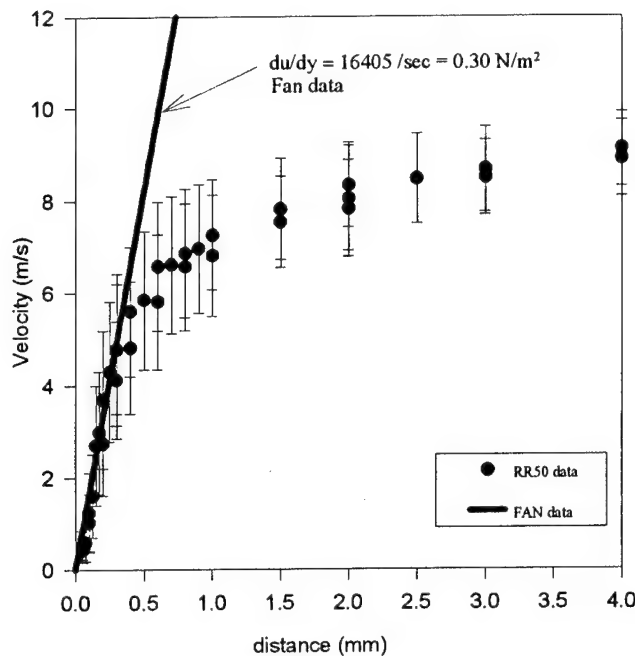
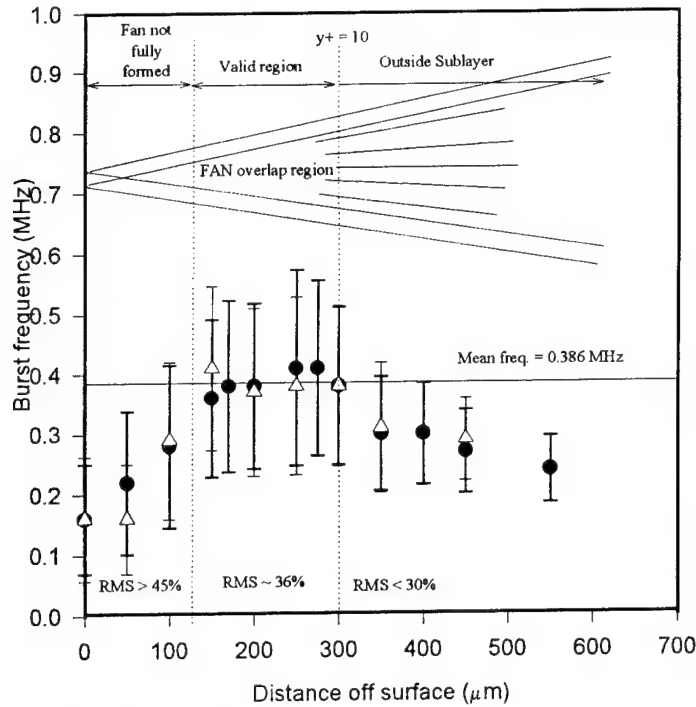


Fig. 42. Probability density function for normalized skin friction measurement in 3/4" channel with  $u_{cl} = 10 \text{ m/s}$ .



**Fig. 43. Comparison of FAN sensor data with RR50 boundary layer survey data. 3/4" channel with  $u_{cl} = 10$  m/s**

Data were collected as a function of receiver alignment. It was found that the measured mean and standard deviation were strongly coupled to the alignment. Fig. 44 shows a plot of burst frequency vs. alignment of the measurement volume with respect to the surface. In general, near the surface RMS values were greater than 50% and the mean was much lower than expected. This result was attributed to light scattered by particles in the region of incomplete fan fringe formation. At approximately 120 microns, the RMS approached the generally accepted value of 36% for turbulence intensity within the sublayer<sup>11</sup>. The mean value also represented a reasonable value for the velocity slope. Between 120 and 300 microns, the mean value remained constant to within 10% and RMS remained between 35% and 39%. Beyond 300 microns, both the mean and RMS values decreased. These results are consistent with what is expected due to the rolling over of the velocity outside of the sublayer. The results were not significantly effected by the use of 50 or 100 micron core fiber and were repeatable on different days. We believe that valid data can be measured at heights above 100 microns but the maximum height is bounded by the sublayer thickness.



**Fig. 44.** Measured burst frequency from the FAN sensor as a function of receiver alignment. Circles are data taken using 100-micron fiber and triangles represent 50 micron fiber data. Diagram on top helps to illustrate three regions: Low region - fan is not completely formed, Mid region - valid sensor region, High region - outside laminar sublayer.

To measure shear stress over a wide range without running into limitations on compressor flow rate, the channel width was reduced to 1/4". The FAN sensor was glued in the channel with Duco cement (dissolvable in acetone) using a straight edge ruler to ensure that the sensor and wall surfaces were flush. The receiver was positioned so that it collected scattered light from the region of the fan fringes located 120 microns above the surface. Fig. 45 shows the measured shear stress versus differential pressure between taps located 24" apart in the channel. The solid line represents the mean shear stress calculated using

$$\bar{\tau} = \frac{\Delta p(w \cdot h)}{2L(h + w)}, \quad (44)$$

where  $\Delta p$  is the pressure differential (note  $\Delta p = \Delta p_{hg} \rho_{hg} g$ ),  $L$  is the distance between pressure taps,  $h$  is the height of the channel and  $w$  is the width. In this case  $h = 0.635$  cm,  $w = 10.2$  cm and  $L = 61$  cm. The error bars in Fig. 45 represent the uncertainty in the sensor transfer function ( $\lambda/S$ ) and the 8 bit digitization resolution. Above  $2 \text{ N/m}^2$ , the sublayer thickness falls below 100 microns which is less than the sensor's minimum measurement height. This is evident by the rolling off of the measured shear stress with increasing pressure. With improved recording techniques (the use of precision masks to form the slits during recording) the minimum height could be reduced by a factor of 4, extending the measurement capability (shear stress dynamic range) by a factor of 16.

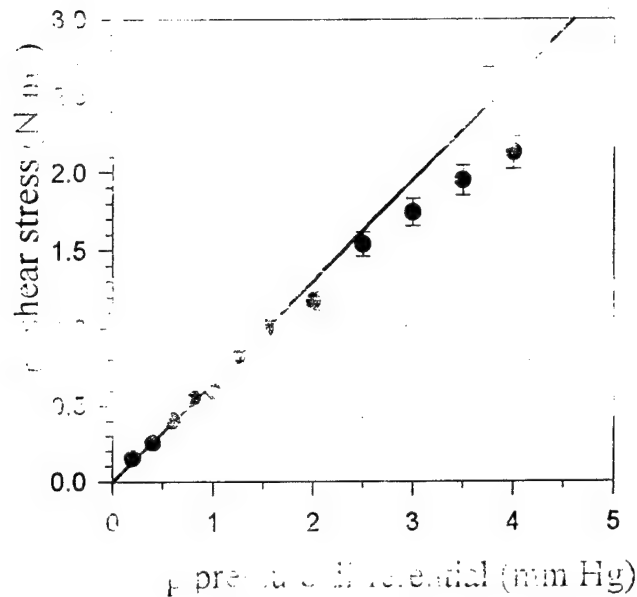


Fig. 45. Shear stress measured using FAN sensor as a function of differential pressure measured between taps separated by 24" in 1/4" channel. Increasing pressure corresponds to higher flow rates. Line indicates theoretical mean shear stress calculated from Equation 44.

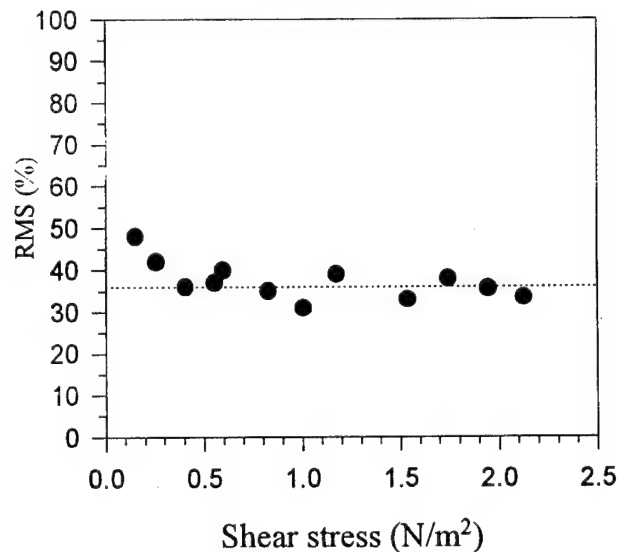


Fig. 46. RMS values for measured by FAN sensor as a function of shear stress. RMS values correspond to data shown in Fig. 36.

Fig. 46 shows the measured RMS distribution at each of the data points from Fig. 45. The average RMS value is 36% excluding the 47% value measured at a shear stress value of 0.2 N/m<sup>2</sup>. The channel flow was not fully turbulent at this value so a correspondingly higher value of turbulence intensity is expected.

### 4.3 MEASUREMENT UNCERTAINTY

Several factors contribute to the measurement uncertainty of the smart surface sensors. The electronic burst processing is similar to conventional LV measurements with uncertainties introduced from the digitization and signal processing algorithms. The Fast Fourier Transform (FFT) processing introduces an uncertainty which is a function of the bin-width. Because the bin width,  $\Delta f$ , is fixed for a given sample frequency,  $f_s$ , and sample size, the measurement uncertainty is then a function of the measured frequency,  $f_D$ . Lower measured frequencies will have a higher uncertainty percentage ( $\Delta f / f_D$ ). For experiments typical of the PM5 and RR50 sensor, an FFT size of 128 was used and sampling rates were changed when average burst frequencies fell below  $f_s/10$ . This leads to a worst case uncertainty of 8% which can be considered a random error introduced for each individual measurement. With ensemble averaging, the random error is reduced by a factor of  $1/\sqrt{N}$ , where  $N$  is the number of samples averaged. The minimum sample size used was 100 points, leading to an uncertainty of 0.8%. In many cases the averaging sample size was 1,000 resulting in an uncertainty due to the processing electronics, of 0.25%. This uncertainty is typical of LV measurements using FFT processing.

Unique to the Smart Surface sensors is an uncertainty arising over the fringe spacing in the probe volume and probe volume location, respectively. The fringe spacing uncertainty is caused by the uncertainty in measuring the incident angle of the address beams and/or the diffracted beams. This will cause a systematic error in the burst frequency measurement. The probe volume location uncertainty is also caused by the uncertainty in the address beam angle as well as by the uncertainty in the measurement of address beam separation.

Typical uncertainty for measuring address beam angle,  $\Delta\theta$ , is 1 degree. Because it is made interferometrically, the uncertainty for measuring the parallelness of the two address beams,  $\Delta\theta'$ , is 0.1 degree. The uncertainties that propagate into the fringe spacing and hence, Doppler frequency are detailed in Table 5. The overall uncertainty of the measurement is driven by the systematic error introduced by the geometric alignment. By measuring the far field angle between the diffracted beams,  $\alpha$ , the fringe spacing can be measured to better than 1%. Direct measurement of this angle is recommended for the highest precision.

The uncertainty in probe volume location was primarily a function of the uncertainty in measuring address beam separation,  $\Delta d$ , which was typically 20 microns. The angular alignment of the address beams also adds uncertainty; however, the contribution from  $\Delta d$  was the most significant.

**Table 5.**

**Experimental uncertainties arising from optical alignment and their contribution to frequency measurement and probe volume position. These are systematic errors.**

Quantity	Typical	PM5 $\Delta\lambda/\lambda$	PM5 $\Delta h$ (/h)	RR50 $\Delta\lambda/\lambda$	RR50 $\Delta h$
angle $\Delta\theta$	1 deg	3%	(3%)	3%	(3%)
parallel $\Delta\theta'$	0.1 deg	1.3%	(1.3%)	0.65%	(0.65%)
separation $\Delta d$	20 microns	---	$\pm 0.2\text{mm}$	---	$\pm 0.030\text{ mm}$
diff. angle $\Delta\alpha$	0.1 deg	1%		1%	
Worst case	----	4.3%	$\pm 0.2\text{mm}$	3.7%	$\pm 0.030\text{ mm}$

#### **4.4 WL SURVIVABILITY TESTING**

The optically smart surfaces (photoresist on glass substrates) were tested in the Wright Laboratory Mach 3 HRNF by WL personnel to determine survivability at sustained Mach numbers.<sup>12</sup> A 15-degree wedge was designed with two indented areas for mounting 4" x 5" aluminum plates with optically smart surfaces. The plates are mounted such that one plate is parallel to the freestream velocity, and the other plate is mounted at a 15 degree angle of attack relative to the freestream velocity. Operating conditions for the Mach 3 HRNF were published by Fiore, et.al.<sup>13</sup>

For this set of experiments, the tunnel was operated at stagnation pressures of 0.586, 1.034, and 2.069 MPa, respectively, which corresponds to a Reynolds number range of 48.9 to 172.5 million/m at a stagnation temperature of 278 K. The static temperature at these conditions is around 83 K and thus the tunnel and model begin collecting frost upon tunnel shutdown. A summary of the test runs and their conditions is shown in Table 6. Note that for Run 1 the tunnel had not been operated for approximately 12 months and a thin layer of rust had formed on the tunnel sidewalls. This resulted in the first run having a large content of abrasive particles present in the freestream flowfield. This was considered the worst case scenario that might be encountered by the optically smart surfaces.

During Run 1, the optically smart surfaces parallel to the freestream flow survived the abrasive flowfield satisfactorily; however, the surface at the 15 degree angle of attack was essentially sand-blasted to the base aluminum surface in a period of approximately 2 seconds. It is believed that the particles impinging on the optically smart surfaces were on the order of 10  $\mu\text{m}$  in diameter and thus would impact the model further from the leading edge and be entrained in the boundary layer.

Prior to the second run, the model was heated to the point where water vapor was no longer freezing on the model surface and the plate that survived Run 1 was moved to the 15° angle of attack position for the remaining runs. Run 2 was begun at a stagnation pressure of 0.586 MPa for 45 seconds. Little or no visible deterioration of the smart surfaces took place at that condition for approximately 30 seconds. Again, no visible deterioration took place. Finally, the stagnation



pressure was increased to 2.069 MPa. At this condition, the surface began deteriorating immediately and after 15 seconds, the surface had been essentially sand-blasted to the base aluminum.

**Table 6.**  
**Survivability test conditions**

<b>Run No.</b>	<b>Plate</b>	<b>Plate Angle of Attack (degrees)</b>	<b>Stagnation Pressure (MPa)</b>	<b>Reynolds Number</b>	<b>Run Duration (seconds)</b>
1	1	15	1.034	$86.2 \times 10^6/\text{m}$	55
1	2	0	1.034	$86.2 \times 10^6/\text{m}$	55
2a	2	15	0.586	$48.9 \times 10^6/\text{m}$	45
2b	2	15	1.034	$86.2 \times 10^6/\text{m}$	30
2c	2	15	2.069	$172.5 \times 10^6/\text{m}$	15

The conclusion of this series of testing is that the survivability of holograms in the Mach 3 facility depends upon the Reynolds number and the angle of attack. The optically smart surface holograms survive at  $0^\circ$  angle of attack for Reynolds numbers up to at least  $86.2 \times 10^6/\text{m}$  and additional testing would be required to determine if they survive at higher Reynolds numbers. However, it is the opinion of the authors that the specific type of surfaces tested would survive at any Reynolds number at  $0^\circ$  angle of attack. At  $15^\circ$  angle of attack, these surfaces survived the "clean" flow up to Reynolds numbers of  $86.2 \times 10^6/\text{m}$ . At higher Reynolds numbers, the particle impingement on the surface essentially sand blasted these surfaces, making them unusable for measurements. These particular surfaces at angle of attack will not survive the "dirty" flowfield of a wind tunnel that has not been operated for any significant period of time.

The results of these tests lead to the recommendations that this optically smart surface material would only be usable in high-Reynolds-number flowfields at  $0^\circ$  angle of attack. In the interest of demonstrating the functionality of optically smart surfaces, it is recommended that initial testing at the Wright Laboratory take place in the Trisonic Gasdynamics Facility at a Mach number in the range 0.3 - 0.8. Additional research and development of rugged, optically smart surfaces will continue there.

## **4.5 WL TGF TESTING**

### **4.5.1 TEST DESCRIPTION**

The purpose of this test was to evaluate the performance and determine the usefulness of OSS sensors for the measurements of velocity in the model boundary layer and sublayer and in model positions not accessible by other techniques in wind tunnels. This test was the first time the OSS sensors were used in the range of Mach 0.3 to 0.85 and also represented the first time the sensors had been tested in a full scale wind-tunnel facility. As such, it presented a chance to identify

technical challenges associated with the more rigorous measurement environment. Four types of OSS sensors were tested in the Trisonics Gasdynamics Facility (TGF) at WL: the PM5, the PM5/glass, the RR50 and the FAN fringe sensor. Three were laser velocimetry (LV) sensors and one was a velocity gradient (skin friction) sensor. The PM5/glass was a PM5 sensor that was mounted 7 mm behind a glass window. This design was an attempt to overcome the 3-mm limit of the PM5 and allow it to make measurements all the way down to the wall.

#### Flat Plate Model

A flatplate model was designed for testing at WL that would allow two smart surfaces to be placed at 8 and 14 inches behind the leading edge. The design was provided by WL engineers to MetroLaser. The plate was machined in Irvine and shipped to WL for subsequent fitting of 5 pressure taps located above the test plug openings and spaced evenly along the plate. Six test plugs were built that allowed mounting of different smart surface sensors. Because of the varying thickness of the sensors (shims plus stainless steel), precision steel washers were purchased that allowed the plugs to be shimmed so the holographic surface was flush with the plate.

The flat plate model was installed in the test section with the test side normal to the floor of the facility. The orientation of the model facilitates the optical reference procedure. The model design is shown in Fig. 47.

—



### Seeding

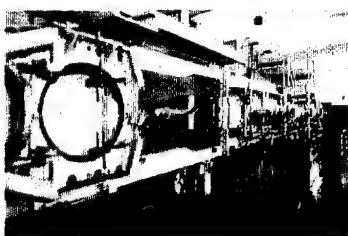
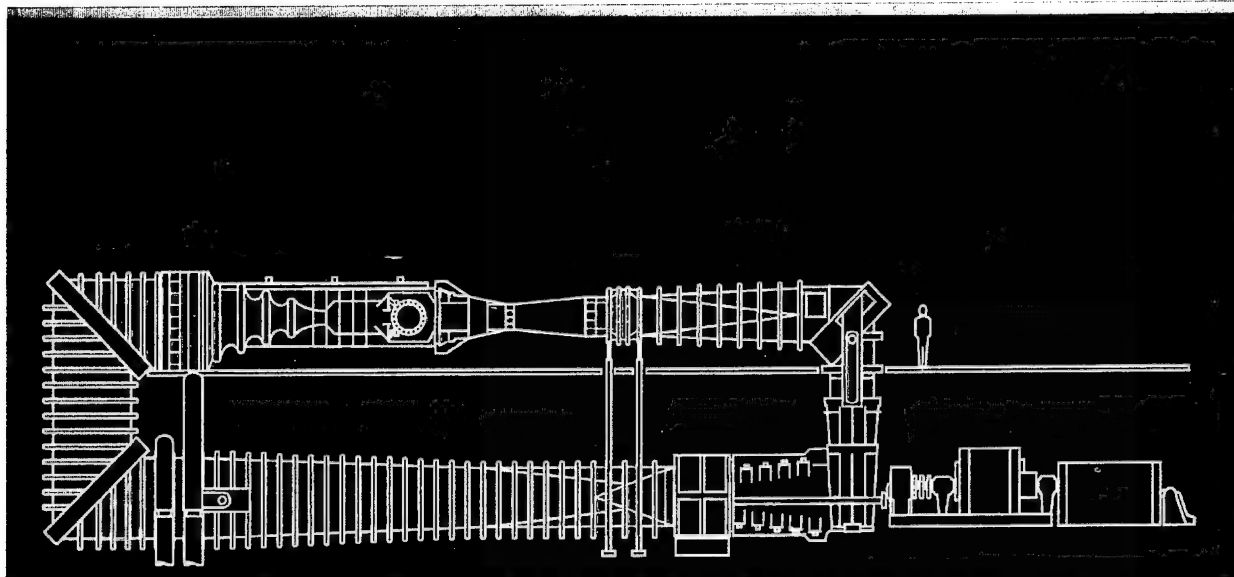
Water was used as the seed for these tests because it was the least likely to damage the holographic surfaces. Typically, silicon oil has been used for seeding in the TGF, but the silicon oil would have distorted the optical surface. The seeder system used was a simple setup with air and water hoses attached to a tee or an atomizing nozzle. The air used was facility shop air at approximately 70 psia. A water pump with a valve in the hose was attached directly to a 5-gallon jug of deionized water. The pump was not designed for continuous use and therefore failed. The water delivery system was changed to a captive tank with regulated air pressure used to deliver the water to the atomizer. The facility dryer was off-line when seeding was used.

## 4.5.2 TGF FACILITY DESCRIPTION

### General Facility Information

The Trisonic Gasdynamics Facility (TGF) is a closed circuit, variable density, continuous flow wind tunnel. (See Fig. 47). It operates at subsonic, transonic, and supersonic speeds through a range of Mach numbers from 0.23 to 3.0.

The 2 foot-square subsonic test section can provide Mach numbers from 0.23 to approximately 0.85. The maximum Reynolds number per foot that can be achieved is 2.5 million. The maximum dynamic pressure for the subsonic section is 350 PSF.



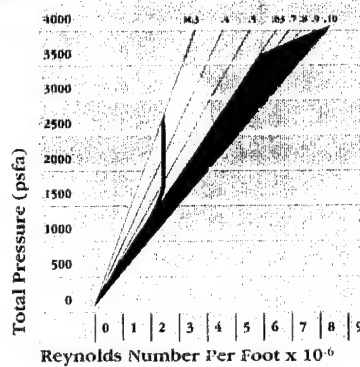
The TGF is converted from subsonic to supersonic testing by interchanging the nozzle blocks exposed in this view with the side walls removed. The  $M = 2.3$  blocks are shown here.



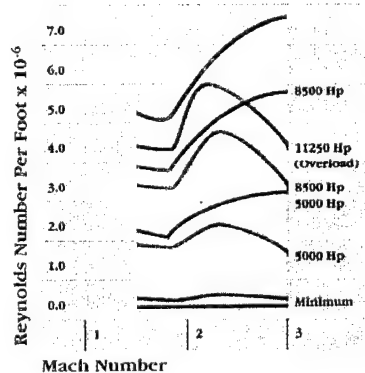
Test conditions are set and maintained from the tunnel control console.



Test data are recorded, reduced to engineering units and plotted for analysis in the TGF control room.



Trisonic Facility subsonic/transonic operating envelope. Compressor drive motors synchronized at Mach .63 and above with transonic insert. Red area indicates transonic insert envelope. Heavy line indicates limit with subsonic blocks and empty test section.



Trisonic Facility supersonic operating envelope. Red lines indicate with second throat, blue lines indicate without second throat.

Fig. 48. TGF Wind Tunnel Diagram.

An insert for transonic testing reduces the test area to 15 x 15 inches. This insert has an option of either two or four variable slotted walls, allowing the wall porosity to be varied between 4 and 12%. The Mach number range for the transonic test section is 0.3 to 1.0. This test section can achieve a Reynolds number of 8 million per foot and a dynamic pressure of 1400 PSF.

The 2-foot, supersonic test section operates at discrete Mach numbers of 1.5, 1.9, 2.3 and 3.0 respectively, through the use of interchangeable fixed nozzle blocks. These blocks have a maximum Reynolds number per foot of 3 to 5 million with a maximum dynamic pressure ranging from 600 to 1,200 PSF.

An auxiliary air system for the tunnel has been installed to accommodate both blowing and suction systems. A 500 PSI high pressure air supply is available at the test section to simulate model jet exhaust or other blowing requirements. This apparatus can provide air at 3 lbm/sec mass flow and a temperature of up to 500°F. Likewise, a vacuum source is available for simulation of model inlet flows or other suction requirements.

The electric drive system for the TGF consists of a 5,000 horsepower synchronous motor and a 3500 horsepower wound rotor induction motor coupled through a double input single output 3.28:1 gear box.

The air flow is propelled by an Allis Chalmers VA 1,310 axial flow compressor with a maximum compression ratio of 4.26:1, at a flow rate of 160,000 CFM. The compressor is 10 stage 50% reaction type with variable stator blades. The compressor is primarily driven at a constant speed of 3600 rpm. The facility operator has instantaneous control by means of individual or simultaneous actuation of all stator blades. This feature renders rapid and sensitive control of flow in the test section.

Temperature equilibrium is maintained in the facility by water cooled, heat exchangers located in the stagnation section. Two sets of heat exchangers are used, one each in the upper and lower legs of the facility. The water is supplied from a 432,000 gallon spray pond located adjacent to the facility complex. Stagnation temperature in the facility is maintained at 100°F by this system with an accuracy of  $\pm 1^\circ\text{F}$ . Stagnation pressure is automatically controlled to within  $\pm 1$  PSF at any selected value from approximately 100 to 4000 PSF, depending upon the Reynolds number desired.

A honeycomb and screen arrangement is located in the 8' x 8-foot stagnation section to minimize turbulence in the test section.

A pair of 28-inch-diameter hinged windows are mounted on the test section sidewalls. These windows can be opened quickly to allow easy access to the models for configuration changes. Also, the two optical quality glass windows allow the use of schlieren, motion picture photography, and laser velocimetry.

The main model support system for the TGF is a rack-mounted, 50-inch radius crescent. The position and angle of the crescent are displayed on the operator's console to an accuracy of  $\pm 1^\circ$ .

0.01 degrees. The center of rotation is the center of the test section viewing window. The pitch range is from -1 to +18.5 degrees for the subsonic and supersonic test sections. The range decreases to -1 to +12 degrees for the transonic section.

A variety of sting extensions are available for attachment to the crescent. The main support has a remotely controlled roll capability of -90 to +180 degrees, with an accuracy of  $\pm 0.005$  degrees. This combined pitch and roll capability provides model angle-of-attack and yaw attitude variation while maintaining flow in the tunnel.

Another support has the capability of traversing horizontally a total of 18 inches to an accuracy of  $\pm 0.001$  inch. This feature is useful for pressure and temperature probing. A computer controlled, three-dimensional traversing capability (axial, vertical, and lateral) has also been provided.

Various types of strut supports are available or can be constructed for special model installations. Two attachment points are available. One is located at the four inch transition section located between the test section and the diffuser. The other utilizes the crescent opening area when the crescent has been removed.

For half span and two-dimensional test model installations, two additional 28-inch window frames are available for installation of blank aluminum plates. These aluminum plates are used with the 2-foot test section. Pressure, temperature, and blowing or suction apparatus can be used with this installation. In the 15x15-inch transonic test section, two-dimensional tests can be conducted in the present slotted test section by replacing the center test slat viewing windows with metal pass-thru inserts. The models are attached outside the test section to the support structure.

An adjustable diffuser is employed in the TGF circuit to increase the efficiency of operations by providing a favorable pressure recovery over a wide range of tunnel conditions. By utilizing the adjustable diffuser as a remotely controlled restriction device, flow through the test section may be completely cut off and directed through a bypass system while keeping the drive train and compressor on line. Thus, stagnation and atmospheric pressure can be equalized, making the test model accessible.

A dryer system is employed in the TGF in order to obtain a dew point necessary to prevent liquefaction in the test section. It is a full flow dryer system utilizing molecular sieve as an agent. It can effectively be used at temperatures up to 200°F. No trouble is encountered in obtaining dew points as low as -35°F with this system. This system continuously recirculates a portion of the air within the facility when operating at all Mach numbers.

### Instrumentation

Facility instrumentation is readily available for any conventional type of testing. Special instrumentation can be acquired for extreme or unusual conditions.

Strain gage balances are primarily used to obtain force and moment data. There exists a sizable inventory of both force and moment balances. The balances are of a six component, internal type which are designed to indicate the aerodynamic loads through deformation of the balance load sensing elements. The load sensing elements have applied to them one or all arms of a wheatstone bridge arranged so as to give an electrical signal proportional to the deformation and ideally the load.

The primary pressure sensing instrumentation consists of electronically scanned differential pressure (ESP) modules of various ranges from 5 lb/in<sup>2</sup> differential to 100 lb/in<sup>2</sup> differential. The pressure modules contain 16, 32, or 64 separate transducers each. Also available are some rack mounted units containing 16 separate transducers each. The transducers can be referenced to a variable pressure from 0 to 14.7 psi or to any other pressure channel being used.

For measurement of velocity and turbulence, a two-channel TSI hot wire anemometer system is available. The system includes a hot wire anemometer voltmeter and linearizer. Some probes are on hand, but in general probes must be specially purchased for a given test.

### Calibrations

The transducers used in the TGF for measuring model pressures are silicon diaphragm transducers made by Pressure Systems Incorporated (PSI). They are differential transducers in the ranges of 5, 15, 30, and 100 psid. They are component parts of the pressure modules in the PSI 780B Electronically Scanned Pressure (ESP) system. Each pressure module contains 16, 32, 48, or 64 channels of transducers which are all manifolded to common reference and calibration manifolds. The Transducers are calibrated in place using the Calibration Standard at vacuum, tunnel static, or atmospheric reference pressure, depending on the test requirements. The ESP modules are calibrated at least every day of tunnel operation, using a 3-point calibration and a second order curve fit. The curve fit accuracy is typically within 0.08% of FULL SCALE.

The calibration standards are resonating quartz crystal transducers made by Paroscientific, Inc. They are Digiquartz series 2000 transducers in the absolute pressure ranges of 15 and 30 psia. The calibration standards are also component parts of the PSI 780B Electronically Scanned Pressure system. The Calibration Standards are calibrated in place every 6 months in the TGF at vacuum reference using the Transfer Standard. The static accuracy is within 0.02% of FULL SCALE.

The transfer standard is a capacitance manometer, made by MKS Instruments. It is a Baratron model 398 system containing three head ranges: 10, 100, and 1000 Torr differential pressure (0.19, 1.9, 19 psid). This system is calibrated in the pressure lab using the pressure lab Primary Standard at atmospheric reference. Due to its unique design, it can then be used to calibrate other instruments at vacuum reference with virtually no shift in calibration. It is recalibrated in the pressure lab every 6 months. The static accuracy of this transfer standard is within 0.05% of READING.



The primary calibration standard, used in the pressure laboratory, is a RUSKA dead weight tester (Model 2460). There are two of these standards in the calibration lab, and they are returned to the manufacturer every 5 years for NIST recertification. The rated accuracy of these units is 0.015% of READING.

Total uncertainty of any pressure measurement will be a combination of the accuracies in the various calibration devices. Note that the uncertainties in the primary and the transfer standard are stated in percent of READING while those of the calibration standard and of the transducers themselves are stated in percent of FULL SCALE. A conservative approach is used to quote the total uncertainty of the devices used in calibration by treating the errors as a percent of transducer FULL SCALE. If all errors are considered independent, then a 95% confidence interval may be obtained using the Root Sum Square method (RSS):

$$\text{ERROR} = (.015\%^2 + .05\%^2 + .02\%^2 + .08\%^2)^{.5}$$
$$\text{ERROR} = \pm 0.1 \% \text{ of Transducer FULL SCALE}$$

The strain gage force and moment balances used in the tunnel are sourced from several manufacturers and calibrated prior to each test entry in the Experimental Branch (FIMN) Force Laboratory. Pretest and post test check loadings are performed in the tunnel to verify that all outputs are maintained to within the balance calibration accuracies.

The laboratory calibrations include bidirectional, equal increment loadings of all the primary components and selected combination loadings as necessary to simulate the actual predicted tunnel test article loads. Generally, at least five load increments are used for each loading. These loadings are provided by standardized calibrated disc weights. Angular sting deflection measurements are also taken during these calibrations and verified during check loadings on the installed test article.

Balance data are reduced using multiple linear regression analyses to determine a matrix of constants and interaction terms, normally of first order significance. Normally targeted accuracy of balance calibrations is  $\pm 0.05\%$  of full range load capacity. These accuracies, however, may vary slightly with application or special use. Most balance calibrations and histories have been maintained on file in the WL Experimental Branch, FIMN.

### Data System

Data are collected and recorded by a Micro VAX III, programmable computer through a software controlled, 120-channel, 40-mV to 10-V, differential multiplexer and a 13-bit 100,000 samples per second, auto ranging analog-to-digital converter. All necessary electronic equipment (power supplies, signal conditioners, amplifiers, etc.) is available to electrically condition the previously mentioned instrumentation such that their respective electrical signals can be processed by the 120 channel multiplexer. After the data have been read by the computer, further data processing continues on line under program control. The primary language utilized by the system is FTN77. Processed data are typically provided on a 9 track digital magnetic tape, ethernet, and/or an LN03

laser printer/plotter, and can be examined during the progress of the test as each test point is recorded.

#### 4.5.3 TEST PERIOD

The transmitter, receiver and computer equipment was shipped to WL on March 14, 1994. Setup of the optics began on the 22nd of March at the Trisonic Gasdynamics Facility and testing of the Smart Surfaces began on the 23rd. The PM5 was the first sensor to be tested in the tunnel. The tunnel occupancy was from 15 March to 6 May 1994. During this period, there were three discrete periods of tunnel operation. From 15 March to 1 April 1994, MetroLaser personnel and the associated government personnel worked together on the first phase of the test. From 25 April to 29 April 1994, government personnel operated without the assistance of MetroLaser personnel. The final set of data was acquired from 2 May to 6 May 1994 with MetroLaser personnel and government personnel again working together.

#### 4.5.4 SPECIAL TEST PROCEDURES

At the lower Mach numbers (0.4 and below) the compressor veins were completely unloaded and a couple of them would oscillate and cause oscillations or surging in the tunnel that could be heard. The tunnel operator was able to reduce the oscillations by opening the bypass and loading the vanes, thus moving them off the limit.

#### 4.5.5 TEST NOTES

The information given here is intended to be of help should the test be run again. Lenses L1 and L3 on the transmitter (refer to Fig. 7) should be put on micrometer driven traverses so that alignment would be faster and more precise.

Requirements for all facility equipment needed for the test should be carefully defined and preliminary sketches of the optical setup approved by both contractors and WL personnel. Items such as mechanical access and platform stability should be examined. Care should be taken to identify whether steel optical tables are required for use with magnetic bases.

Aluminum tooling plate should not be used for wind tunnel models because it is difficult to machine, damages easily and has reduced loading capacity compared with standard 6061 stock.

A pretest briefing should be given to advise personnel involved in the test that because the OSS system is in an early prototype phase, progress may be slow and erratic. Many hours may pass without collection of data while adjustments are made to the optics and electronics. Conversely, when the system does become operational, data collection may proceed at a rapid pace and require the immediate attention and cooperation of the tunnel personnel.

#### 4.5.6 TEST SUMMARY

Both the transmitting optics and the receiving optics were mounted on a large optical table which was attached to a three axis, linear translation stage positioned on the north side of the test section. Optical access was through the north test section window. (See Fig. 49 for a photograph of the installation.) Data taken from the tests were recorded on computer. Additionally, each mean velocity, RMS, tunnel MACH number and calculated velocity were recorded in a test log.

##### PM5 Sensor

Laser velocimetry data were collected in the TGF using the subsonic blocks for freestream Mach numbers in the range 0.3 to 0.85. The stagnation pressure was approximately 57.5 kPa and the stagnation temperature was 311 K for a unit freestream Reynolds number in the range of  $3.4 \times 10^6/\text{m}$  to  $7.5 \times 10^6/\text{m}$ . This OSS sensor uses two address beams, one of which has to be frequency shifted using an acousto-optic modulator (Bragg shifter) in order to cover the range of velocities (frequencies) required. At each location, 100 samples were collected and the mean value of these samples is shown with freestream velocity plotted against Mach number in Fig. 50. Also shown in Fig. 50 is a line representing the theoretical velocities calculated using isentropic equations for a compressible flow. Multiple data points at each Mach number represents multiple data sample sets. The data follows the theory reasonably well in this Mach number range. It is believed that data could be taken up to Mach 3.0 with a faster data acquisition board.

A boundary-layer survey was conducted at Mach 0.4 with data being collected between 2 mm and 70 mm off the hologram. The data from this profile are also shown in Fig. 51, with distance plotted against velocity ratio where the velocity is normalized against the velocity measured by tunnel instrumentation. Some of the data points were taken with a standard PM5 sensor and some were taken with a PM5 set 4.76 mm below the model surface with a glass plate filling the gap (PM5G). The PM5G was designed in an attempt to measure velocities closer to the model surface than possible with the standard PM5; however, seeding and frequency response appear to have limited the effectiveness of the PM5G. The data from several days and sensors cluster fairly well, but not perfectly. This indicates that a more precise alignment procedure must be used in setting up the optical system. Also, note that as distance from the plate increases beyond a typical turbulent boundary-layer profile, the velocity decreases instead of remaining at the freestream velocity. This is attributed to a possible minor angle-of-attack of the model, creating a divergent channel with the tunnel side wall.

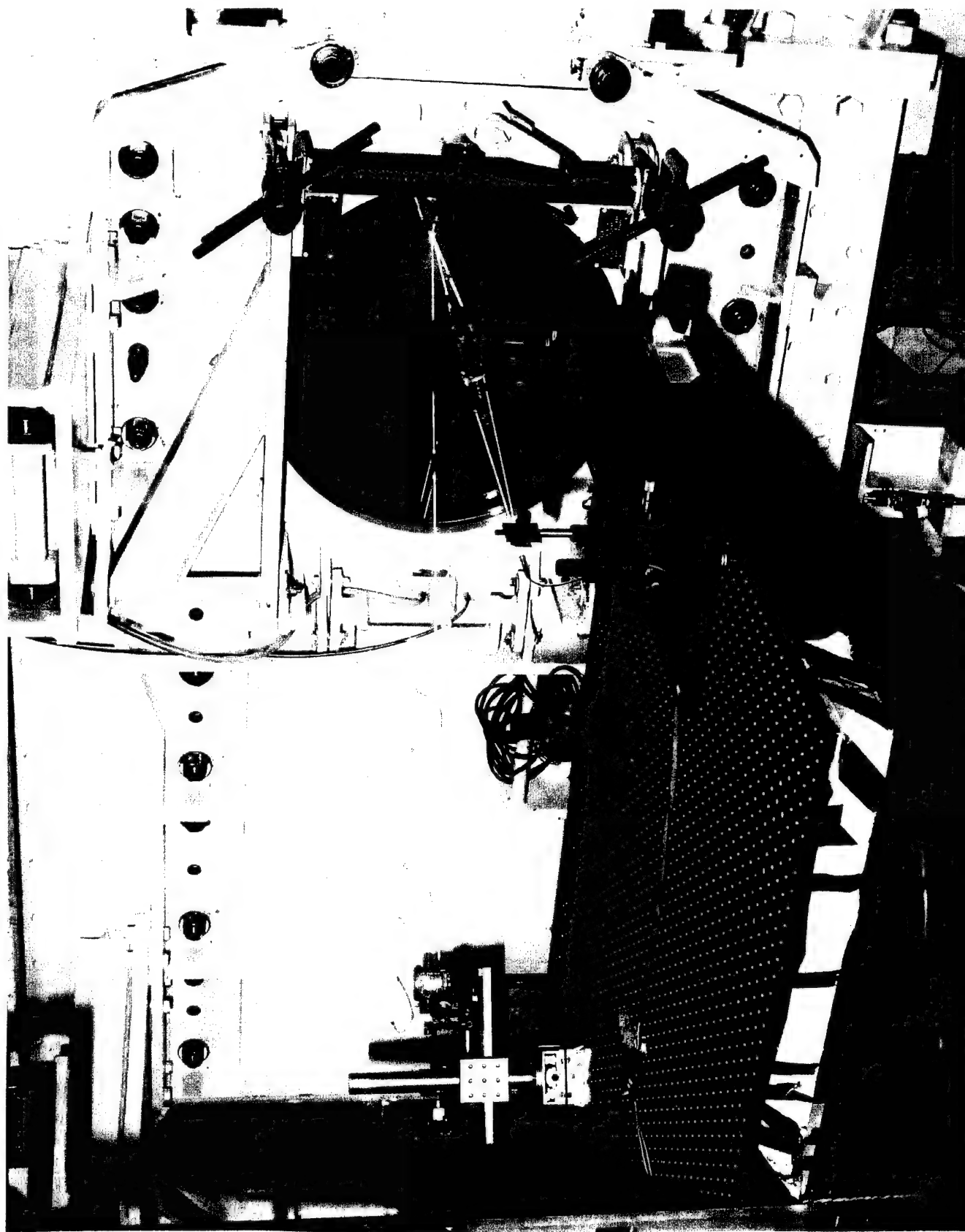


Fig. 49. TGF Optically Smart Surface Transmitter, receiver and model - Installation Photo

Optically Smart Surface – TGF Test  
Mach number survey – 28 Mar/01 Apr 94

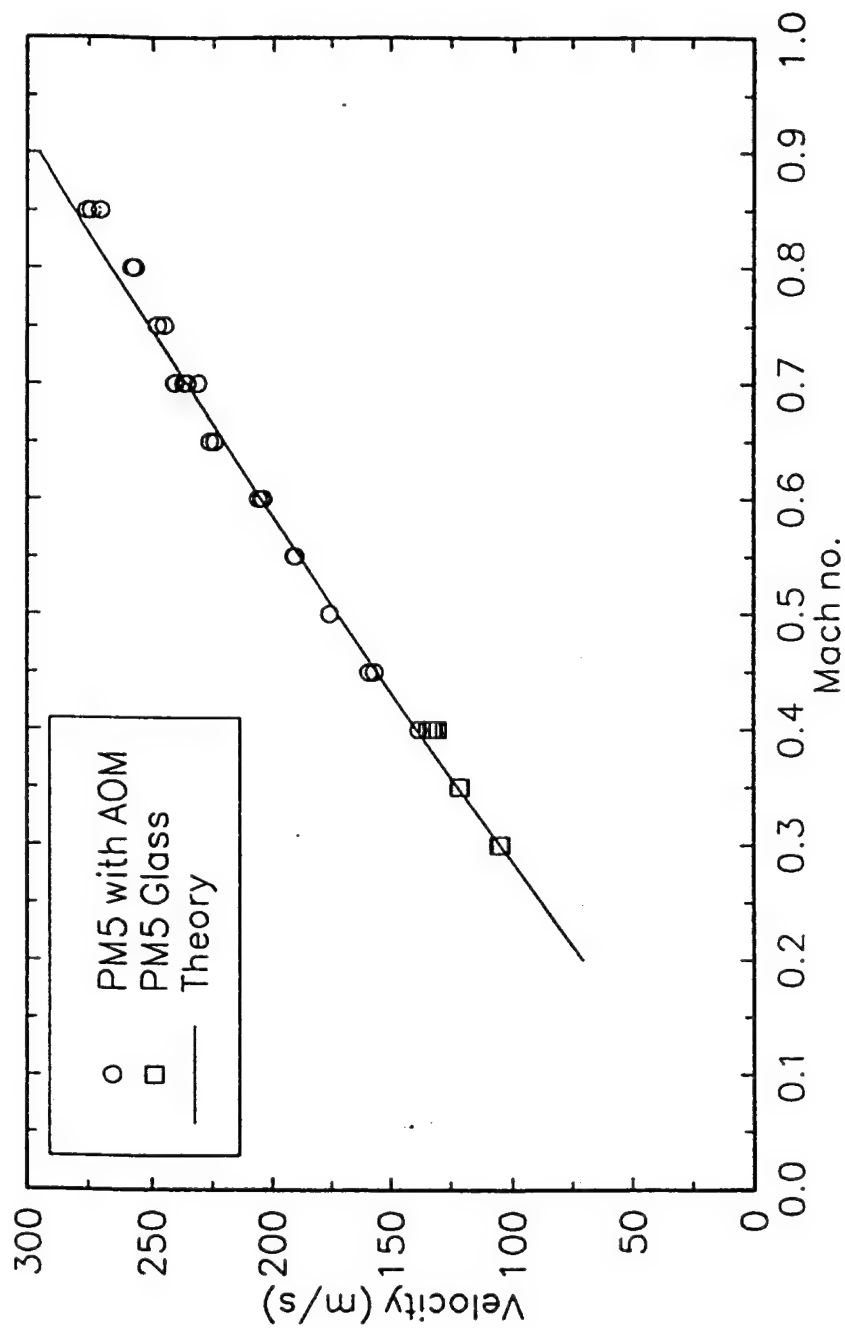


Fig. 50. PM5 Freestream Velocity Measurements,  $M = 0.3 - 0.85$

Optically Smart Surfaces – TCF Test  
 PM5/PM5G, Mach 0.4, 25/31 Mar/01 Apr 94

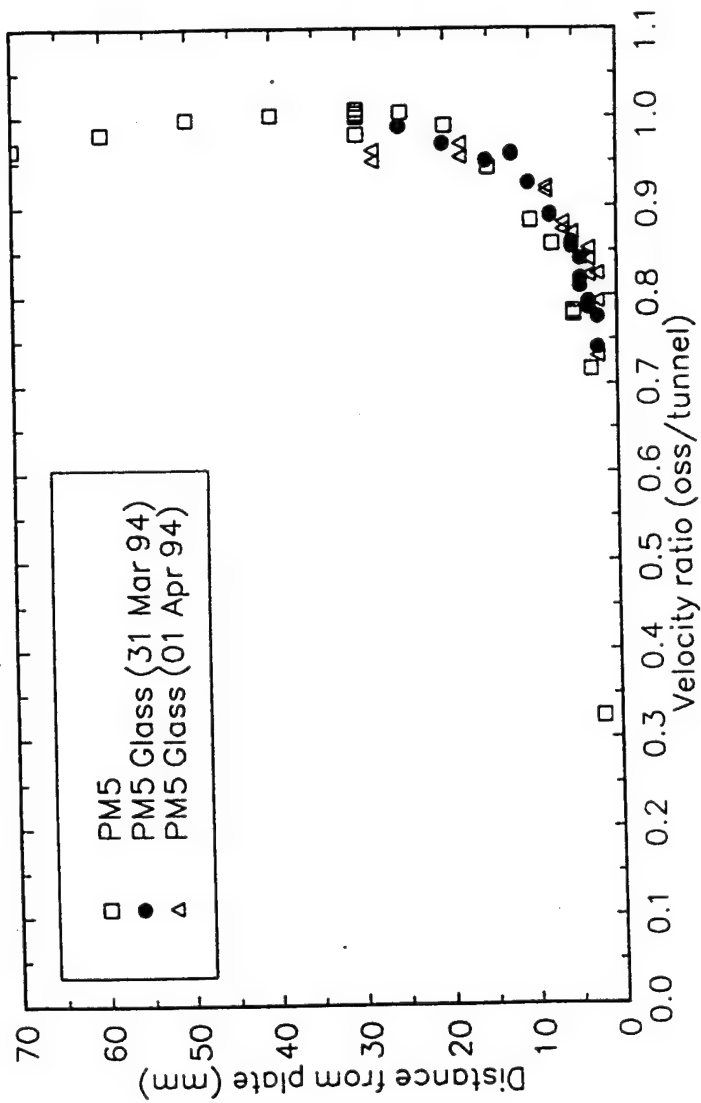


Fig. 51. PM5 Boundary Layer Profile Measurement at M - 0.4

### RR50 Sensor

The RR50 sensor was successfully used in the calibration channel at MetroLaser to measure the boundary-layer laminar sublayer. There was only time available to try this OSS sensor during one shift in the TGF. The results were questionable and the exact reasons were not determined but it could have been a seeding problem, dirty tunnel window, or optical alignment.

### FAN Sensor

The FAN sensor was tested in the last three shifts of the test. Data taken with the FAN sensor are plotted in Fig. 52 as a function of Mach number. Problems were encountered when trying to repeat the acquired data. There was a large perturbation in the data when tunnel conditions were changed. It was found that with time, while keeping the tunnel conditions constant, the data would return to more expected values. It is now understood that receiver alignment is critical to the operation of this sensor. The minimum usable height of the sensor was later determined to be 120 microns. Future tests of this sensor will require additional, perhaps automated, alignment procedures. Future generation FAN sensors should have increased measurement capability making measurement at higher shear stress values possible.

### Thermal Sensitivity

The thermal sensitivity of the sensors was also tested by reducing the tunnel stagnation temperature from 311 K to 300 K. Freestream velocity measurements were then taken between Mach 0.3 and 0.47. The data were unaffected by the tunnel and model temperature. Thus, we conclude that the sensors are not thermally sensitive to moderate deviations.

# Optically Smart Surface – Fan Fringe 5, 6 May 94

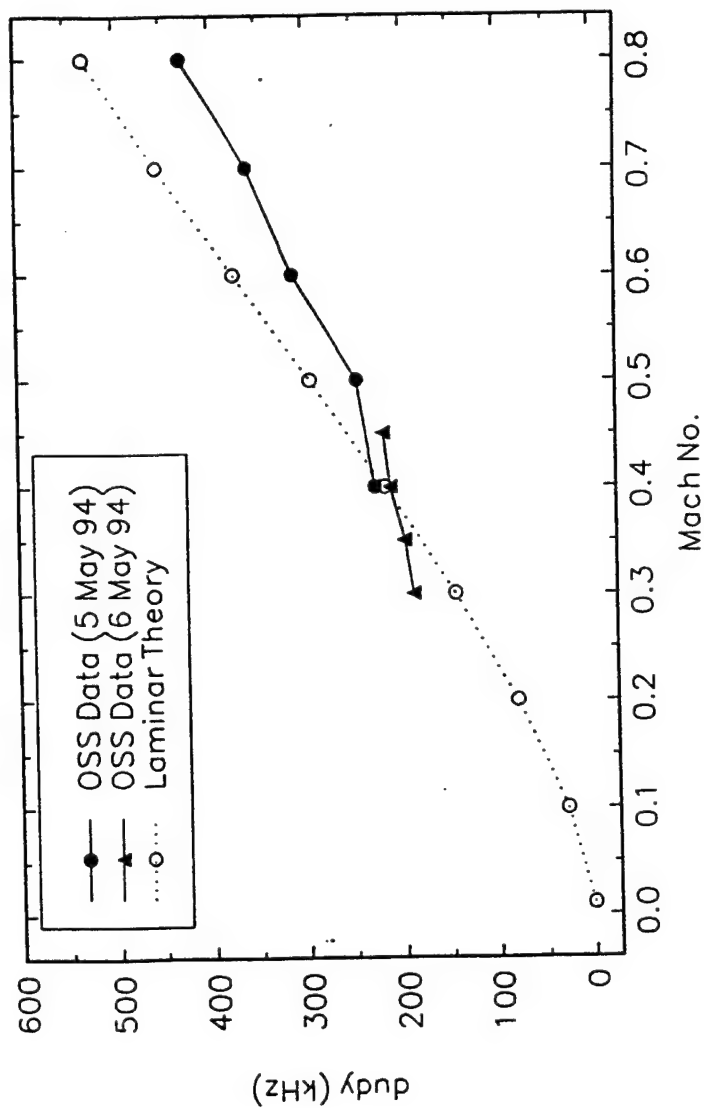


Fig. 52. Fan Fringe Sensor Velocity Gradient Measurement ( $du/dy$ ) for M - 03 - 0.8



## 5.0 RECOMMENDATIONS FOR FUTURE DEVELOPMENT

### 5.1 MULTIPLEXED VOLUME RECORDINGS

An additional idea which grew out of this program is the possibility of recording volume type reflection holograms in a material such as Dupont's green sensitive photopolymer. The idea behind a volume hologram is that recording and playback takes place inside the volume of a material with a thickness on the order of 20 -100 microns, as opposed to being just a surface interaction. The advantages to this method are that diffraction efficiency may approach 100%, multiple holograms can be stored inside the same media, each holographic image can be recalled independently and the recording and playback wavelength can be the same so the chromatic aberrations are eliminated. Fig. 53 illustrates the idea behind the multiple hologram storage that is possible using volume holography. Multiple holograms can be recorded using either different reference beam angles or different laser wavelengths for each recording. The images can be recalled either individually or in parallel. Using the frequency multiplexed scheme, where each hologram is recorded with a different wavelength, every sensor can be replayed simultaneously, allowing data to be gathered in parallel. This could be useful to recall multiple probe volumes of different height as shown in Fig. 53. Detection of each probe volume could be accomplished by a combination of spectral filtering and/or image plane filtering. In addition, different types of holograms can be recorded in the same media. For instance, The FAN fringe sensor could be combined with several standard LV probe volumes so that one sensor could detect the velocity gradient inside the sublayer as well as several fixed points outside the sublayer. In this way, a complete velocity profile could be obtained using only a single sensor.

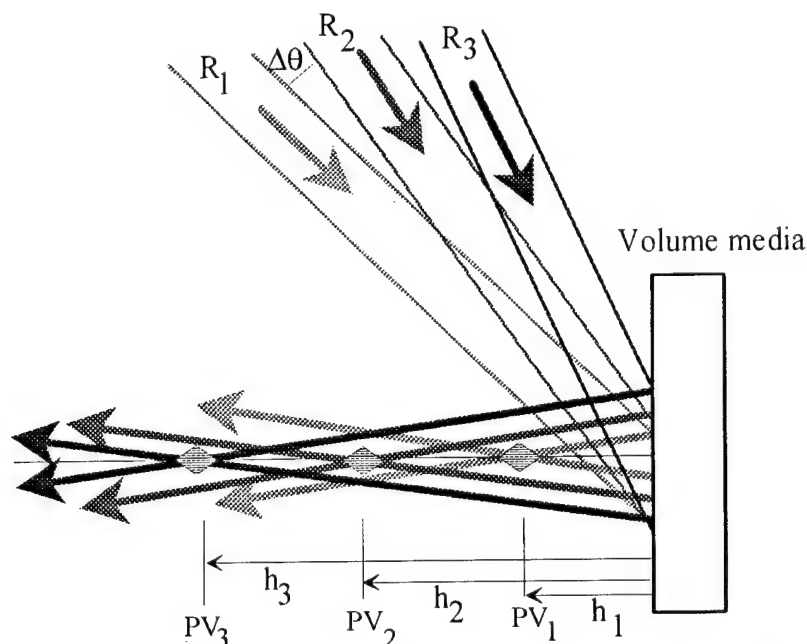
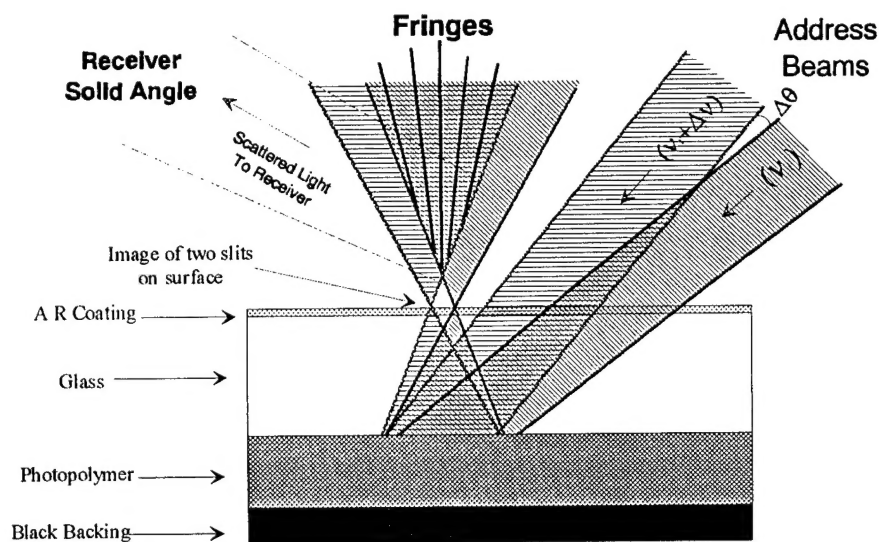


Fig. 53. Multiple probe volume reconstruction using volume holographic media. Angular change between reconstruction beams is not necessary if different colors are used.

## 5.2 FAN FRINGE VOLUME RECORDINGS.

An improved method for recording and reconstructing a FAN fringe sensor capable of measuring flow direction was identified. This new sensor is similar in concept to the FAN fringe sensor tested in the calibration channel; however, it is significantly improved due to its ability to detect flow reversals and its high efficiency. The idea is also based on recording volume type reflection holograms in a material such as Dupont's green sensitive photopolymer. Creating the holographic fan fringe sensor can be accomplished by recording the image of two slits directly on the surface of a transparent substrate. Fig. 54 illustrates the concept of the holographic sensor. The sensor can be recorded in several ways. The simplest realization is the stationary fringe sensor which requires only one address beam to record and playback. This sensor could be very useful for a wide variety of measurements but is incapable of determining flow direction.



**Fig. 54. Holographic implementation of Fan fringe sensor. Drawing illustrates multiplexed recording to produce rotating fan. Stationary fan can be made with a single reference/reconstruction beam.**

For situations where flow reversals may be encountered, a two frequency, multiplexed recording can be used. This is shown in Fig. 54 where the two beams are separated by a small frequency difference (20 - 80 MHz) and are incident at slightly different angles (10 degrees). Each beam reconstructs one of the slits and, as a result, the fan fringes rotate. This allows instantaneous detection of flow reversals.

## 5.3 CURVED SURFACE VOLUME RECORDINGS

The sensors can be economically produced on small glass plugs (2 - 5 mm dia. x 5mm). For applications where the model curvature is small or flat, the plugs may be mounted directly into the surface by taping holes of the required depth. With proper tolerances during manufacturing, reasonable flushness should be possible. This permits mass production for placement at multiple locations on a model. Fig. 55 illustrates the concept of multiple sensors. Each sensor can be

addressed with the same laser transmitter and optical receiver or multiple, simultaneous measurements could be made.

In applications where flushness is critical, such as turbulent transition regions, or when mounting on a curved surface, such as the leading edge of a wing, the sensors can be mounted from underneath a transparent surface. In this case, it is necessary to record the sensors with them installed in the model to compensate for exact depth and curvature of the surface. Photopolymer, because of its unique ability to develop without any chemical processing, would permit embedded sensors to be recorded directly on a model.

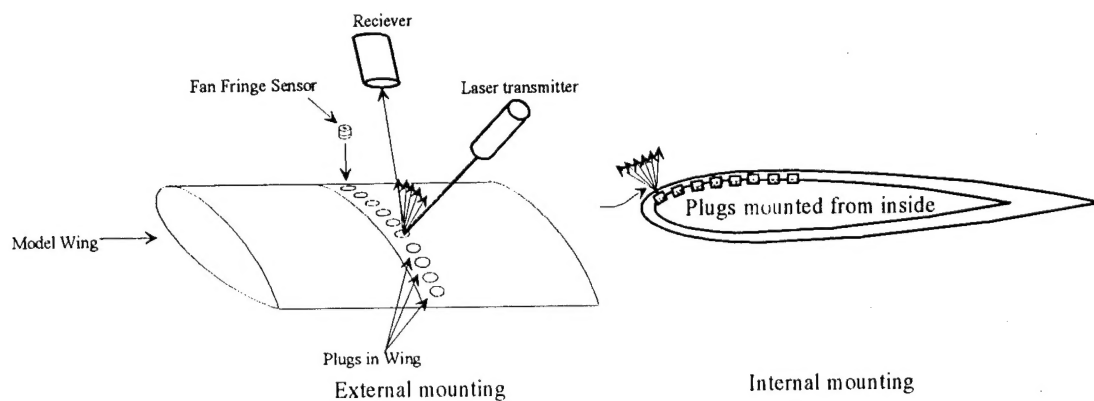


**Fig. 55. Incorporation of sensors into aerodynamic models. Plug size would be on the order of 5 mm diameter and 3 mm in depth. In flow situations where flushness of the sensor may cause tripping of the boundary layer, the sensor can be integral part of model as shown for internal mounting.**

## 6.0 CONCLUSIONS

A unique, new, nonintrusive optical diagnostic technique called "optically smart surfaces" (OSS) has been demonstrated and validated in the subsonic regime. This diagnostic system has been demonstrated in both a low-speed calibration channel and a full-scale, trisonic wind tunnel at subsonic speeds. Optically smart surfaces can be used to overcome some of the geometric limitations of conventional laser velocimetry systems. OSS technology is well suited for applications requiring long range remote measurements. The surface referenced nature of the measurement mitigates the effects of vibration and thermal expansion on probe location. One component, LV measurements, have been made at a range of 0.05 mm to 300 mm from the model surface and at flow rates of up to 270 m/s. The velocity range can be extended into the supersonic regime by incorporating higher speed signal processing equipment. Measurement of velocity gradients inside the laminar sublayer of turbulent boundary layer flows, which provide a measure of shear stress and skin friction, has been demonstrated using the FAN sensor. The FAN sensor tested here had a dynamic range of  $2 \text{ N/m}^2$ . This could be increased by an order of magnitude through improved recording techniques. Other adaptations of the existing OSS designs can result in sensors to measure mechanical stress, temperature, and boundary-layer transitions. We have also shown, both analytically and experimentally, that it is possible to record OSS on curved surfaces in such a way that surface curvature is compensated for in the holographic reconstruction. We have proposed that volume holographic recording media could replace the surface relief holograms so that multiple sensors could be recorded in the same physical location. Each sensor could be recalled using a separate reference beam that differed in angle and/or wavelength. Thus, each sensor could make multiple measurements in serial or in *parallel*.

Further refinement and development of OSS technology could produce a commercially viable product. In addition to applications in aerodynamic measurements, OSS could have significant commercial potential in the areas of gas, oil, and water volumetric flow measurements, remote displacement measurements and security verification.

## 7.0 REFERENCES

- <sup>1</sup> L.G. Smith, G. W. Williams, J. Swienton and J. Millerd, "Optically Smart Surfaces Laser Velocimetry Measurements," AIAA 95-0641 33rd Aerospace Sciences Meeting and Exhibit, Reno, Nevada, Jan. 9-12, 1995.
- <sup>2</sup> J.D. Trolinger and D.M. Rosenthal, 1992b "*Optically Smart Surfaces for Aerodynamic Measurements*," AIAA Paper 92-3895, July 1992.
- <sup>3</sup> Optical Methods in Engineering Metrology, Chap. 6, D.C. Williams, Editor, Chapman and Hall, New York, 1993.
- <sup>4</sup> A.A. Naqwi and W. C. Reynolds, "Measurement of turbulent wall velocity gradients using cylindrical waves of laser light," *Exp. Fluids* Vol. 14, pp. 121-132, 1991.
- <sup>5</sup> M.Born and E. Wolf, Principles of Optics, Chapter 8, Pergamon Press New York, 1970.
- <sup>6</sup> N.K. Sheridan, "Production of Blazed Holograms," *Appl. Phys. Lett.* **12**, 316 1968.
- <sup>7</sup> M.P. Petrov, S.I. Stepanov and A.V. Khomenko, "Photorefractive Crystals in Coherent Optical Systems," Springer-Verlag, New York, (1991).
- <sup>8</sup> White Fluid Mechanics McGraw-Hill 1979
- <sup>9</sup> H. Schlichting Boundary Layer Theory, McGraw-Hill, New York, Chapt. X, 1968.
- <sup>10</sup> K.G. Winter, *Progress in Aerospace Sciences*, Vol. 18, 1977.
- <sup>11</sup> P.H. Alfredsson, A.V. Johansson, J.H. Haritonidis and H. Eckelman "*On the Fluctuating Wall Shear Stress and the Velocity Field in the Viscous Sublayer*," *Phys. Fluids* 31, 1025 (1988).
- <sup>12</sup> L. Smith and G. Williams, "Optically Smart Surfaces Survivability Testing at Mach 3," Wright Laboratory, WL-TM-93-300, 1993
- <sup>13</sup> A.W. Fiore, D.G. Moore, D.H. Murray and J.E. West, "*Design and Calibration of the ARL Mach 3 High Reynolds Number Facility*," Aerospace Research Laboratory, ARL TR 75-0012, January 1975.